6-27-2018 1:00 PM

Non-Cancerous Abnormalities That Could Mimic Prostate Cancer Like Signal in Multi-Parametric MRI Images

Mena Gaed
The University of Western Ontario

Supervisor
Dr. Fenster, Aaron
The University of Western Ontario
Dr. Moussa, Madeleine
The University of Western Ontario

Graduate Program in Pathology
A thesis submitted in partial fulfillment of the requirements for the degree in Master of Science

Abstract

Prostate Cancer (PCa) is the most common non-cutaneous cancer in North American men. Multi-parametric magnatic resonance imaging (mpMRI) has the potential to be used as a non-invasive procedure to predict locations and prognosis of PCa. This study aims to examine non-cancerous pathology lesions and normal histology that could mimic cancer in mpMRI signals. This study includes 19 radical prostatectomy specimens from the London Health Science Centre (LHSC) that were marked with 10 strand-shaped fiducials per specimen which were used as landmarks in histology processing and ex vivo MRI. Initial registration between fiducials on histology and MR images was performed followed by the development of an interactive digital technique for deformable registration of in vivo to ex vivo MRI with digital histopathology images. The relationship between MRI signals and non-cancerous abnormalities that could mimic PCa has not been tested previously in correlation with digital histopathology imaging. The unregistered mp-MRI images are contoured by 4 individual radiology observers according to the Prostate Imaging Reporting and Data System (PI-RADS). Analysis of the radiology data showed prostatic intraepithelial neoplasia (PIN), atrophy and benign prostatic hyperplasia (BPH) as main non-cancerous abnormalities responsible for cancer like signals on mpMRI. This study will help increase the accuracy of detecting PCa and play a role in the diagnosis and classification of confounders that mimic cancer in MR images.

Keywords

Prostate imaging, Prostate non-cancerous abnormalities, Prostate image regestirations, in-vivo prostate MRI, Prostate cancer.

Acknowledgments

Today is the day: writing a small note of appreciation is the finishing touch on my dissertation. It has been a period of intense learning, not just in the scientific arena, but on a personal level.

My appreciation and gratitude to my committee are infinite. Your support and willingness to help will not be forgotten. Special thanks to Dr. Fenster, my supervisor, for his valuable advice, great support, and opportunities to conduct this research. I would also like to thank Dr. Moussa (co-supervisor) for the valuable assistance I have received from her and providing me with the tools to successfully complete my dissertation.

To my small family, I dedicate this work to you all; Giustina, Demetrius, and my lovely wife, Mary. Giustina and Demetrius were born during the development of this work. Here are to many late nights of multi-tasking writing and bottle feeding. Thank you for making me laugh when I needed it the most. Thank you to my wife for her love and support, I could not imagine completing this work without you next to me.

Finally, I would like to acknowledge with gratitude, my bigger family. I am indebted to my parents who introduced me to the realm of academic excellence. I am grateful for your support in my dreams, encouraging my pursuits and guiding me in the right direction. I cannot forget my amazing siblings for all their love and support. All these years, you guys never cease to amaze me with your surprises.

To my brother Michael, I thank you for the long hours of discussions that helped me to focus and complete this research. Even though we do not see each other as often, your support from halfway around the world is always felt.

For all these reasons, I dedicate my success and this research to my family!

Table of Contents

List of Tables

Page

List of Figures

Page

List of Abbreviations

2D	Two-dimensional
3D	Three-dimensional
ADC	Apparent Diffusion Coefficient
AFMS	Anterior Fibromuscular Stroma
BPH	Benign Prostatic Hyperplasia
CZ	Central Zone
DCE	Dynamic Contrast-Enhanced
DRE	Digital Rectal Examination
DWI	Diffusion Weighted Imaging
ED	Ejaculatory Ducts
EPE	Extra-Prostatic Extension
ERC	Endo-Rectal Coil
H&E	Hematoxylin and Eosin
HDI	Histopathology Digital Images
HGPIN	High-Grade Prostatic Intraepithelial Neoplasia
K^{trans}	Pharmacokinetic Contrast Transfer Coefficient
K_{ep}	Pharmacokinetic rate Constant
LHSC	London health science centre
Lt	Left side
mpMR	Multi-Parametric Magnetic Resonance
mpMRI	Multi-Parametric Magnetic Resonance Imaging

MR	Magnetic Resonance
MRI	Magnetic Resonance Imaging
MRS	Magnetic Resonance Spectroscopy
PAH	Post-Atrophic Hyperplasia
PCa	Prostate cancer
PCSM	Prostate Cancer-Specific Mortality
PIN	Prostatic Intraepithelial Neoplasia
PI-RADS	Prostate Imaging Reporting and Data System
PSA	Prostate Specific Antigen
PZ	Peripheral Zone
Rt	Right side
SA	Simple atrophy
SI	Signal Intensity
SNR	Signal to noise ratio
SV	Seminal Vesicles
T2W	T2 Weighted
TRE	Target Registration Error
TRUS	Trans-Rectal Ultrasound
TZ	Transition Zone
$\boldsymbol{V_e}$	Pharmacokinetics contrast leakage

Chapter 1

1 Introduction

1.1 Prostate Cancer Epidemiology

Prostate cancer (PCa) is one of the most common cancers in North American men and the developed world. It is the second leading cause of cancer in men after skin cancer. According to the World Health Organization (WHO) (Globocan 2012), approximately that 1.1 million men worldwide were diagnosed with PCa with an estimated seventy-percent of cases established in developed countries (**Figure 1.1**). These countries include USA, Canada, Australia, and New Zealand as well as Northern and Western European regions, which demonstrates the wide-ranging geographic variation of incidence with a twenty-five fold increase in incidence compared to developing countries [1].

Several influences are responsible for incidence variations, including methods of data gathering and analysis, socio-economic status (SES) as well as access to the healthcare system. To further demonstrate this variation, the introduction of PCa screening tests with Prostate Specific Antigen (PSA) in the late 1980s and early 1990s has significantly increased asymptomatic PCa cases detected in North America and the United Kingdom [2].

In 2012, it was estimated that 307,000 deaths were due to PCa, with a tenfold increase in the new incidence rate compare to the mortality rate [1]. Despite the increase in incidence rates of PCa in almost all countries, the mortality rate is higher in developing countries compared to a significant decline in developed countries [3] (**Figure 1.2**). The developed healthcare system is associated with a high level of PCa diagnosis accompanied by low mortality rate. The Canadian Cancer Society and The National Cancer Institute Surveillance, Epidemiology and End Results (SEER) in the USA estimated that new cases of diagnosed PCa for 2015 were 24,000 in Canada and 220,800 in the USA. The mortality numbers were 4,100 in Canada and 27,540 in the USA. In Canada, PCa represents 24% of all cancer cases affecting men, compared to 13.3% in the USA.

Similarly, Canadian records reveal that PCa is responsible for 10% of all estimated cancer deaths compared to 4.7% in the USA with a five-year survival rate of 96% and 98.9% in Canada and the USA respectively [4, 5].

With many risk factors associated with PCa, five leading causes have been discovered to have the strongest significance on PCa. These include race/ethnicity, age, family history, diet, and genetics, which will be discussed below [6].

1.1.1 Race/Ethnicity

Several studies have concluded that black men or those with African descent have a higher risk of PCa compared to Caucasian men as well as a higher mortality rate with a 2.5-fold increase between the two racial groups [5]. Also, studies have shown that black men have a greater risk of being diagnosed with an advanced PCa grade at a younger age compared to Caucasian men in the same age groups. The lowest incidence of PCa was reported in Asian races and communities [1, 7-9]. Data from the Detroit (SEER) registry confirms with the radical prostatectomy specimen analysis, that the cancer volume and Gleason score were higher in Black men. They have an increased risk for more advanced and distant metastasis with a ratio of 4:1 compared to Caucasian men. These findings support the faster growth and transformation to clinically significant disease in Black men in comparison to Caucasian men [10].

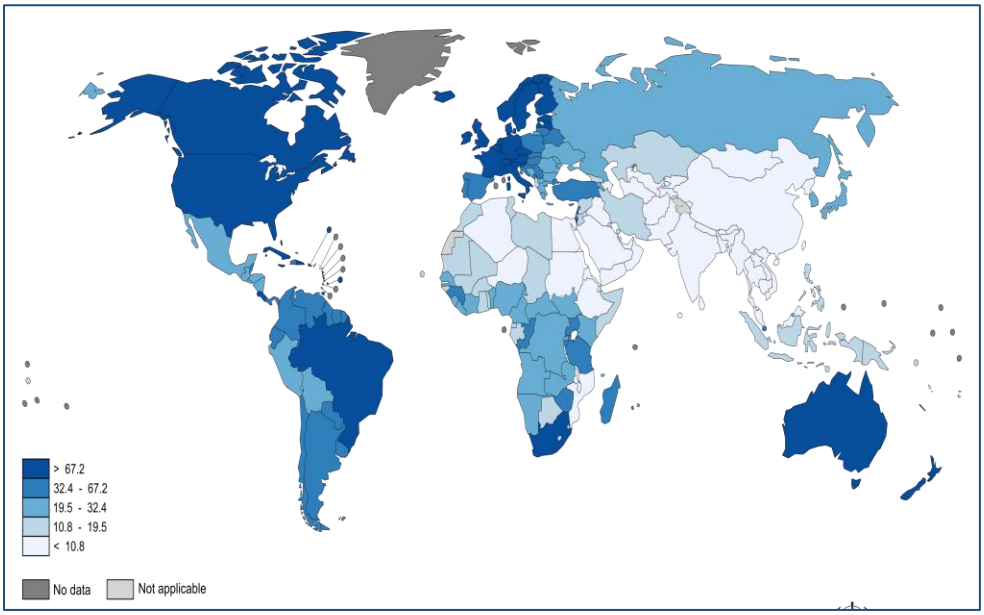

(**Figure 1.1**) **World map presenting the distribution of PCa incidence worldwide per 100,000** (Globocan 2012) [1]

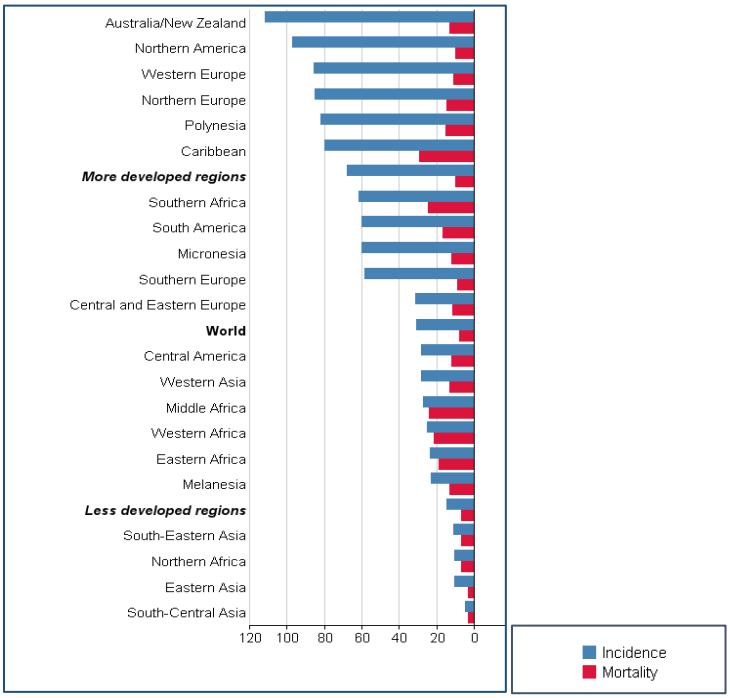

(**Figure 1.2**) **International incidence and mortality of PCa worldwide per 100,000**. (Adopted from Globocan 2012) [1]. The graph presents a high incidence of PCa associated with low mortality in developed countries while developing countries sustained similar mortality rates despite low incidence rates.

1.1.2 Age

Before the introduction of PSA screening, PCa was called the disease of old age. The risk of diagnosis of PCa in men under the age of forty is very low. It is estimated that 1 in 55 men will be diagnosed with PCa in the age group of 40-60 years. However, this ratio will increase to 1 in 7 men in the age group of 60-80 years [11]. Autopsy results in prostate tissue sampling illustrate that 75% of men over 80 years old will develop latent microscopic PCa at some point in their lives [12, 13]. Other studies have indicated that 26% of men over the age of 75 will be diagnosed with high-risk disease and clinically significant cancer. Clinically significant cancer is defined as cancer with a volume of more than 0.5 cm^3 and/or a Gleason score of more than 6 [14]. Advanced age at the diagnosis of PCa is one of the major risk factors for increased Prostate Cancer-Specific Mortality (PCSM) [15].

1.1.3 Family and Socioeconomic Status

The family history of PCa is another well-known risk factor that presents a sufficient warrant for early screening and close monitoring to detect early PCa when it arises. Studies demonstrated that the risk of PCa is higher with brothers involvement than father involvement [16]. The family history of PCa is a greater risk factor for a more fatal and aggressive disease than for the isolated incidence of PCa, which points to the association of fatal PCa to a genetic subgroup [17].

However, PCa risk factors are more complicated than initially thought. It has been reported that higher Socioeconomic Status (SES) groups demonstrate high incidents of PCa with a low mortality rate across all racial and ethnic groups [18]. Research studies report the early detection of PCa is possible due to the increase of frequent screening and an advanced health care system. Studies have also indicated that regular screening is responsible for a small percentage of discovery. Additional factors should be considered and examined carefully for further understanding of the Socioeconomic Status and its relation to a higher PCa incidence [19].

1.1.4 Diet

The fourth factor is the type of diet patients follow and its relationship to PCa incidence. Diets that contain a high fiber content such as vegetables and low fat have been associated with a decreased incidence of PCa. However, diets that involve high caloric content fatty foods such as red meat, dairy products and calcium from dairy products were also associated with increased incidence of PCa [20]. Some authors report that the consumption of fish three times or more per week was associated with a decreased risk of PCa as well as lowering the chance of metastatic disease development [21]. The exact correlation between types of food and PCa is still unknown with unclear pathway. Further examinations should address these correlations in more detail.

Selenium was initially considered to lower the incidence of PCa. Results from other studies presented a moderate decrease in PCa risk with high serum selenium intake [22]. However, additional studies failed to replicate these findings and suggested no association between PCa and selenium serum level [23]. In recent cohort studies involving selenium and Vitamin E in a chemopreventive nutrient trial, no associations were discovered between serum selenium level and PCa [24, 25].

1.1.5 Obesity

Obesity is one of the public health challenges that society faces, as it has increased rapidly among the general population. Obesity is related to various diseases and types of cancer (e.g. breast and colon cancer). Obesity was not considered as a risk factor for PCa until recently. Obese men would have a higher risk of aggressive diseases with a lower chance of nonaggressive diseases if they were affected with PCa [26, 27]. This finding is potentially biased due to the difficulty of diagnosing PCa in obese men. To briefly explain, obese men have a larger volume of blood compared to non-obese men, this, in turn, will influence the PSA serum level to the lower range. Larger prostate sizes in obese men have a higher chance of missing the tumour during biopsies. Obesity has also been

found to have an adverse impact on the sensitivity of digital rectal exams (DRE) [28, 29].

Obesity does not only affect the diagnosis of PCa, but it has an impact on treatment options and outcomes. After a prostatectomy and external radiation therapy, obesity was linked to biochemical failure. Furthermore, obesity is associated with a greater rate of complications and poor side effects after androgen-deprivation therapy as well as higher rate of PCSM [30, 31]. Obesity has been linked to increasing serum Insulin-like Growth Hormone (IGF-1), which has a strong linkage to increasing PCa risk [32].

1.2 Anatomy and Histology of Prostate Gland

1.2.1 Prostate Gland Anatomy

The prostate gland is one of three accessory glands of the male genital reproductive system besides seminal vesicles and bulbourethral (Cowper's) gland. It is a funnel-shaped organ, located in the true anatomical pelvic boundary. The prostate base is immediately below the bladder neck, and the apex is just above the urogenital diaphragm. The proximal half of prostatic urethra runs steeply downwards and forward through the center of the gland, then at the level of verumontanum (mid prostatic urethra) it twists anteriorly [33]. The anterior prostate surface is slightly concave and is located behind the pubic bone and connected to it with the puboprostatic ligament. The posterior surface is horizontal with a midline depression in contact with rectal ampulla. The prostate is separated from the rectum by a dual film thin like fascia termed "Denonvillier's Fascia." Extraperitoneal fat surrounds the prostate in the space of Retzius anteriorly, where the prostatic dorsal venous plexus is found. The venous plexus is responsible for the blood supply and drainage of the penis. The levator-ani muscles surround the lateral surface of the gland bilaterally. The prostate is pierced by ejaculatory ducts on the posterior surface laterally and run obliquely and forward towards the posterior surface of the urethra at the level of verumontanum where they join the prostatic urethra [34].

The essential and central landmark of the prostate gland is the urethra, which has an average length of 3-4 cm and a mid-urethral 35° angulation anteriorly. The urethral curvature divides the urethra into two sides: proximal and distal with an almost identical length. The verumontanum structure arises from the posterior wall of the urethra where this bend occurs. It continues and points distally to form the crista urethralis [35] (**Figure 1.3**). The majority of prostatic acini and ejaculatory ducts open in the verumontanum. The periurethral glands of Littre, which have a smaller opening are found along the whole length of the urethra. A circumferential muscle sheath layer covers the entire urethra and is attached between the two urethral sphincters. Proximally, the circumferential sheath contains smooth muscle with the role of preventing retrograde ejaculations. Distally, the apex region consists of smooth and striated muscle, which has a primary role in micturition control [36].

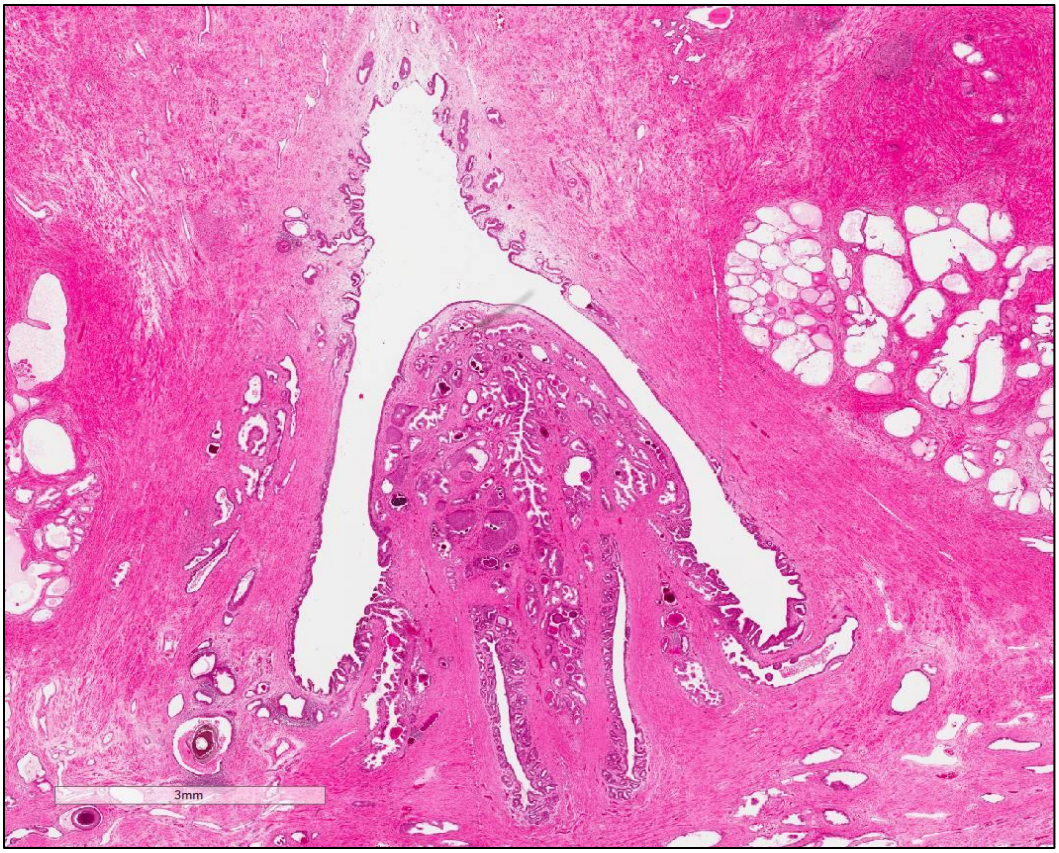

(**Figure 1.3**) **The urethra structures at the level of verumontanum**. Low magnification of a prostate tissue section with hematoxylin and eosin stain showing urethral structure at the level of verumontanum and crista urethralis, an opening site for prostatic glands and ejaculatory duct.

1.2.2 Embryology of the Prostate Gland

The prostate gland and the adjacent structure develops from 2 different origins. The prostate gland arises from urogenital sinus that develops from epithelial buds, while the Seminal Vesicles (SV), Epididymis, Vas Deferens (VD) and Ejaculatory Ducts (ED) develop from the Mesonephric Duct (Wolffian duct). The mesenchyme stimulates the urogenital sinus epithelium proliferation, ductal morphogenesis, and differentiation. Through the feedback loop mechanism, the epithelial tissue signals the mesenchyme tissue (undifferentiated connective tissue) to proliferate and differentiate into smooth muscle cells around the epithelial ducts. This development is under the regulation of androgen produced from the testis, which is considered the growth factor promoter to the prostate gland [37, 38].

The mesenchymal tissues continue growing to evolve the dome-shaped base of the prostate. During the mesenchymal growth, the ejaculatory duct formation continues to grow and proliferate towards the future verumontanum structure at urethral midway. The area around the ejaculatory duct continues to proliferate and form the central zone of the prostate. By the 10th week of embryonic life, the epithelial buds begin to branch mainly from the posterior and lateral regions of the urethral wall. The prostate duct formations and solid epithelial tissue continue to grow after birth at a very slow rate with a constant prostate size (less than 2 cm in diameter) until puberty [35, 38]. By the age of 20, and under the effect of androgen on the prostate, the gland reaches approximately 20 g in weight and remains within this range until the age of 30.

1.2.3 Microscopic Anatomy of the Prostate Gland

According to Dr. McNeal's model, the prostate gland is composed of glandular and non-glandular regions or districts that cannot be separated by gross anatomy. The glandular component contains Peripheral, Central and Transitional Zones that are only identified on a microscopic level. The non-glandular tissues are anterior fibromuscular stroma and prostatic capsule. Additionally, McNeal includes the

periprostatic and striated sphincters, nerve and blood supply within the non-glandular tissue component [39, 40].

1.2.3.1 Peripheral Zone (PZ)

The Peripheral Zone composes 70% of the prostate gland volume. It is the most common region for (chronic) Prostatitis, Prostatic Intraepithelial Neoplasia (PIN) and Carcinoma. It occupies the posterior, lateral and distal anterolateral area (apex) of the gland, which gives it a horseshoe shape. The peripheral zone ducts open into the urethra as a double row every 2 mm on the posterolateral surface for about 1.5 cm from the verumontanum proximally to the apex distally [36, 40].

The coronal section of the prostate gland demonstrates that the ducts of the peripheral zone occupy the lateral area around the distal urethra extensively at a 15° angle. The ducts are distant from the urethra toward the prostate capsule and have branches arched anteriorly and posteriorly giving origins to groups of acini. The acini are similar in shape and thickness. Also, the acini are distant from the urethra. Peripheral zone acini have a simple structure and are oval or rounded in shape surrounded by loose woven stroma and collagen **(Figure 1.4)** [33, 39, 40].

1.2.3.2 Central Zone (CZ)

The central zone composes 25% of the gland volume. It is responsible for 1-5% of the incidence of carcinoma and inflammation. The central zone is a cone-shaped structure that encloses the Ejaculatory Ducts (ED) with its base distal to the bladder neck, and its apex pointed at the verumontanum. The base of the prostate gland is formed mostly by the CZ. The ducts open in the verumontanum just around the ED orifices and fan out towards the base. The central zone acini display more complex structure than the peripheral and transitional zones. The acini are larger in size, particularly towards the capsule with papillary folding and intraluminal ridges, which resemble a cribriform appearance. This cribriform glandular structure shape is occasionally misidentified as Prostatic Intraepithelial Neoplasia (PIN). The central zone has a higher stromal to epithelial ratio

compared to other prostatic tissues. The stroma consists of compact interlacing smooth muscle bundles **(Figure 1.5)** [33, 36, 40].

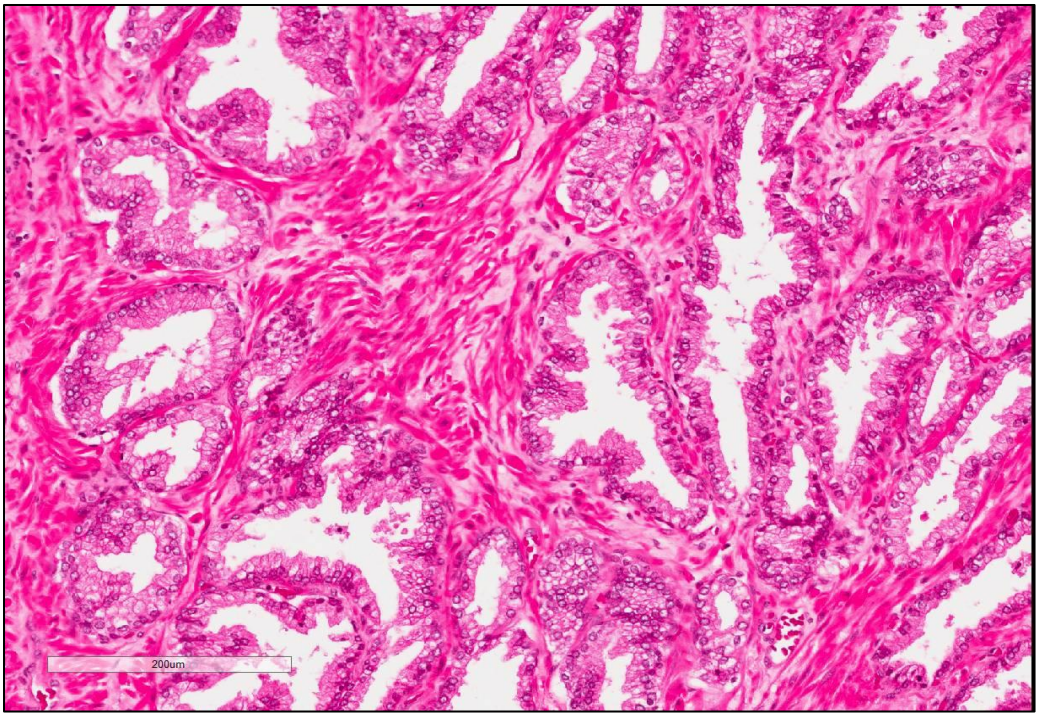

(Figure 1.4) Peripheral zone. Simple rounded or oval glands with loose woven stroma in between. 20X magnification power.

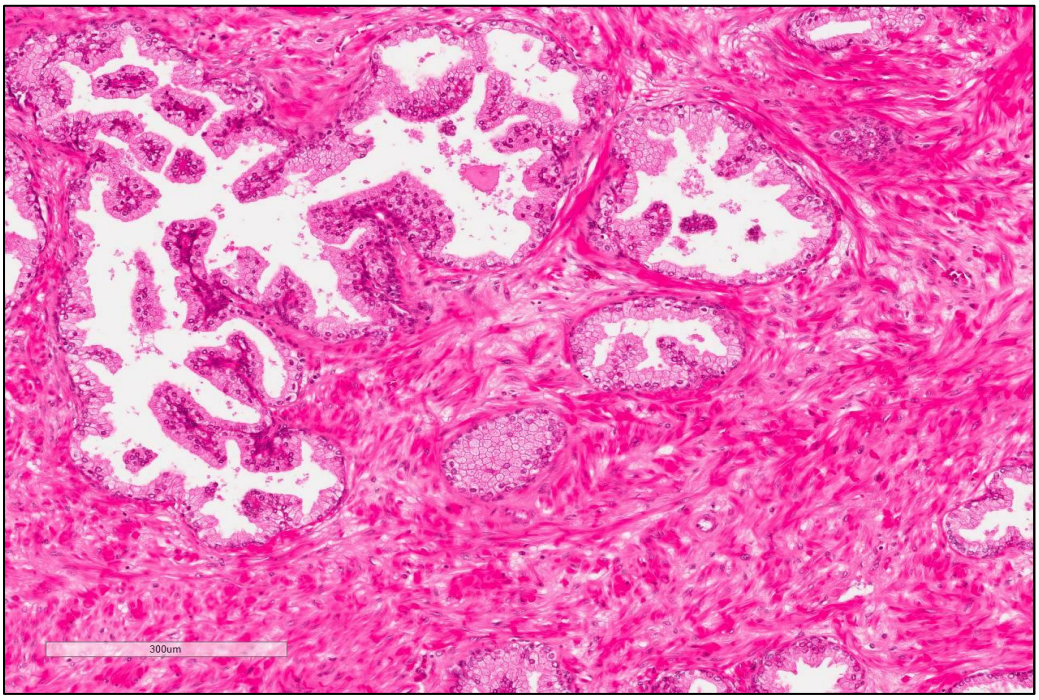

(Figure 1.5) Central zone. Glands structures are more complex (Cribriform) with compact interlacing stromal appearance. 15X magnification.

1.2.3.3 Transition Zone (TZ)

Initially, the Transition Zone (TZ) was not described by Dr. McNeal until 1978. He published a report in 1972 stating that Benign Prostatic Hyperplasia (BPH) arised from periurethral glands. He concluded that it is a benign nodular hyperplasia of the prostatic urethra [41]. The new anatomical concept emerged after the fundamental change in Dr. McNeal's report in 1978 stating that the origin of BPH is in the transitional zone [42, 43]. The TZ surrounds the proximal prostatic urethra, forming about 5% of prostatic volume, however, it can grow significantly and become more than the remaining prostate tissue combined. The TZ ducts exit the urethra as a single slit on the posterolateral surface just proximal to urethral angulation occurrence. The ducts extend laterally and curve sharply anteriorly and branches in the direction of the bladder neck. There is a clear boundary between TZ and the residual glandular tissue made by fibromuscular tissue, which enables its visualizations by transrectal ultrasound. The acinar component of the TZ is similar to the PZ with a small rounded or oval structure encircled by more compressed stroma composed of a compact, dense, interlacing smooth muscle bundle. This smooth muscle blends with pre-prostatic sphincter stroma and Anterior Fibromuscular Stroma (AFMS) [33, 40].

Rather than BPH, the TZ is responsible for 20% of prostate carcinoma. Pathologists refer to PZ and CZ as outer prostate or non-transition zone and the TZ and AFMS as the inner prostate [44]. Transition zone cancer is usually large in volume with high PSA serum level, although it is accompanied by low Gleason score [45]. Cancer arising from TZ is associated with high risk of bladder neck involvement with anterior positive surgical margins and low risk for neurovascular bundle invasions, Extra Prostatic Extension (EPE) or Seminal Vesicles (SV) [45, 46].

1.2.3.4 Anterior Fibromuscular Stroma (AFMS)

According to Dr. McNeal's description, AFMS is an apron of wedge-like shaped tissue. It runs from the bladder neck over the anteromedial surface of the prostate proximally and becomes narrow distally to connect with the prostatic urethra at

the apex [40]. It is attached to the periprostatic sphincter and Transition zone from its posterior dorsal surface proximally, and the semicircular striated muscle towards the apex distally. The lateral margin of AFMS interlaces with prostatic capsule laterally above, providing cover to most of the anterior margin of the PZ. The AFS structure is similar to the bladder neck with a large compact smooth muscle bundle. However, these smooth muscle bundles are more randomly oriented and are divided in between with bands of dense fibrous tissue [33, 36, 40].

1.2.3.5 Prostate Capsule

The capsule of the prostate gland consists of a dual layer, a smooth muscle layer located internally with the collagen layers externally. The inner smooth muscle layer grows transversely and inwards to blend with the smooth muscle surrounding the prostatic glandular acini. Clear identifications between the two layers is quite difficult even with the assistance of viewing these layers on the microscopic level [35]. To further explain this difficulty, the multilayer collagenous fascia surrounds the gland, which varies in thickness across the different areas of the prostate. This fascia may blend with the capsule depending on the location. The capsule is ill-differentiated and contains varied tissue between smooth muscles, striated muscles and fibrous tissue in the region of the apex. The inconsistency of prostate capsule structure leads to not being considered as a real anatomical feature [47, 48]. Since the prostate gland is surrounded by abundant amounts of adipose tissue, pathologists use this as a landmark for extra-prostatic tissue identification and the assessment of cancer spreading outside the gland in prostate biopsy or total prostatectomy specimens.

1.2.4 Vascular Supply

The arterial supply to the prostate originates from two sets of arteries on each side, known as the superior and inferior prostatic pedicles. Commonly, the superior prostatic pedicle (prostate artery) is a branch of the prostatic-vesicular artery that supplies the inferior bladder portion and seminal vesicles. The origin of the prostate artery is variable. For instance, the cadaveric specimens study

demonstrated that the prostate artery might originate from other roots [49]. The prostate artery then divides into two branches adjacent to the base of the prostate gland laterally, the urethral artery (medial branch) and the capsular artery (lateral branch). The urethral artery is responsible for blood supply to the proximal prostatic urethra until the crista urethralis, transitional zone, and paraurethral glands. It penetrates the gland on prostatovesicular junction proceeding in a perpendicular course in relation to the urethra before having a 90° angle turn to run parallel to it. The capsular artery has a caudal descending direction towards the apex and external to the prostatic capsule. Capsular artery has perforated branches that penetrated the prostatic capsule providing blood supply to the prostate capsule, central zone, and distal urethra. The capsular artery receives various anastomosis from the inferior prostatic pedicle branch after forming plexus around the distal prostate-urethral junctions [34, 50, 51].

1.2.5 Neurovascular Bundles of the Prostate

The prostate neurovascular bundles are formed on a groove between the posterolateral borders of the prostate anteriorly and rectum posteriorly. It consists of the cavernous nerves that arise from the pelvic plexus to supply corpora cavernosa and corpora spongiosum after entering the helium of the penis inferior to the pubic bone. It has a major role in erectile function. This gives the bundle its significant surgical landmark due to the direct impact on post-surgical recovery as well as resuming erectile function and sexual activity. The cavernous nerves are joined by arterial and venous branches from the prostatovesicular artery and veins admixed together to form the bundle. The bundles run between the prostatic fascia medially, and levator ani muscle fascia laterally. The cavernous nerves contain sympathetic fibres originating from T11 to L2 ganglia as well as parasympathetic elements originating from ventral rami of S3 and S4 [34, 52].

1.2.6 Normal Histology of the Prostate Gland

The essential physiological function of the prostate gland is to sustain nutrition to sperms during ejaculation with quick and efficient ejections of small volumes of fluid. The prostate has a large storage capacity with a low secretory volume. The

muscular component allows the gland to carry out these functions [35]. The ducts and acini are both lined with tall columnar secretory epithelium cells with pale to clear cytoplasm, secretory vacuoles, and dark nuclei. The secretory vacuoles are tightly packed in PZ and TZ; however, they are wider and less dense in the CZ [33, 35, 39]. Secretory cells produce Prostate-Specific Antigen (PSA) and Prostate Specific Acid Phosphatase (PSAP) from all prostate zones. Also, they produce pepsinogen II, lactoferrin, and plasminogen activator from the CZ. They stain positive with PSA and PSAP and negative with high molecular weight cytokeratin stain due to the lack of immunoreactivity [35].

The secretory cells are found on the layer of basal cells, which are isolated from the basement membrane and stroma. Basal cells are flattened, elongated in shape, with slender dark nuclei and are progressively scant or with no cytoplasm comparable to fibroblasts. They are arranged parallel to the basement membrane. Occasionally, the basal cells are not seen, or they may be presented partially around the ducts and acini of the prostate gland. Basal cells stain positive for high molecular weight cytokeratin or P63 stain. They are absent in the existence of adenocarcinoma.

The distal ducts near the urethra are lined with urothelial cell similar to the urethral epithelium. The urothelium is a spindle-shaped like cell with scant cytoplasm. The nucleus sustains a nuclear groove. The long axes of these grooves are parallel to the basement membrane [35, 39].

The last epithelial cell type is endocrine-paracrine cells that has unknown physiologic functions. They are found between the basal and secretory cell with the lateral dendritic process [39]. These cells are not easily identified with routine Hematoxylin and Eosin staining (H&E), that require special immunohistochemical stains of antibodies like chromogranin A, serotonin, and neuron-specific enolase [53, 54]. Although, the paracrine cell function is still unknown, they contain serotonin granules and various peptide hormones such as somatostatin, calcitonin, and bombesin [33, 35, 39, 54].

1.2.7 Mimickers of Prostate Cancer

Pathologists face a challenging task in diagnosing PCa, especially in a small glandular amount in well differentiating cancer lesions or other deviations from normal histology tissue. The mimickers are classified according to their glandular size in comparison to Gleason scoring. There are small, medium and large glandular size mimickers. However, the majority of mimickers fall into the small gland category [55].

The following section discusses three noncancerous pathological lesions. We have observed that atrophy, Prostatic Intraepithelial Neoplasia (PIN), and Benign Prostatic Hyperplasia (BPH) were the major confounders of prostate cancer on MRI (discussed further in section 3). These lesions can result in a false positive cancerous-like signal in MRI on prostate gland images.

1.2.7.1 Atrophy

Atrophy is one of the most common discoveries in prostate tissue during biopsy or retrieval of the whole prostate specimen from radical prostatectomy. There are two main characteristic types of atrophy, diffuse and focal. Androgen deprivation is responsible for diffuse atrophy whether through orchiectomy, surgically or chemically through antiandrogen or luteinizing releasing hormone agonists [56]. Focal Atrophy has no known link to androgen deprivation, however, earlier studies refer to focal atrophy as a part of aging. Other research studies have indicated that focal atrophy could be a result of either acute or chronic inflammation [35, 57].

The focal atrophic glands are typically heterogeneous patches, distorted and relatively small in size. They are accompanied by flattened epithelium and hyperchromatic nuclei. Some focal atrophic acini are present with the complete lack of a basal cell layer [56]. There are multiple variants for atrophic gland subtypes. Nevertheless, these subtypes share the same main histologic features. No challenges exist in identifying atrophic glands with high power magnifications except for Post-Atrophic Hyperplasia (PAH). The challenges the pathologists face in recognizing PAH are owed to the increase of the cytoplasmic basophilic

appearance and increase in acinar architecture. Other types of atrophic glands are conceivably mistaken with adenocarcinoma on low power magnifications. Four distinctive variants of prostate focal atrophy are discussed further.

1.2.7.1.1 Simple Atrophy (SA)

The first typical variant and the most common type of atrophy is known as the Simple Atrophy (SA). The acini appear basophilic on a low-power magnification due to the diminished amount of cytoplasm. Although the acini appearance are irregular and angulated, they still appear within a relative average calibre. The cells are reduced in the cytoplasm with no change to the nucleus size and shape with the nucleoli appearing smaller with chronic inflammation. In summary, they are mimicking adenocarcinoma **(Figure 1.6)** [35, 56].

1.2.7.1.2 Post-Atrophic Hyperplasia (PAH)

The acini in PAH are small and rounded with a lobular arrangement **(Figure 1.7)**. They are often accompanied by dilated ducts called feeder ducts, resulting in the appearance of resting breast lobules. Therefore, some authors and pathologists termed PAH as lobular atrophy [56]. PAH is basophilic in appearance with low cuboidal cell shape, scant cytoplasm and a small to a medium-sized nucleus with mild to moderate enlargements compared to adjacent normal epithelial cells. This results in the confusion with adenocarcinoma [35, 56, 58]. A tight arrangement of multiple small acini raises the impression of tissue proliferation when relating to normal tissue and hyperplasia expression [59].

Although the basal cell layer is present in PAH acini, it is rarely identified with a light microscope using a hematoxylin and eosin stain. The basal cells are present and appear in a distorted and fragmented layer with the use of immunohistochemically high-molecular-weight cytokeratin stain. The PAH is associated with stromal involvement. Stromal changes are varied and are capable in presenting as a smooth muscle atrophy to dense sclerotic changes that have a significant impact on acini shape and luminal space [58].

PAH is commonly associated with chronic inflammatory cells in the adjacent stroma or the luminal space [56]. PAH represents the most extreme form of morphological changes of atrophic acini, which may be misdiagnosed as an adenocarcinoma followed by unnecessary treatment intervention.

1.2.7.1.3 Simple Atrophy with a Cystic Formation

The acini in simple atrophy with cystic formation reveal that shape and diameter vary. They range from a small to large calibre that produce a sieve-like appearance in the gross sections as well as cystic-like appearances under the microscope. The acini are arranged tightly with little to no stromal in-between. The cells have a little cytoplasm. There is no relation observed between simple atrophy with cystic formation and chronic inflammation [35, 56] **(Figure 1.8)**.

1.2.7.1.4 Partial Atrophy

In contrast with the various types of atrophy, partial atrophy acini have a non-basophilic appearance on low magnification. The cytoplasm is reduced in the partial atrophic epithelial cells compared to the normal glandular epithelium. The majority of cytoplasm commonly presents laterally to the nucleus leading to enhanced internuclear spaces. This results in a low-to-pale appearance on low power magnification **(Figure 1.9)**. The partial atrophic glands may become present in small to medium sizes with intraluminal dark pinkish or crystalloid secretion that could mimic adenocarcinoma of the prostate. Partial atrophy is frequently viewed as simple atrophy presenting the proposition to consider that partial atrophy as a stage of atrophic changes [35, 56].

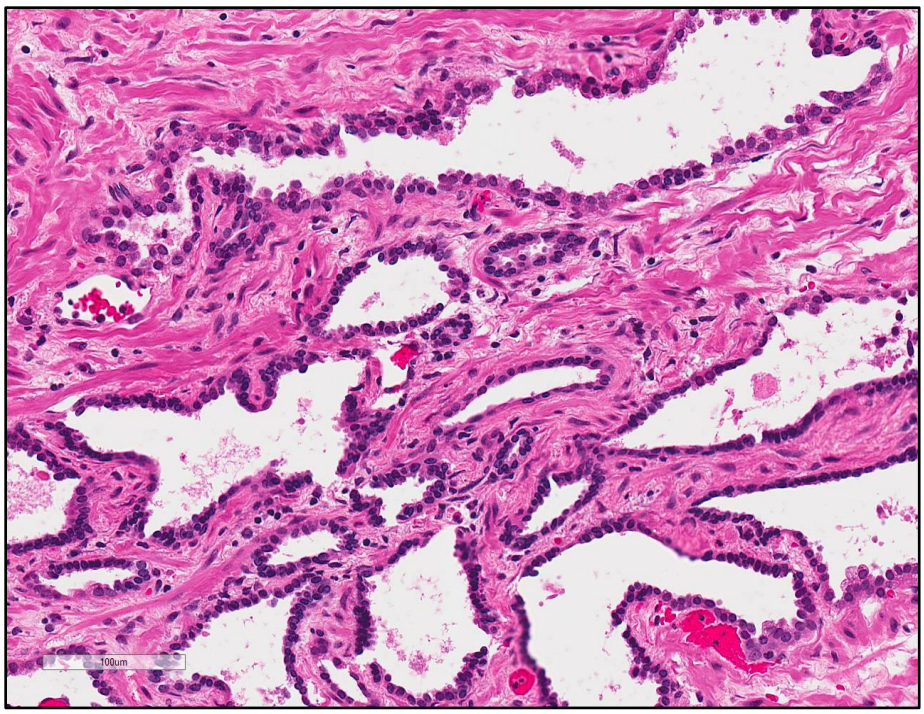

(Figure 1.6): **Simple Atrophy**. Angulated glands with basophilic appearance with very low to no cytoplasm with normal size, dark nuclei. 20X magnification.

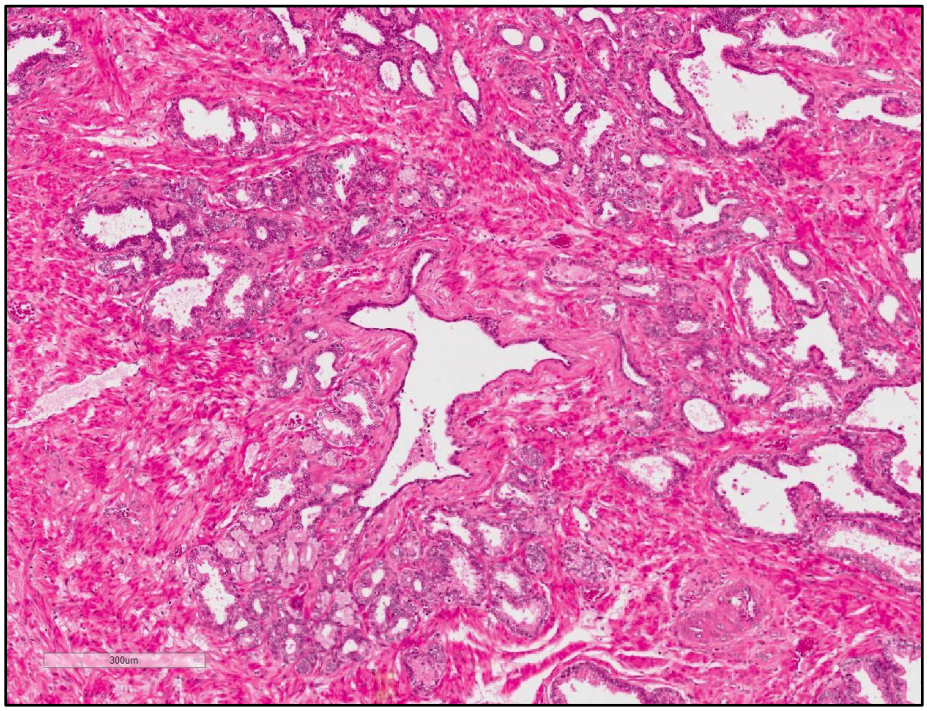

(Figure 1.7) Post-Atrophic Hyperplasia (PAH). Low power image shows a central dilated duct (feeding duct) surrounded by atrophic acini.

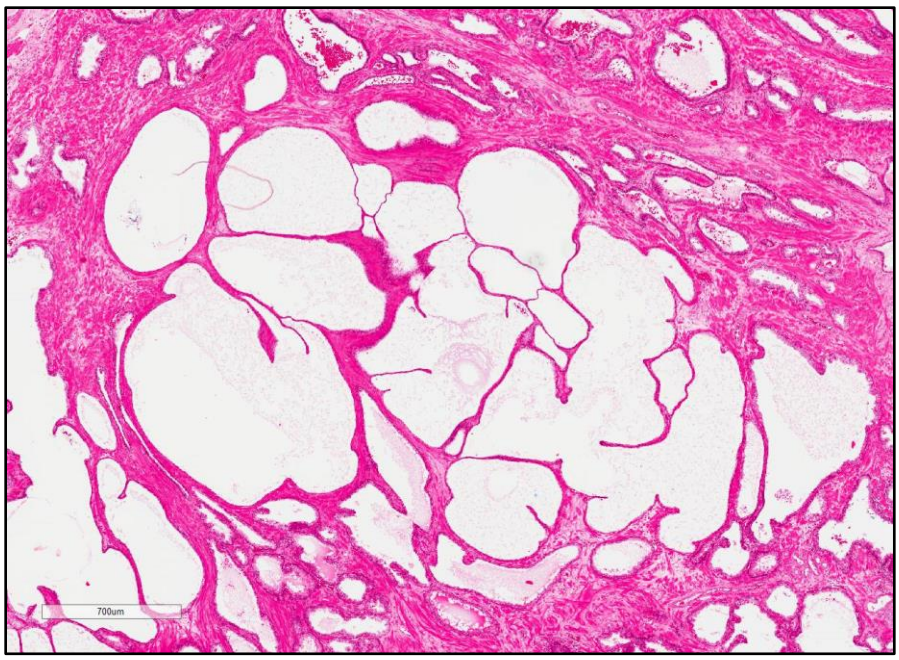

(Figure 1.8) Simple atrophy with cystic formation. Simple cystic atrophy, distinctive with medium to large calibre glands, rounded in shape with no or very little cytoplasm. 10X magnification.

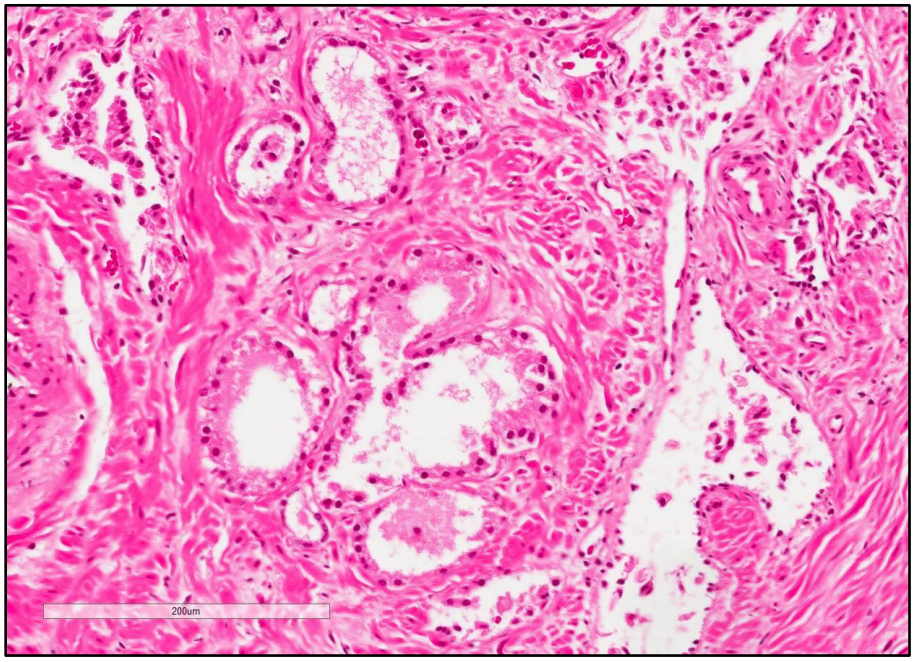

(Figure 1.9) Partial atrophy. Pale cytoplasm is laterally positioned with increased internuclear distance. Glands are also with pink to eosinophilic Intraluminal secretion. 15X magnification.

1.2.7.2 Prostatic Intraepithelial Neoplasia (PIN)

Historically, McNeal and Bostwick described PIN as premalignant lesions and identified it as a intraductal dysplasia [60]. Previously, PIN was classified into three categories according to epithelial dysplasia; mild, moderate and severe. Pathologists currently use a newer classification, which includes only two classes, low-grade, and High-Grade PIN (HGPIN). HGPIN is considered the most acceptable PCa precursor by many Pathologists. With a morphology similar to prostate adenocarcinoma, HGPIN denotes a pre-invasive state to a cellular hyperplasia of prostatic gland [61]. Not only do PIN and PCa share comparable morphological features, but they also have similar epidemiological criteria regarding age and race. A strong relationship is identified between advanced age and incidence, size, and multifocality of PIN diagnosis. PIN has been reported in men as early as 20 years of age, however, these findings were associated with to low-grade PIN [62]. HGPIN and PCa have a high incidental rate in African American men compared to Caucasian men and other race groups. In contrast, no significant associations have been found between HGPIN and the increase of free or total PSA serum level [61-64]. This limitation leads to the conclusion that prostate biopsy is the only current method of detection and screening for HGPIN. The specific criteria to distinguish between low and high-grade PIN includes prominent nucleoli and more atypia in HGPIN [60]. A wide range of intra-observer variability exists with over or underdiagnosis of HGPIN in Pathologists' reports.

Low-grade PIN glands demonstrate slight epithelial proliferation and crowding with some irregular spacing. The nucleus criteria includes a slight enlargement accompanied by a thin membrane and normal chromatin activity. The basement membrane and basal cell layer are continuous and intact [65].

However, HGPIN consists of benign glands with some architecture abnormalities in prostate glands acini, the main feature of its diagnosis is nuclear atypia with close features to cancerous cells rather than normal epithelium.

Extensive volume and multifocal HGPIN have a high predictive value for increasing frequency, amount, and severity in the presence of PCa [61]. Both HGPIN and PCa have a greater chance arising from the peripheral zone. They demonstrate similar nuclear features and correlate with epithelial dysplasia [65]. HGPIN and PCa share heterogeneous features with multifocal presence. PIN associated with increased angiogenesis similar to changes that occur with PCa, which is used as evidence to consider PIN as a PCa precursor. These characteristics in HGPIN make it one of the mandatory standard diagnosis remarks in prostate biopsy or radical prostatectomy pathology reports [61].

HGPIN glands display glandular enlargement with four main patterns, tufting (most common), flat, papillary, or cribriform. Unusual patterns include signet ring cell, foamy glands, small cell (neuroendocrine), hobnail, and squamoid [66]. There is no clinical significance between patterns. The majority of cases will demonstrate most of the histological patterns existing at the same time. The acini are separated by a different amount of stroma. Their characteristic features include nuclear enlargement and overlap with hyperchromatic evidence add-ons to the increase of nuclear-cytoplasmic ratio, epithelial hyperplasia, and amphophilic cytoplasm. The nuclear membrane gets thickened with enlarged nucleoli. These features are responsible for the PIN basophilic appearance on low magnification power. The basement membrane is present with disruption to the basal cells [65]. The HGPIN nuclei are located closer to the gland's center compared to the nuclei close to the basement membrane in normal glands [60].

The specific immunohistochemical staining (High molecular weight cytokeratins, CK5, p63) is used to distinguish between HGPIN and in particular with the cribriform pattern of Gleason grade 4 in the prostate biopsy **(Figure 1.10)**. PIN glands show micropapillary form similar to breast micropapillary intraductal carcinoma with more crowded and piled up nuclei.

The primary incidence of the HGPIN finding and risk of PCa are assumed to be a 50% chance on prostate biopsy. However, later studies showed that the median

risk of diagnosing PCa after HGPIN detection is about 21% [67, 68]. The majority of Pathologists agree that the detection of HGPIN on needle biopsy warrants a follow-up biopsy [69].

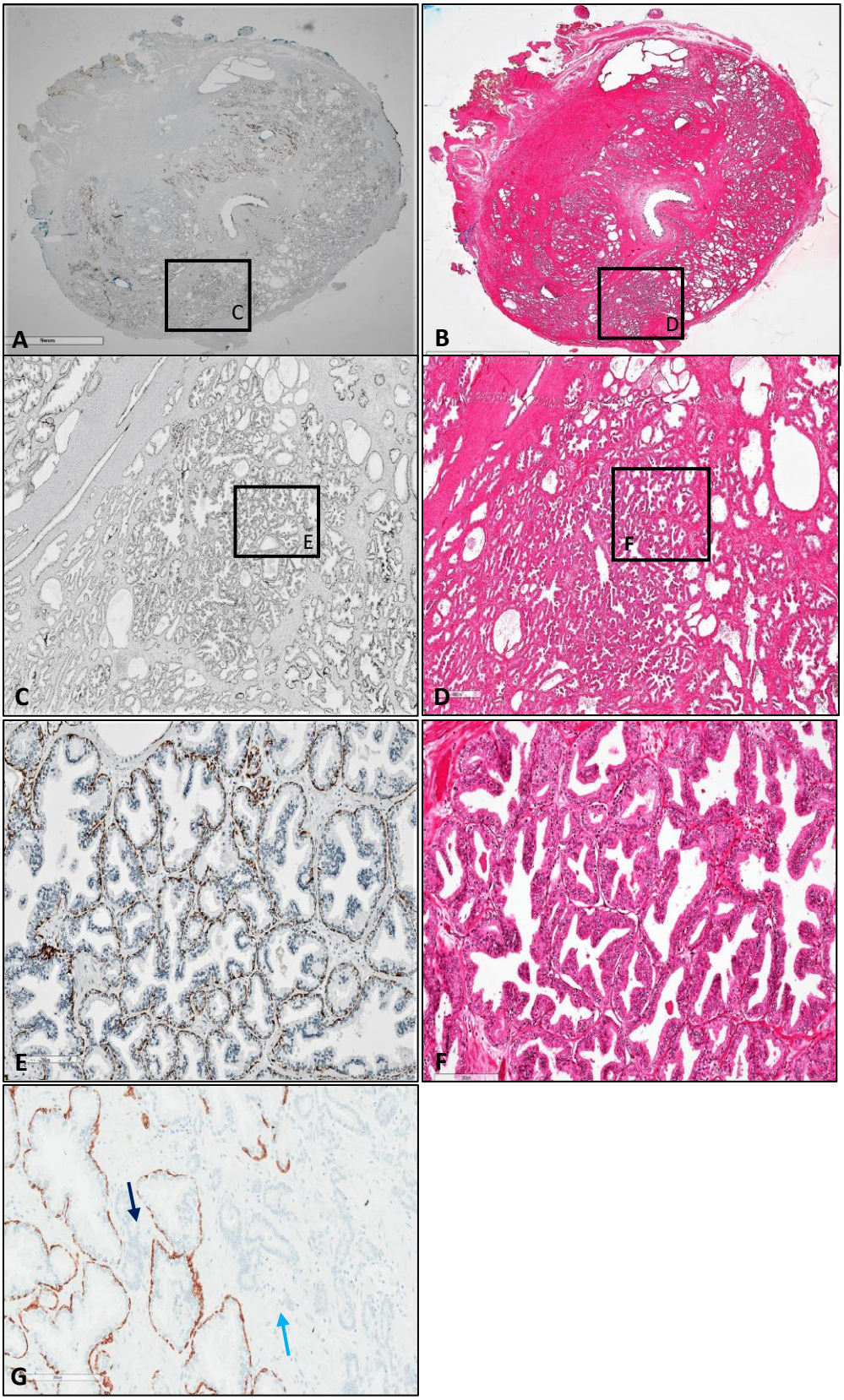
A
C
B
D
C
E
D
F
E
F
G

(Figure 1.10) Histopathology digital images for a whole-mount prostate section with PIN features. (A) Prostate whole-mount section image stained with high molecular weight cytokeratin immunohistochemical stain (CK) compared to the same prostate section stained with Hematoxylin & Eosin staining (H & E) (B). (C) a 10 times power zoom shows the same section area containing glands with the cribriform type of high grade prostatic intraepithelial neoplasia stained positive with cytokeratin in the image (C) and (H & E) staining in the image (D). A high-power zoom of the same section with the area containing PIN, stained with cytokeratin in the image (E) and with (H & E) stain on image (F). Note PIN glands stain positive with cytokeratin (dark blue arrow) compared to the negative stain with prostate adenocarcinoma glands (cyan arrow) in the image (E).

1.2.7.3 Benign Prostatic Hyperplasia (BPH)

Nodular hyperplasia or BPH is considered one of the benign conditions of the prostate. It involves an enlargement of the transitional zone and the area around the urethra due to the proliferation of epithelium and stromal tissue. This proliferation creates pressure on the prostatic urethra along with prostatic sphincter. The significant pressure is responsible for a set of symptoms termed Lower Urinary Tract Symptoms (LUTS). These symptoms include increased urinary frequency, urgency, weak urine stream with diminished force and size, incomplete void and nocturia [70]. The transitional zone hyperplasia also accounts for prostate gland outline deformity. The enlargement of the transitional zone in the direction of the apex leads to diminishing the anterior fibromuscular stroma due to stretching and increasing the anteroposterior gland dimension. Additionally, the peripheral zone is compressed and thinning due to lateral growth resulting in increasing the gland width [35, 71].

BPH is predominant at an advanced age sharing some similarity with prostate cancer. However, it is not considered as a PCa precursor. 10% of the BPH cases are found to be associated with PCa, and they are discovered accidentally during transurethral prostatectomy resection procedures [72]. An advanced age increases the risk for BPH and PCa, in addition, both might respond well to androgen deprivation [73].

BPH usually replaces the entire transitional zone **(Figure 1.11)** and consist of multiple, individual, nodules, that differ in size and shape. Grossly, these nodules are varied between soft, firm or rubbery in consistency and yellowish-gray in color. There are two subtypes of BPH, depending on predominant tissue proliferation, epithelial hyperplasia **(Figure 1.12)**, and stromal hyperplasia **(Figure 1.13)**. Grossly, the epithelial nodules have a spongy like appearance that bulges on the cut surface which is oozing a pale, white, and watery like fluid. The predominant stromal BPH consists of fibrous connective tissue and smooth muscle present with trabeculation or diffuse enlargement with no nodule

formation. The majority of BPH nodules contain all elements with varying extent in each nodule.

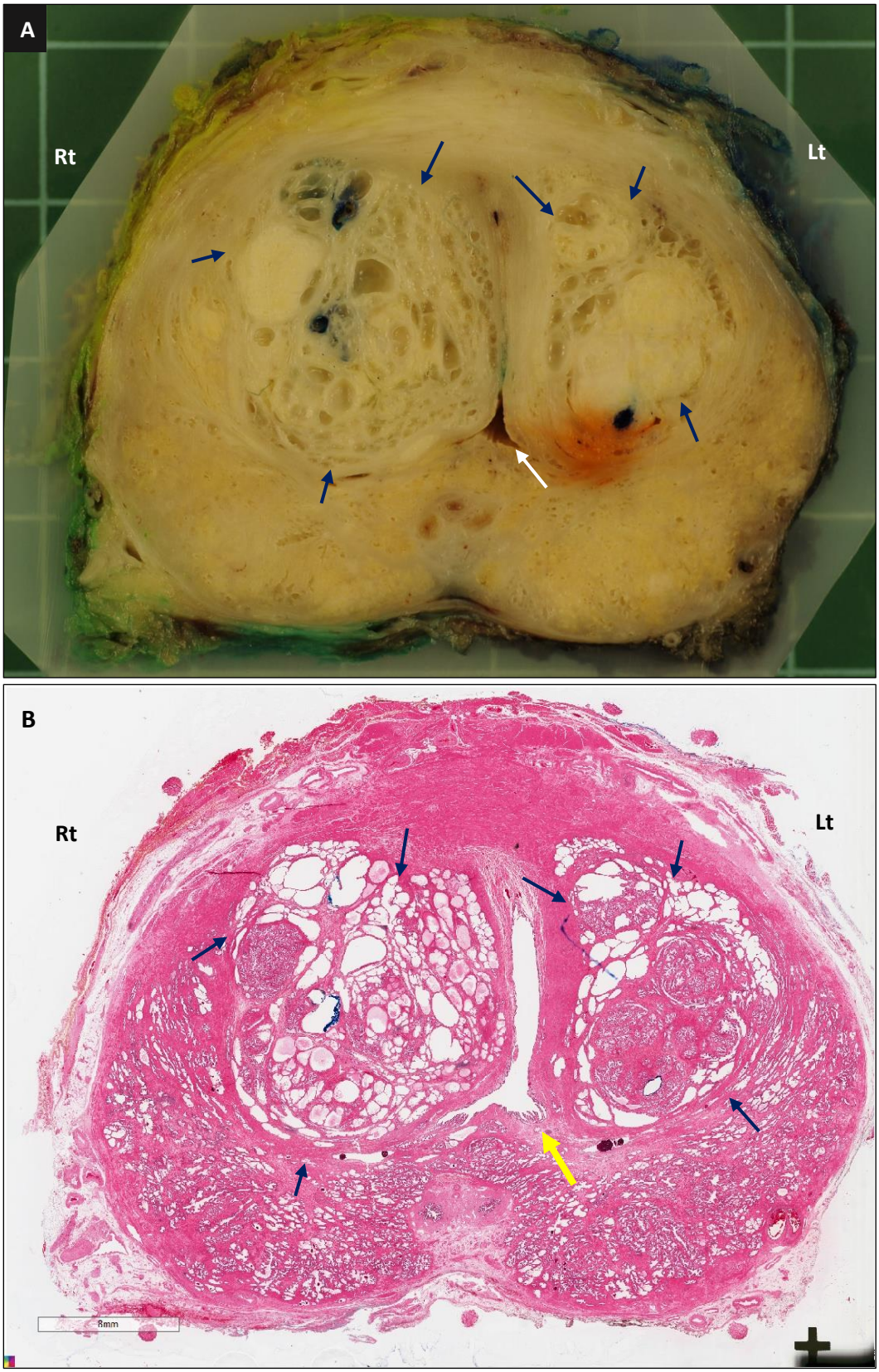
A
Rt
Lt
B
Rt
Lt
8mm

(**Figure 1.11**) **Whole-mount prostate formalin block with BPH features and their digital (H&E) histopathology image**. Whole-mount prostate formalin block (A) shows two yellowish-grayish large transitional zone hyperplasia with a spongy appearance (blue arrows) adjacent to the Urethra (white arrow) bilaterally. Right side nodule is more significant than the Left side. The same section presented in image (B) with Hematoxylin and Eosin stain (H&E) demonstrates a large transitional zone with benign prostatic hyperplasia (blue arrows) on each side of the urethral structure (yellow arrow).

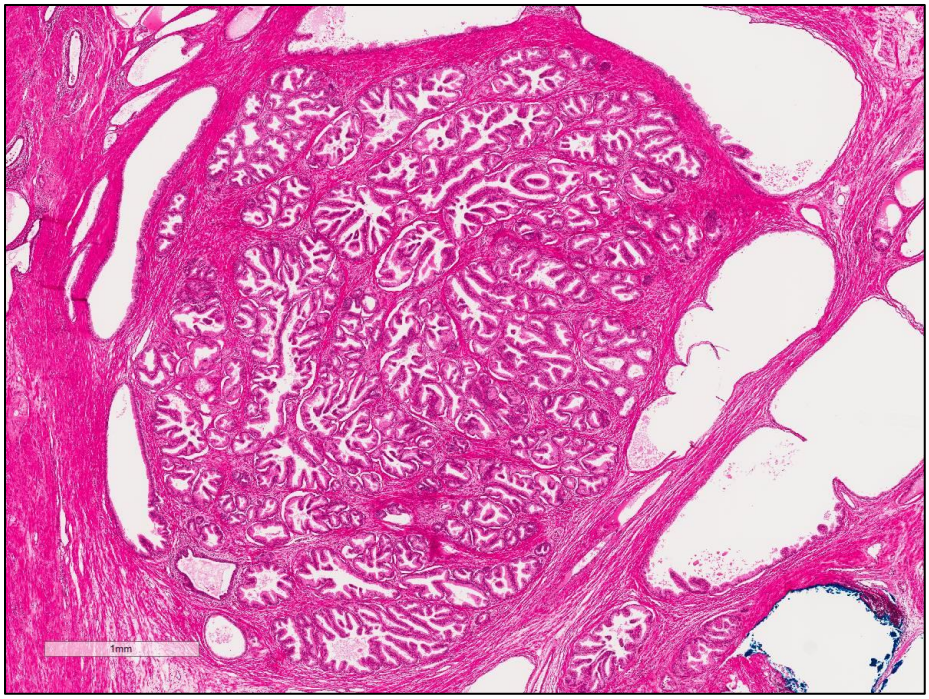

(Figure 1.12) The glandular element of BPH, also known as epithelial element in the transition zone of the prostate gland. 10X magnification

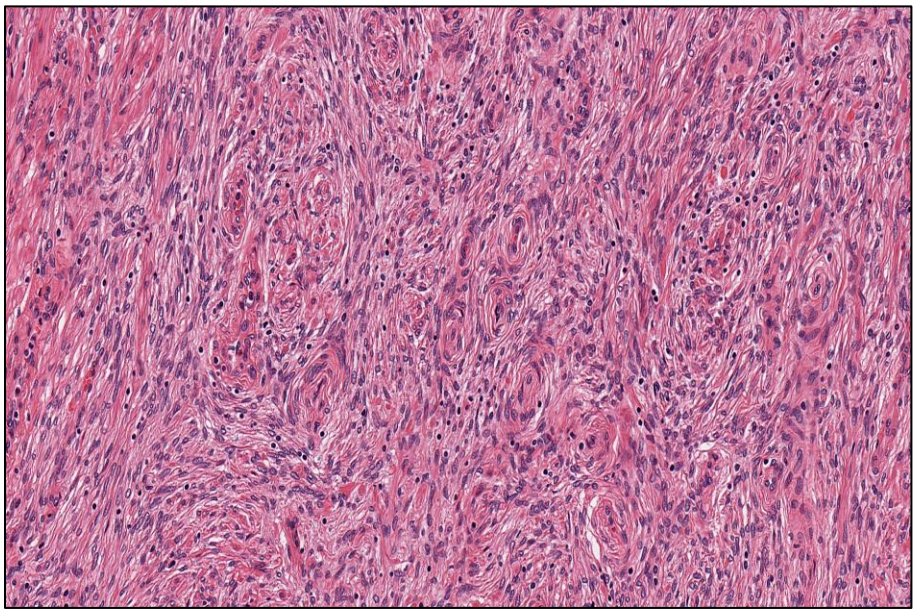

(Figure 1.13) The stromal element of Benign Prostatic Hyperplasia (BPH). High power image showing stromal element in the transitional zone of the prostate gland consists of fibrous connective tissue and smooth muscle.

1.3 Screening

Improvement in the management and treatment of cancer, in general, is owed to a unique collaboration between five disciplines including screening and early detection programs, imaging, surgery, chemotherapy, and radiation. In PCa, the current detection methods include Digital Rectal Exam (DRE), Prostate-Specific Antigen (PSA), which is a blood serum testing as initial screening followed by Transrectal Ultrasound (TRUS) guided biopsies.

1.3.1 Prostate-Specific Antigen (PSA)

Prostate-Specific Antigen (PSA) is a glycoprotein produced by the secretory epithelial cell in the prostate ducts and acini. PSA is also a serine protease of the Human Kallikrein family (HK-3). It is responsible for the release of spermatozoa from the seminal clots by dissolving and the breakdown of gel-forming proteins, improve sperm motility as well as soften the cervical mucus [74, 75].

PSA is synthesized as a proenzyme (pro-PSA) in normal and other pathological cells such as hypertrophy or cancer. The Pro-PSA is then secreted into the lumen of prostate ducts where it gets activated by removing the propeptide chain followed by inactivation of proteolysis. The active and inactive PSA leaks into the bloodstream through the capillary basement membrane after passing through the stroma and epithelial basement membrane. In the blood serum, the inactive PSA is unbounded and called (free-PSA) while the active form of PSA gets bounded by a protease inhibitor [76, 77]. Prostate cancer cells were found to produce more binding protein PSA. This lead to lower free-PSA in proportion to total PSA in prostate cancer patients [78].

The most commonly used value for PSA cutoff is 4 ng/ml, although this value is still controversial. The PCa probability with PSA level lower than 2 ng/ml is found to be around 2%. This probability is increased significantly to 18% with PSA levels from 2.5-4.0 ng/ml. The possibility of PCa is 22-27% for PSA values between 4.0 and 10.0 ng/ml, rising to 67% with PSA values more than 10.0 ng/ml [74]. Studies suggested lowering the PSA cutoff value to 2.5 ng/ml or even

further to 1.5 ng/ml to improve early cancer detection and a better outcome [79, 80]. However, dropping the cutoff PSA value will lead to increase the sensitivity and decrease the specificity, leading to an increase in the number of unneccesary biopsies [77, 80, 81].

Many factors should be measured for the optimum cutoff value for PSA. Factors such as age, race and medications can have a significant impact on the range of normal PSA values.

1.3.1.1 Age and Race-Specific PSA Range

The prostate gland tends to increase in size with age, affecting the amount of PSA produced by normal epithelial cells. As a result, it has been proposed that in men with no prostate cancer, a different standard reference range for each age group should be used (**Table 1.1**) [82, 83]. The PSA value is also affected by various ethnic and racial groups. Men of African descent were found to have a higher PSA average compared to those from Caucasian and Asian roots [77, 83, 84].

Since PSA is produced by normal and pathological cells, noncancerous lesions could affect the level of PSA, but not to the same extent as cancer cells. PSA could also be influenced by physiological functions like ejaculation, which increases the PSA level. Prostatitis, infarction, and BPH were found to increase PSA level. Locally invasive procedures such as prostate needle biopsies were also are found to increase PSA levels [76].

Medications such as 5-alpha-reductase inhibitor and Finasteride were used in the treatment of BPH and hair loss respectively were found to lower PSA levels by 50% with minimal effect on PSA produced by cancer cells. These medications could be used to enhance the efficacy of serum PSA testing to minimize the number of unnecessary prostate biopsies [85].

Age	PSA Specific reference range (ng/ml)
40-49	0.0-2.5
50-59	0.0-3.5
60-69	0.0-4.5
70-79	0.0-6.5

(Table 1.1) Proposed PSA Age-Specific reference range [82]

1.3.1.2 Free vs. Total PSA

Currently, the introduction of free PSA to total PSA ratio has improved the specificity of PSA in predicting and detecting PCa, in particular when total PSA is in a normal range (below 4 ng/mL) or in the gray zone (4-10 ng/mL). Men with PCa are found to have a lower percentage of free PSA compared to cancer-free men. The cutoff value of free PSA percentage around 25% or less was found to increase the risk of PCa by 95% and decrease unnecessary biopsies by 20% [86]. Other studies suggested adding the age as a considered influence [84]. In the circumstances of the standard Digital Rectal Exam (DRE) and PSA (4-10ng/mL), men with 70 years of age and above should use 16% of free PSA compared to 20% in men under 70 years old [87].

1.3.2 Prostate Cancer Diagnosis

Prostate Cancer (PCa) diagnosis is made through histological assessment and evaluation following a prostate biopsy. Since most PCa arises from the peripheral zone, it is unusual for PCa to cause any symptoms unless they are locally invasive to the urethra or if it produced distant metastasis. Before the era of PSA, abnormal DRE was the only reason for the prostate biopsy. Currently, abnormal PSA alone is sufficient to warrant a prostate biopsy even though the DRE is normal.

Prostate biopsy is achieved with the aid of Transrectal Ultrasound (TRUS), which can be used to assess the prostate volume as well as detect prostate lesions for biopsy. Any suspicious hypoechoic lesion within the prostate gland should be sampled, even though, not every hypoechoic lesion will be cancer positive. Some author proposed that only 18% of the hypoechoic lesions will produce positive tumour sampling [88].

Prostate biopsy was initially performed through a sextant pattern by obtaining one core bilaterally from the prostate gland base, mid-gland and apex. Increasing the number of core biopsies with more attention given to the lateral and apex zone sampling has increased the chance of cancer detection by 31% [89]. Many research studies focused on increasing the number of sampling cores with the relation to cancer detection rates. A 10-12 core biopsy pattern provides a balance

between cancer detection rate and lower morbidity and adverse effect rate [90, 91]. Some authors have reported no extra benefits in cancer detection rate from increasing core sampling number more than 12 cores [89-91]; however, this is still controversial.

Despite the chance of improvement in detecting PCa with an extended scheme of core sampling biopsy, it is still estimated to carry a false-negative rate. The detection rate in prostate biopsy reaches 39-52% using the assistance of MRI in high-risk patients after negative detection on previous or initial biopsies [92]. The challenging task with TRUS biopsy is not only to detect PCa but to identify and grade cancer for further and more effective management and treatment. Some studies proposed that only 28% of TRUS biopsy cases were associated with the same original Gleason score compared to the definite Gleason score found after radical prostatectomy [93]. The sensitivity of ultrasound to identify prostate tumour tissue is insufficient, as it depends on cancer volume rather than cancer grade, and is not consistent for detection of cancer in low-risk men with early-stage PCa [94].

1.4 Magnetic Resonance Imaging (MRI)

Multi-parametric MRI is used to assess multiple organ parameters in the same MRI imaging session. The sequences of the mpMRI protocol consist of T2W, DWI, and DCE. Optional MR spectroscopy imaging can also be added to the scan protocols [95]. MRI provides a detailed and clear anatomical and tissue image of the prostate gland structure. It also provides a high intrinsic soft-tissue informative assessment such as vascular condition, cellularity, and metabolic evaluation.

Using a surface phased array coil (pelvic-surface coil), the diagnostic accuracy performance was reported to be 77% overall with a sensitivity and specificity reaching 71% and 74% respectively [96]. The pelvic surface coil produces an image showing a respectable detailed anatomical pelvic structure, yet it does not establish an accurate diagnostic image for smaller sized organs such as the prostate gland, which may result in an adverse low diagnostic outcome [97].

The introduction of endo-rectal coil (ERC), which suggested a better images increase the diagnostic accuracy and performance. An ERC captures better and more detailed gland morphology of the prostate and adjacent tissues, and gives an opportunity to maximize the utilization of functional mpMRI sequences [96]. An ERC accompanied with 3 Tesla imaging systems are responsible for increasing the overall diagnostic accuracy to 97%, sensitivity and specificity 88% and 98% respectively [96, 98]. Special care must be taken with the use of ERC to avoid or minimize artifacts during imaging, such as caused by air in the rectal bulb. Additionally, patient discomfort can cause movement, which leads to malpositioning and motions artifacts.

Clinical MRI imaging is typically performed with two types of magnetic field strength fields, either 1.5 or 3 Teslas (1.5T or 3T). Both strengths have been recognized by radiologists, however, 3T MRI systems increase the signal to noise ratio (SNR) and spatial resolution, resulting in well developed image and more enhanced resolution quality [99].

MRI should be postponed for 6-8 weeks after a prostate biopsy to avoid any haemorrhage artifacts. Prostate haemorrhage is considered as one of the possible cancer confounders, mimicking cancer on MRI. The patients are instructed to abstain from any sexual activity for 72 hours before the scan to increase seminal vesicle volume and improve cancer detection. Patients are also advised to fast at least 4 hours and empty their bladder one hour before the MRI scan. Use of Scopolamine is sometimes required to reduce bowel movement, decreasing patient discomfort and minimizing artifacts [100].

MRI allows prostate gland assessment with higher spatial resolution and soft tissue contrast compared to any other imaging modalities. The three most relevant MRI sequences in our study were T2-weighted, DCE, and (DWI) **(Figure 1.14)**.

1.4.1 T2-Weighted Imaging (T2W)

T2W is the main squence used for prostate MR imaging. It is conducted with a Fast Spin Echo (FSE), also known as a Turbo spin echo (TSE) sequence with multiple spatial planes, enabling a better assessment of the gland volume than with other imaging modalities [95]. The T2W sequence creates an image with a detailed spatial resolution and soft tissue contrast, enabling full evaluation of the zonal anatomy and adjacent tissues, including the urethra, seminal vesicle, extracapsular extension, and neurovascular bundles [101]. The high-water tissue content is represented in the T2W image with a high signal intensity while fat is displayed with a low signal intensity. In the case of presence of prostate cancer, water content is diminished significantly leading to a low signal intensity in contrast to normal adjacent prostate tissue [102].

The multi-planer sequence includes the axial plane, which must be combined with sagittal and coronal planes. The image generated by the axial sequence typically includes the bladder dome superiorly until the perineal area inferiorly, and the coxo-femoral joint borders bilaterally. The sagittal plane enables the evaluation of the prostate gland posterior surface and its relation to the rectum and the bladder. The coronal plane, which is slightly oblique along with the main prostate axis,

allows for a better assessment of the transition and peripheral zone, and in particular the lateral and anterolateral horns [97].

The normal peripheral zone appears in the T2W sequence as hyperintense, particularly due to the presence of a significant amount of glandular and high-water content tissue with a clear crescent or horseshoe shape through the mid-gland section. The peripheral zone is surrounded by a prostate capsule, which appears as a thin, full hypointense layer, that circles the whole gland. The prostate capsule has a substantial clinical significance, as it is used as a landmark in staging PCa [101]. Cancer in the peripheral zone is characterized by an oval or nodular shape focus with low-signal intensity. The sensitivity in detecting PCa in T2W reaches more than 90% with Gleason score of 7 and higher, and decreases markedly with Gleason score lower than 6 [100].

The Central and Transition zones are hard to distinguish when there is no evidence of BPH presence. The differentiation of the central zone could reach 80% with current MRI systems [103].

The transition zone consists of less glandular tissue with low water content compared to the peripheral zone. The internal gland, which forms from the transitional and periurethral zone is categorized by intermediate signal intensity, which increases the challenge for detecting cancer in the transitional zone due to signal overlapping of tumours and BPH. The central gland is surrounded by a thin hypointense layer isolating it from the peripheral zone [100].

The transition zone in the presence of nodular hyperplasia shows heterogeneous signal intensity depending on the nodules' consistency. Two types of nodules can be found in the transition zone, glandular and stromal nodules. Glandular nodules represent the more common type. It appears as a homogeneous high signal intensity due to high fluid content with a thin layer of the hypointense capsule. The second type is a stromal nodule, which has a homogeneous low-signal intensity surrounded by a fine hypo-intense capsule. The stromal nodule is more relatively challenging to identify due to its distinct variation [96]. The malignant

tissue in TZ appears homogeneous with vague or blurred margins giving an erased charcoal sign, lenticular, or water drop shape [104].

Identifying PCa in the central zone with T2W imaging is quite challenging [105]. It appears as a collection of tissue separating the transition zone from the peripheral zone on an axial view with low-signal intensity compared to the outer region. The central zone tissue is commonly pushed laterally towards the peripheral zone by glandular hyperplasia of the transitional zone. The coronal view sequence illustrates the central zone as a triangle or tear-drop-shaped appearance ranging from seminal vesicle to verumontanum area [105].

The anterior fibromuscular stroma (AFMS) is the most anterior structure of the gland with a crescent or wedge-shaped appearance. It is characterized by homogenous, marked hypointense signal on T2W, which is best seen in an axial view sequence. Cancer involvement in AFMS is signified by a high signal intensity rounded in shape and external protrusions that affect gland symmetry and sometimes prostate capsule continuity in the case of external prostatic extension (EPE). Due to its heterogeneous appearance, a normal central zone tissue could mimic cancer on T2W and ADC imaging [96, 106].

The coronal view sequence gives excellent detail of the seminal vesicles, and has a variable signal intensity that relies on fluid volume. Aging has an adverse physiological effect on fluid volume inside the seminal vesicle leading to a decrease in signal intensity. Cancer involvement in the seminal vesicles is characterized by thickening of its wall, asymmetric shape appearance, focal or diffuse low signal intensity, and enlarged ejaculatory ducts [107-109].

The sagittal view provides an excellent imaging tool to assess the bladder neck, a full length of the prostatic urethra, seminal vesicle and its relationship to the rectum and Denonvilliers's fascia. This provides a practical tool for PCa staging. Cancer mimickers in T2W images include the central zone, stromal BPH, ejaculatory ducts, haemorrhage, and chronic prostatitis.

1.4.2 Diffusion-Weighted Image (DWI) and Apparent Diffusion Coefficient (ADC)

The diffusion-weighted image (DWI) sequence is based on Brownian motion of water molecules in tissues, which is affected by tissue temperature and by degree of cellularity [110]. The diffusion of fluid occurs from a high concentration zone to a lower concentration zone, and is controlled by tissue thermal energy and cellularity. The DWI sequence provides the ability to assess the micro-architecture of the imaged tissue [111]. The coefficient “b” is the determining factor of the diffusion sequence. The level of sensitivity of water molecules weighted diffusion is directly proportioned with “b”. The “b” coefficient is affected by the diffusion parameters, which include distance, intensity, and duration between two tissue gradients. Thus, DWI will be more sensitive to tissues with a higher diffusion coefficient [96, 101]

The quantitative assessment of the reconstructed DWI image is used to generate a visual map called the Apparent Diffusion Coefficient (ADC). The ADC map, expressed in units of mm^2/s, is calculated using the “b” coefficient, which represents the degree of water molecules diffusion in the targeted tissue [96]. The ADC map establishes an estimated average value of each voxel in the imaged region and is displayed as an opposite contrast to the captured DWI image. This process assists in eliminating the T2 shine-through effect as ADC measures the degree of diffusion independent from the T2 shine influence. [95, 112].

Water diffusion in healthy prostate tissue is captured as a low signal intensity due to low or regular cellularity due to free water diffusion. The image is depicted as a hyperintense value on ADC. In contrast, cancer tissue is associated with crowded small glands, and cells with a larger nucleus to cytoplasm ratio, a limited amount of stroma between glands, reduced extracellular space, and abnormal parenchymal tissue structure. These changes diminish water molecule diffusion in tissues, and result in a high signal intensity on DWI, which is converted to a hypointense value on an ADC image [95, 101]. DWI and ADC images in addition

to T2W could provide an extra quantitative assessment of prostate tumour behavior and aggressiveness [113].

1.4.3 Dynamic Contrast-Enhanced (DCE)

PCa is found to be associated with a new vascular formation with high vascular density and permeability in a process called neoangiogenesis. This blood supply provides the necessary nutrients to tumour cells [114]. DCE-MRI is a functional imaging method with the ability to assess the vascular supply and microvascular structure of the tissue in a given zone by capturing the tissue enhancement after intravenous administration of a contrast agent. The DCE imaging procedure takes approximately 5-10 minutes to complete. A fast T1W sequence is required to acquier multiple serial images within a short time interval before and after contrast injection. T1W images will establish a baseline evaluation of the tissue during contrast injections to distinguish the contrast influx to the prostate gland, and post-injection, to estimate the uptake and washout time of the contrast. These multiple scans provide images of the prostate tissue perfusion for assessment [115]. The DCE images are obtained with high temporal resolution and a 3D acquisition mode.

The DCE image is generated by injecting rapidly a contrast agent of low-molecular-weight gadolinium chelate at a rate of 2-4mL/S followed by a saline flush [101]. The contrast agent molecules will diffuse into the extracellular extravascular space (interstitial space), termed as the leakage space. Abnormal neovascularization and reconstruction, which accompany the prostate tumour, will have a stronger vascular leakage, resulting in the prostate tumour having a quicker, more intense contrast enhancement compares to the normal adjacent tissues followed by rapid washout before surrounding tissue [96].

There are three methods available for assessing DCE images, qualitative, semi-quantitative and quantitative. The qualitative assessment approach is based on the visual analysis of the potential cancer area with observation of the rapid regional significant enhancement and early washout of the contrast agent compared to the adjacent tissue. This method is subject to inter-observer experience and variability

with the least standardization capability. BPH, transitional zone, and inflammation could be responsible for relatively high enhanced image on DCE sequence and quicker washout compared to the rest of the gland tissue, but not to the same extent as PCa [102, 116].

The semi-quantitative approach utilizes the time and intensity curve in addition to the same principle used in qualitative assessment including the time for enhancement and washout. The time/intensity curve estimates the time to obtain maximum peak enhancement, the slope of the curve, wash-in or wash-out times. Three types of time/signal intensity curves are commonly generated with a software aid. The persistent type 1 curve shows a clear evidence of the constant progress of enhancement after the initial peak. Type 2 curve, which is named a plateau, shows a curve that flattens after the initial peak. Type 3 curve is named the decline, and is characterized by rapid decline of the curve after the initial peak [117, 118]. Prostate tumours are more likely to be associated with a type 3 curve, but can produce type 1 and type 2 curves to a lesser extent [119].

Quantitative DCE image assessment utilizes multifaceted methods including pharmacokinetic parameters such as the volume transfer constant (K^{trans}), which evaluates the contrast agent influx from blood vessels and capillaries into the interstitial space, which is extracelluler and extravaculer. (K^{trans}) is influenced by blood flow, vascular permeability and surface area [120]. The reverse reflux rate of contrast agent from the interstitial space back to the vascular stream is (K_{ep}), and (V_e) represents the extracellular, extravascular volume fraction and are related thus: K_{ep}= K^{trans}/V_e [117]. Many software applications have been developed to generate more accurate and quantitative DCE map parameters to be used in developing more standardized assessment guidelines in the evaluation of PCa from DCE images. Prostate cancer will produce an increase in K^{trans} and K_{ep}. The current method of choice is the quantitative assessment of DCE images, despite its high complexity compared to semiquantitive assessment [117].

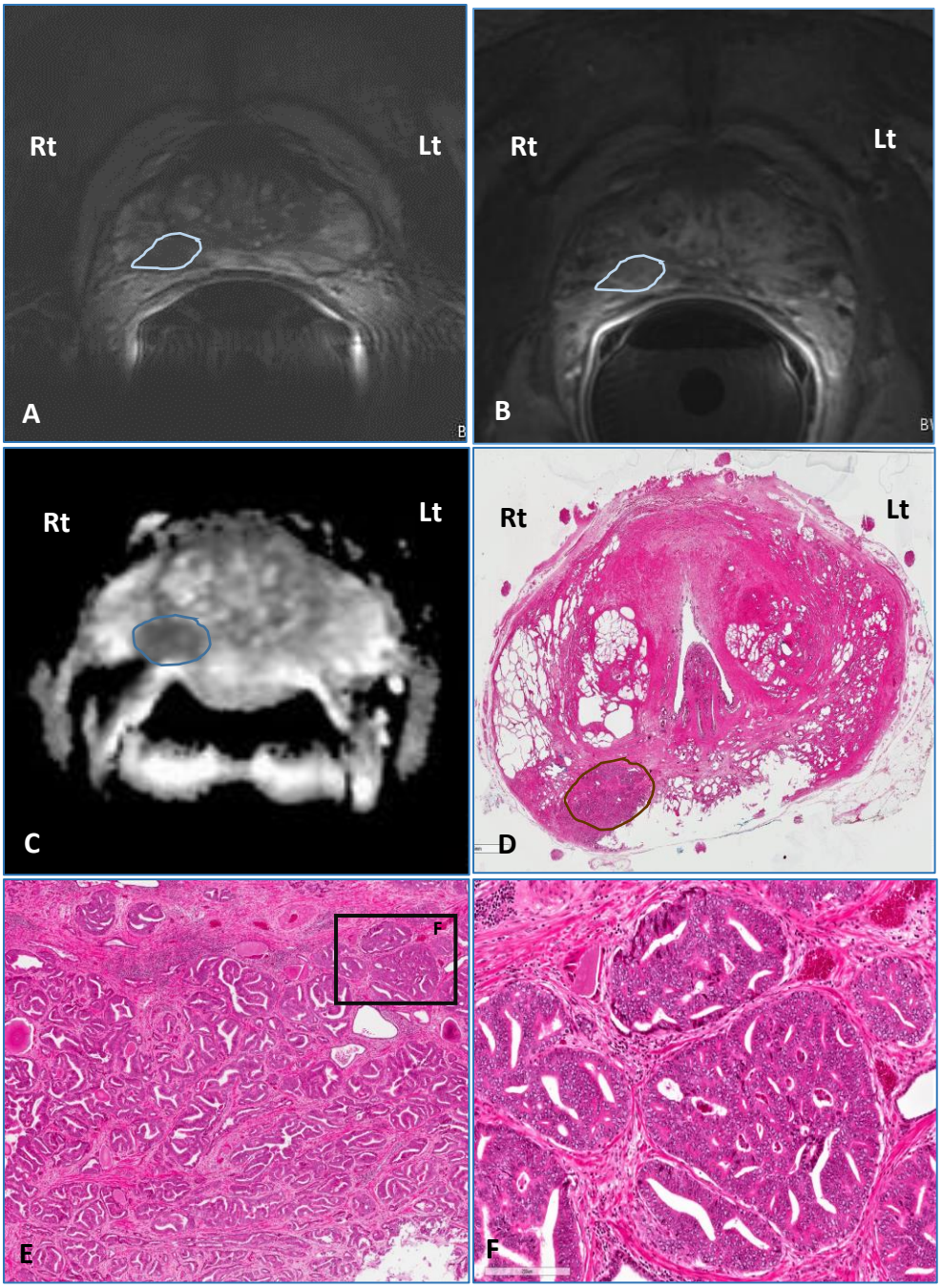

(Figure 1.14) In-vivo prostate multiparametric MRI and its corresponding histopathology digital image. (A) Axial T2W image with an area of hypointensity on the right posterolateral aspect of prostate gland (light blue) contour. (B) Dynamic contrast-enhanced image. (C) ADC map with hypointensity in the same region. (D) Histopathology digital image for the whole-mount prostate section with adenocarcinoma features in same region (brown) contour.

(E) 10X image of the affected area showing Gleason grade 4 (G4) adenocarcinoma. (F) High power view for the affected area (rectangular) with a G4 cribriform pattern.

1.5 Prostate Imaging Report and Data System (PI-RADS)

The emergence of MRI as a useful tool in detecting and localizing prostate cancer was accompanied by an initial lack of standardization in interpreting of this imaging data between radiologists with similar earlier challenges faced with breast mammogram. Thus, there was an urgent need to develop an assessment approach to be widely adopted by experts to improve the quality of reporting, create a better standardization and reduce inter-observer variability.

Multiple assessment methods have been introduced to evaluate prostate mpMRI. One of the preliminary methods was assessing the suspected lesion on a binary scale whether it is positive or negative for malignancy [121]. Based on the number of sequences marked as positive, the suspected lesions were asigned a score of low, intermediate and high. Despite the simplicity, this approach was not popular due to the inability of addressing the variability of degree of abnormality observed in the MR image sequences [122].

Recently, the Prostate Image Report and Data System (PI-RADS) has gained international popularity since it was introduced by the European Society of Urogenital Radiology, followed by publishing a guideline in 2012 [123]. They aimed to develop a clinical guideline that focuses on the three optimal diagnostic technique for detecting, staging, node and bone involvement.

To assess prostate mpMRI images using a PI-RADS score, prostate images should be acquired using a high-field scanner with 1.5 Tesla (1.5T) as a minimum field strength accompanied by endo-rectal and body phase array coils to yield a high signal to noise ratio. An endo-rectal coil could be optional with field strength of 3 Tesla [124].

The T2W image using turbo-spin-echo (TSE) is the main method for prostate MR imaging as it provides a highly detailed image of the prostate anatomy and surrounding tissues with visually recognizable zonal morphology. T2W images are acquired with axial, sagittal and/or coronal sequences [124], and a T1W image is also highly suggested to rule out any intraprostatic haemorrhage from a prior

biopsy or inflammatory reactions. The T1W image could also be helpful in assessing parailiac and regional lymph nodes enlargement, suggesting a metastatic disease [124].

The PI-RADS classification of T2W is based on zonal anatomy. Two separate schemes are endorsed for different zonal anatomy as the contrast varies between peripheral zone and central gland **(Table 1.2-1.3)**. Also, any involvement of the bladder neck, seminal vesicles invasion or extra-prostatic extension must be noted [125, 126].

The PI-RADS interpretation of DWI is based on images acquried with a high b-value ($b \geq 800 s/mm^2$) with corresponding apparent diffusion coefficient map. Each lesion is assessed with a score 1-5 according to signal intensity and localization [127].

Any increased signal in DWI aquired with a high b-value not accompanied by a focally reduced the signal in the ADC maps is assigned a Score of 1. Diffuse hyperintense signals on DWI with a reduced signal on a corresponding ADC map is assigned a score of 2 (lesion cannot be delineated). Score 3 is assigned to a diffuse asymmetrical or unilateral high intense signal on the high-b-value image, which is accompanied by a decreased signal on a corresponding ADC image. Focal lesions that are isointense on DWI with a high b-value and a signal reduction on a corresponding ADC map are assigned a score of 4. The focal significant reduction on an ADC map with a focal hyperintense signal in a corresponding DWI image with a high b-value ($b \geq 800 s/mm^2$) is assigned a score of 5 **(Table 1.4)** [123, 124].

The PI-RADS is used to assess each mpMRI image individually with a score range from 1 to 5. The assessment followed by an overall score varies from 1 to 5. Each area and suspected lesion in an image generated by the different sequences should be evaluated separately with a scoring between 1 and 5. The total overall rating is then calculated based on a number of lesions, locations and each lesion score with the possibility of the presence of extraprostatic extensions. An overall score ranging between 1 and 5 characterizes the probability of the presence of a

clinically significant tumour. Transitional zone assessment must be performed separately from the peripheral zone [122, 123]. The PI-RADS assessment must include the seminal vesicles, prostate capsular involvement or any sign of potential or compact evidence of extraprostatic extension [123].

Score	Criteria
1	Uniform high signal intensity (SI)
2	Linear, wedge shaped or geographic areas of lower SI, not well demarcated
3	Intermediate appearances not in categories 1-2 and 4-5
4	Discrete, homogeneous low signal focus/mass confined to the prostate
5	Discrete, homogeneous, low SI focus with EPE, invasive behaviour or mass effect on capsule (e.g. bulging)

(Table 1.2) PI-RADS scoring system classification criteria for T2W image assessment for the peripheral zone [123]

Score	Criteria
1	Heterogeneous TZ adenoma with well defined margins (organised chaos)
2	Areas of more homogeneous low SI, well defined margin, originate from TZ/BPH
3	Intermediate appearances not in categories 1-2 and 4-5
4	Areas of more homogeneous low SI, ill defined (erased charcoal)
5	Same as 4, involving the AFS or anterior horn of PZ, lenticular or water drop shaped

(Table 1.3) PI-RADS scoring system classification criteria for T2W image assessment for the Transition zone [123]

Score	Criteria
1	No reduction in ADC compared with normal glandular tissue. No increase in SI or any high b-value image (≥b800)
2	Diffuse, hyper SI on ≥b800 image with low ADC. No focality however, linear, triangular or geographical features are acceptable
3	Intermediate appearances not in categories 1-2 and 4-5
4	Focal area(s) of reduced ADC but iso-intense SI on high b-value images (≥b800)
5	Focal area/mass of hyper SI high b-value images (≥b800) with reduced ADC

(Table 1.4) PI-RADS scoring system classification criteria for Diffusion Weighted Imaging (DWI) image assessment [123]

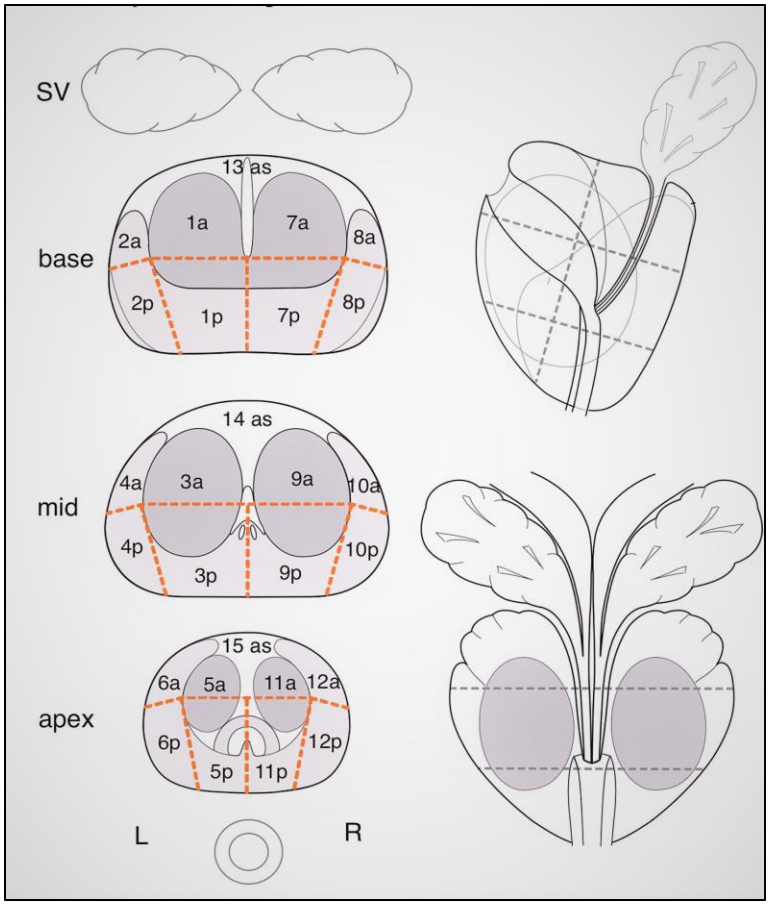

(**Figure 1.15**) **Twenty-seven regions of interest for the standardized PI-RADs scheme** [128], a: anterior, as: anterior stroma, p: posterior, R: right, L: left. SV: seminal vesicles.

PI-RADS Score	Interpretation
1	Benign, highly unlikely for malignancy
2	Most probably benign or unlikely for malignancy
3	Intermediate or equivocally
4	Likely or probably malignant
5	Highly suspicious of malignant

(Table 1.5) Interpretation of PI-RADS scoring assessment [124, 128]

1.6 Rationale

Our study aims to gain a better understanding of non-cancerous pathological lesions in prostate gland and their relationship to mpMRI signal that could be mistaken as a potential cancer signal on MRI.

This may help increase cancer detection accuracy and reduced false positive detection of prostate cancer.

1.7 Hypothesis

Atrophy, PIN, and BPH are the main non-cancerous pathology that could mimic cancer like signals on mpMR images due to their morphological similarity with adenocarcinoma.

1.8 Specific Aim

The objective of the study is to test and examine non-cancerous pathology lesions and their subtypes that could raise a false positive cancer like signals on mpMRI.

Chapter 2

2 Materials and Methods

This study was approved by the Human Subject Research Ethics Board London Health Sciences Center, (LHSC), and University of Western Ontario, London, Canada). A written informed consent was obtained from each patient before a non-clinical standard set of *in vivo* prostate gland scan. Images were taken two to three weeks in advance of surgery.

2.1 Materials

A total of 19 patient were enrolled in the study. Patients who participate in the study have been previously diagnosed with prostate cancer through prostate biopsy. Prior to prostatectomy, a multi-modality set of images including an *in vivo* multiparametric Magnetic Resonance images (mpMRI) were acquired from each participant using a 3 Tesla MRI scanner (GE Discovery MR750, GE Healthcare, Waukesha, WI) [129] with the use of an endorectal coil (Prostate eCoil; Medrad, Warrendale, PA) surrounded by barium sulfate suspension in a sheath [129]. The mpMRI included high-resolution T2W images for diagnostic assessment, also to allow registration to other modalities, Dynamic Contrast Enhanced (DCE) and Apparent Diffusion Coefficient (ADC) images [130]. The *in vivo* mpMRI images were obtained after the biopsy and before surgery. The mpMR Imaging was performed 19 weeks (± 8 weeks) following the biopsy. This period was to allow the prostate gland a recovery period to avoid haemorrhage interference with the analysis of the images.

A strict patient inclusion and exclusion criteria allowed for the collections of the radical prostatectomy specimens from 19 cases. Patient inclusion criteria were as follows: the patient must be at least eighteen years of age and have a confirmed clinical diagnosis of PCa histologically, clinical classifications of the tumour grade between T1 and T2 by trans-rectal ultrasound (TRUS) guided biopsy, and radical prostatectomy as the choice of treatment. Patient Exclusion criteria were: any use of 5-alpha reductase inhibitors in the past 6 months prior to study

enrolment, any prior therapy for PCa, any contraindications to perform and acquire the preoperative set of MR imaging with contrast as renal functions impairments, sickle cell disease or any other type of anemia, and allergy to the contrast agents or any source of artifact in the pelvis (e.g. hip prosthesis).

The T2W imaging was performed with a two-dimensional (2D) and three-dimensional (3D) fast spin-echo sequence (repetition time msec/echo time msec,6050/163; bandwidth, ±31.25 kHz; two signals acquired; field of view, 14 cm; section thickness 2.2 mm; matrix -384 × 256; 40 slices) and (2000/148.5; bandwidth, ± 125 kHz; one signal acquired; field of view, 14cm; slice thickness, 1.4 mm; matrix, 320 × 192; 84 slices) for 2D and 3D T2W respectively. The T1 weighted images were acquired with the 3D spoiled gradient-recalled echo (5.6/2.1; bandwidth, ±31.25 kHz; two signals acquired; field of view, 14 cm; section thickness, 2.8mm; matrix, 256 ×192; 42 sections; flip angle, 15°;7 volumes acquired at 90 sec/volume) [130]. The T1W imaging was performed after administration of gadopentetate dimeglimine (Magnevist; Bayer Healthcare Pharmaceutical, West Haven, Conn) intravenously [130]. The dose of gadopentetate dimeglimine was 0.1 mmol per kilogram body weight with injection rate of 4 ml/sec followed by 20ml of saline flush. The radical prostatectomy followed *in vivo* imaging. The resected prostate specimens were fixed in formalin for 72 hours before fiducial insertion, *ex vivo* MR imaging, and histopathology processing (**Figure 2.1**).

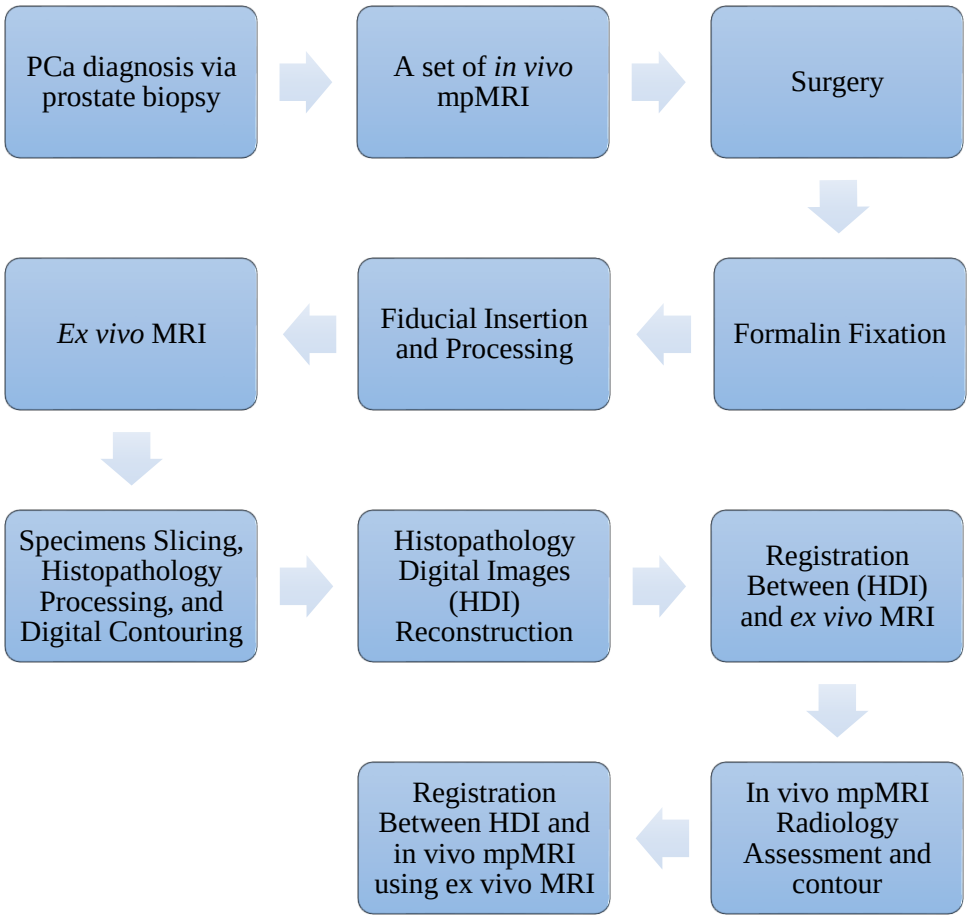

(**Figure 2.1**) **Overview of the steps in our method used in prostate specimen processing.**

2.2 Methods

2.2.1 Fiducials Processing

Before obtaining *ex vivo* prostate MR images, two sets of 10 standard shape fiducials markings were applied to the prostate gland. The aim of this non-anatomical markings was for them to be visible in the *ex vivo* MR and digital histology images. The fiducials were required to be able to endure the heat and the tough chemical treatment through gland grossing and histology processing without any distortions or damage to the tissue. In contrast, these fiducials should not have any impact on pathologists' assessment. This was ensured as any alteration to pathology assessment will have a significant impact on post-surgery patient care and management.

The internal fiducial markers consisted of three cotton threads soaked in blue dye designed for tissue marking (Triangle Biomedical Sciences, Durham, NC) and 1:40 gadopentetate dimeglumine, which enabled visibility and identifications of the fiducials on T1 weighted MRI [131]. The internal fiducials applications were completed with the assistance of 18G cannula and stylet with a Quincke-type point (**Figure 2.2**). The cannula with a stylet was designed to perform a clear tissue separation to avoid any tissue damage during the insertion processes. The cannula and stylet were inserted into the prostate gland from the base and exit at the apex with an optimal target to be within one centimeter posteriorly to the anterior urethral opening. Strict measurements were applied with caution to keep the cannulas at a fair distance from the urethral structural and openings to avoid any clinical assessment alteration or aggressive treatment methods for follow up management due to possible higher tumour staging diagnosis. Following the insertion of total three 18G cannulas and style, two on the right prostate lobe and one on the left lobe, the stylets were then removed, and a fair length cotton thread was inserted through each cannula. The free part of threads were soaked in blue dye and gadolinium. Following the cotton thread insertion with the blue dye, the cannula and cotton thread were pulled together outside the prostate tissue leaving the free soaked thread part with the blue dye and Magnevist within the prostate

tissue (**Figure 2.3**). The applied dye tissue marking enabled localization during digital histopathology analysis, and the gadolinium allowed localization in the *ex vivo* MRI. The cotton threads were removed after whole gland MR imaging and before specimen slicing to avoid any tissue disruptions during specimen slicing [132].

Cylinder-shaped surface-mount fiducials were extracted from a formalin fixed lamb or pig kidney cortex via 16G biopsy needle (the same model used in a breast biopsy) **(Figure 2.4)**. After successful extraction, they were completely immersed in 1:40 gadopentetate dimeglumine and 10% buffer formalin for a minimum of at least 20 minutes to ensure the completion of infusions. The fiducials were firmly fixed to the prostate surface using 411 Loctite ethyl cyanoacrylate adhesives (Loctite 411; Henkel, Dusseldorf, Germany) **(Figure 2.5)**. Loctite 411 does not interfere or generate any tissue damage during the cutting processes. Furthermore, Loctite 411 is sufficiently tough enough to survive the heat and chemicals through histology processing, preventing the external fiducial from deteriorating or disruption during the rough processing methods. The following step includes three fiducials applied on the posterior surface with one fiducial on each side with a 45° angle, and the remaining fiducial was applied centrally. On the anterior surface, three parallel fiducials were attached with two on the left side and one on the right. A fourth fiducial was placed diagonally from the right anterior to left posterior apex to base. Thus, a total of seven fiducials were mounted on the surface of the prostate [130-133].

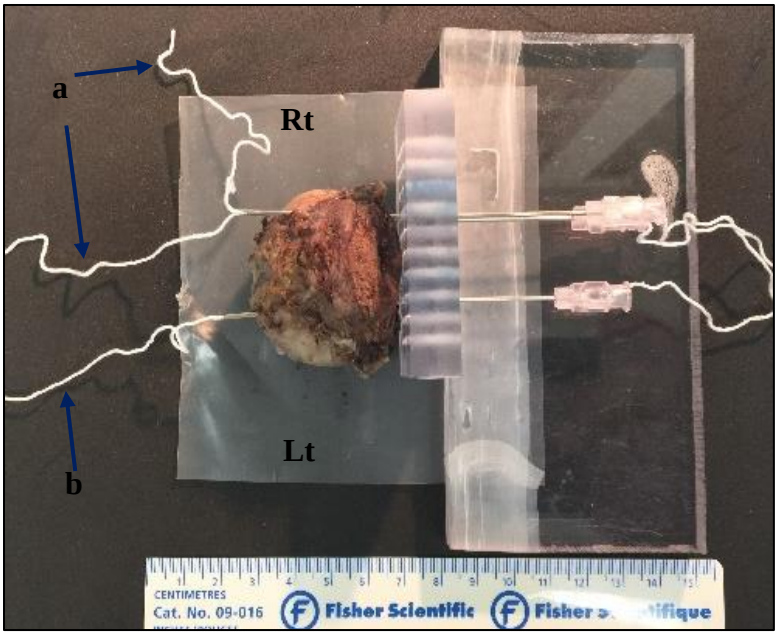

(Figure 2.2) Prostate gland with three 18G cannulas with inserted threads after removing the style. (Rt) right side, (Lt) left side (a) 2 threads on the right side and (b) 1 on the left side of the prostate gland.

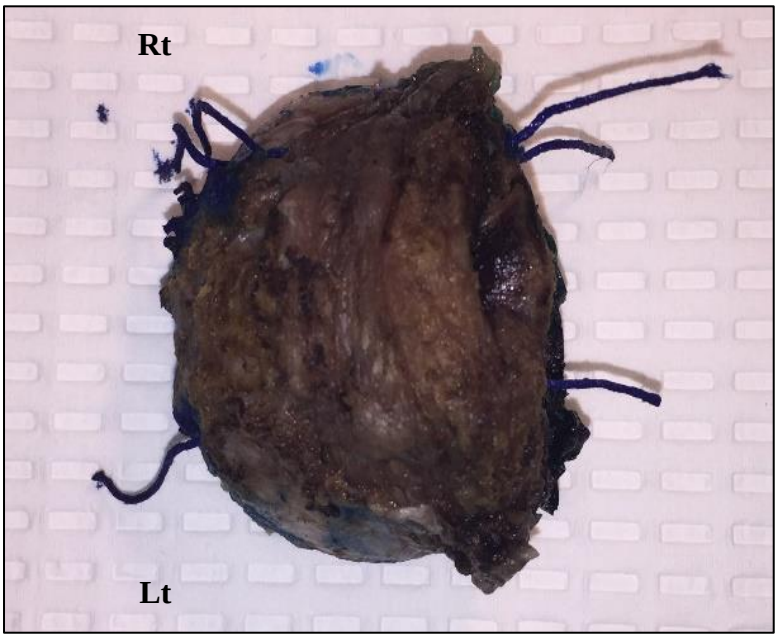

(Figure 2.3) Prostate gland after threads soaking in Magnevist & dye, followed by removing 18G cannula leaving threads inside the glands.

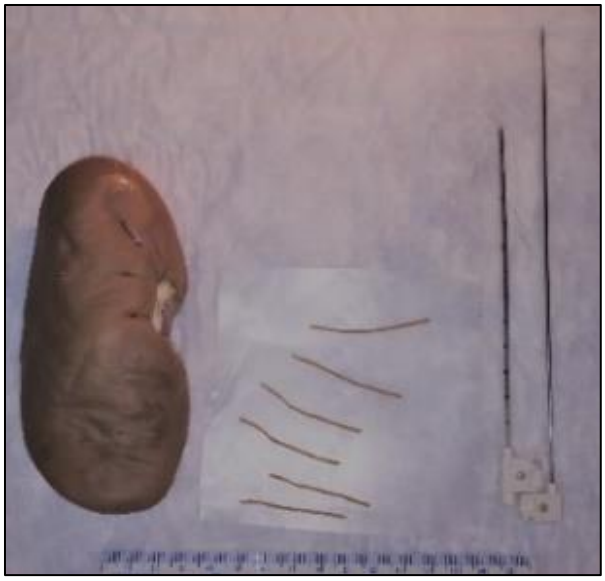

(Figure 2.4) The external fiducials obtained from a pig kidney by using breast biopsy needle

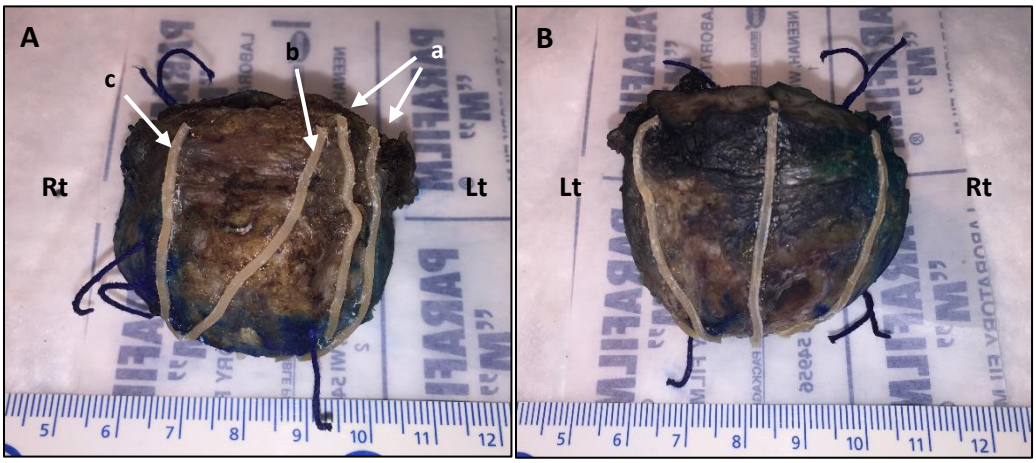

(Figure 2.5) The anterior and posterior surface of prostate gland post-fiducials application. (A) The anterior surface of prostate gland post fiducials application (pig Kidney) using 411 Loctite ethyl cyanoacrylate adhesives. Total of 4 fiducials, (a) 2 fiducials on the left side, (b) 1 placed diagonally, and (c) 1 on the right side. **(B)** Prostate gland posterior surface with a total of three fiducials (pig kidney) applied using 411 Loctite ethyl cyanoacrylate adhesives.

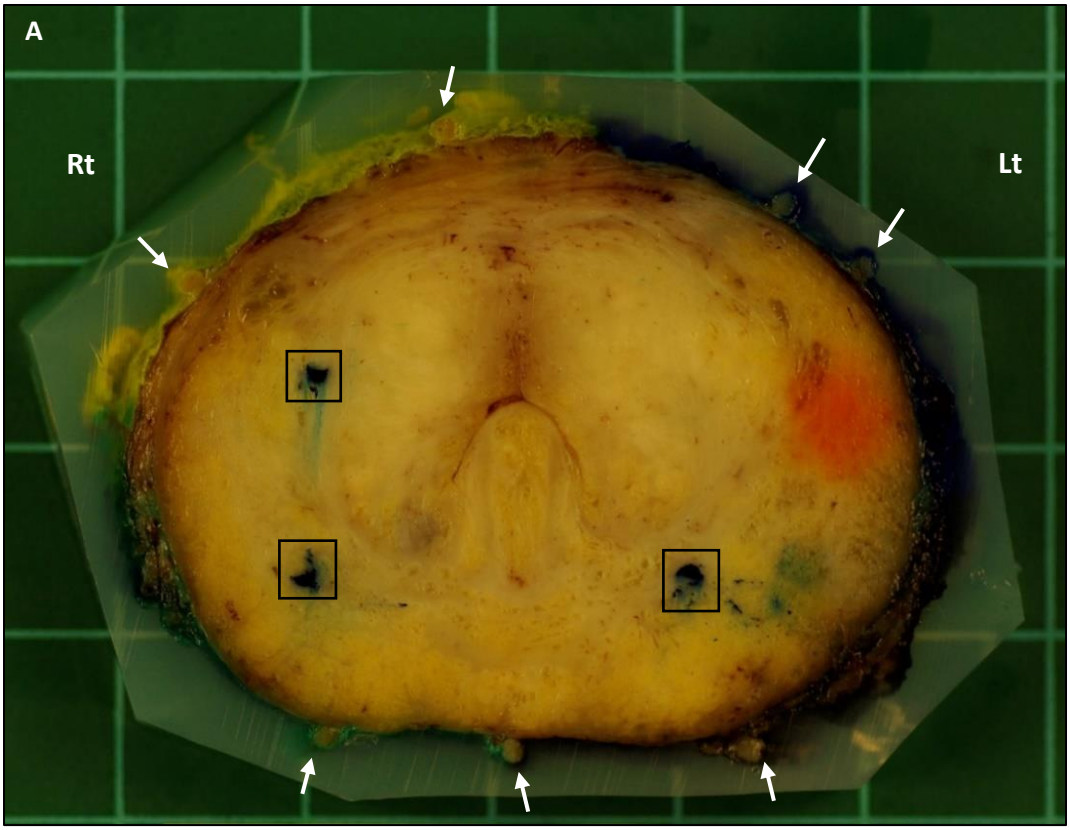
A
Rt
Lt

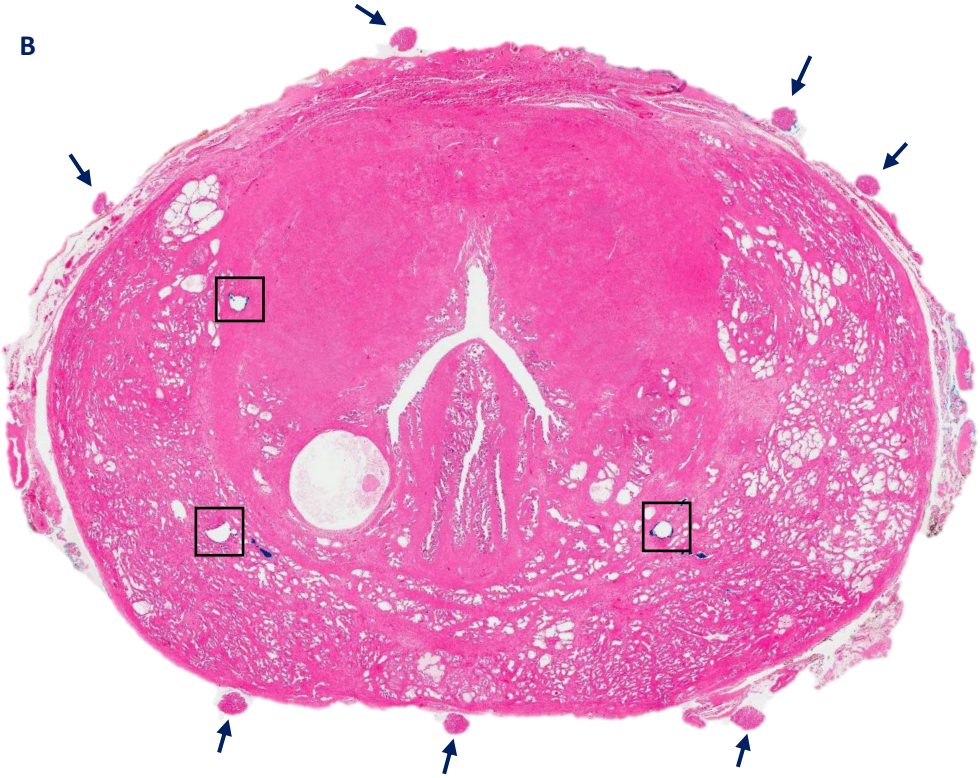
B

(Figure 2.6) Internal and external fiducial marking in formalin block and histopathology image. (A) Image of whole-mount prostate formalin blocks surrounded by the remnant of agar after prostate gland slicing and its corresponding (H&E) digital histopathology image (B). A total of 10 fiducial markings are clearly visible; 3 internal (black squares) with 2 on the right side and one on the left. A total of 7 surface mount fiducials (white arrows on formalin block and deep blue arrows on digital histopathology image), 4 on the anterior surface and 3 on the posterior.

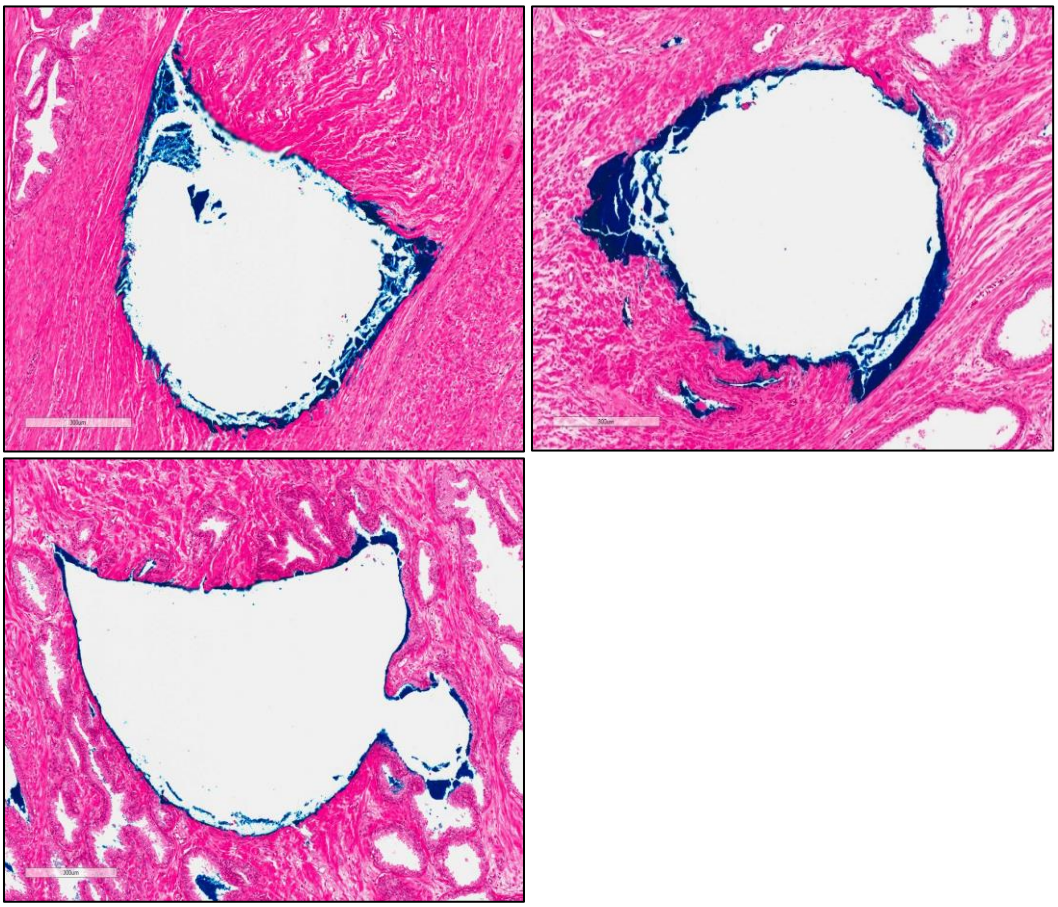

(Figure 2.7) High power digital histopathology images showing 3 visible inked internal fiducials marking (3 black squares on Fig: 2.6, B) with deep blue ink in 3 internal fiducial markings which were used as landmarks for prostate image reconstruction and registrations.

2.2.2 Ex-vivo MR Imaging

The *ex vivo* MR imaging was performed following the placement of fiducials marking. The whole gland was placed and fixed inside in a large glass syringe to prevent any movement during the MR scan. The glass syringe was filled with Christo-Lube MCG 1046 (Lubrication Technology, Franklin Furnace, OH). The Christo-lube is invisible in MR images, which gives zero signals to the surrounding regions of the gland. This provides a black background in the image and minimizes magnetic boundary artifacts at the prostate gland border. The MR images were acquired by an MR750 system (GE Healthcare, Waukesha, WI), using a carotid coil instead on endorectal coil in *in-vivo* MRI scan, T2W (3D fast spin echo; TR/TE:2000/148.5ms; bandwidth, ±125kHz; three signals acquired; field of view, 14 cm; slice thickness, 0.4mm; matrix 320×192; 160 sections; 25 minutes), and T1 weighted signal (3D spoiled gradient-recalled echo; TR/TE: 6.5/2.5ms; bandwidth, ±31.25 KHz; eight signals acquired; field of view, 14 cm; section thickness, 0.4 cm; matrix 256×192; slice; flip angle, 15°; 25 minutes) protocols [129, 132].

2.2.3 Specimens Slicing, Histopathology Processing, and Digital Contouring

This process was initiated after the removal of the prostate apex. The aim is to remove the prostate apex including the entire anterior urethral opening with at least 1 cm in thickness. The pathologist determined the plain of the first cut by visual assessment. Three pins were inserted, which were used for surface orientations during surface cuts using slotted forceps (ProCut; Milestone Srl, Sorisole, Italy) with design adjustments to avoid any lateral motions between the upper and lower forceps plates during cutting processing [131, 132].

Following the apex cut, the specimen was positioned in a square box with the cut surface facing the bottom of the box. The box was filled with liquid agar and cooled to 4°C. The whole block was sliced with a rotator blade cutter (GC-9 Slicer) measuring 4.4 mm thickness from the anterior cut aspect (Globe Food

Equipment, Dayton, Ohio) [131]. This thickness enabled simple registrations with MRI images since they were obtained with a 2.2 mm image slice thickness. The 4.4 mm histological thickness also resisted fragmentation or tissue rolling during handling and histology possessing. An average of three to five whole-mount sections per specimen were completed depending on prostate volume and shape.

The clinical histopathology processing protocols followed the base cutting, which included whole mount paraffin block, microtome cutting at 4 µm thick sections from each whole-mount block and staining with hematoxylin and eosin stain. The slides were then digitally magnified at 20X (0.5µm/pixel) using the brightfield slide scanner (ScanScope GL; Aperio Technology, Vista, CA, USA). Digital histopathology images were contoured with a color-coded scheme to identify various types of Gleason grades and scores as well as other non-cancerous abnormalities such as PIN and Atrophy **(Table 3.1)**. The contouring was completed with the use of Cintiq 22-inch HD widescreen computer monitor, which included an enabling pen for fine drawing (Wacom Co, Japan) and image scope software (Aperio Technology, Vista, CA, USA) **(Fig 2.8)**. The image contouring process was done under the supervision of two genitourinary pathologists, which their approval is required before submission to allow for the next step of registrations to be completed.

	G3		G4+3		PIN
	G4		G4+5		EPE
	G5		G5+4		Positive Margin
	G3+4		G5+3		Atrophy

(Table 2.1) The color coding scheme used for contouring cancer and non-cancerous lesions on digital histopathology images. (G3) Gleason grade 3, (G4) Gleason grade 4, (G5) Gleason grade 5. For the areas, which included more than Gleason grade with difficulty to contour separately. Thus, we combined the two or more grades together, with respect to dominant grade to be called first. For example, the G3+4 contour present area of two great complexes enough to separate them, with the G3 is the dominant grade in this area. PIN: Prostatic Intraepithelial Neoplasia, EPE: Extra-Prostatic Extension.

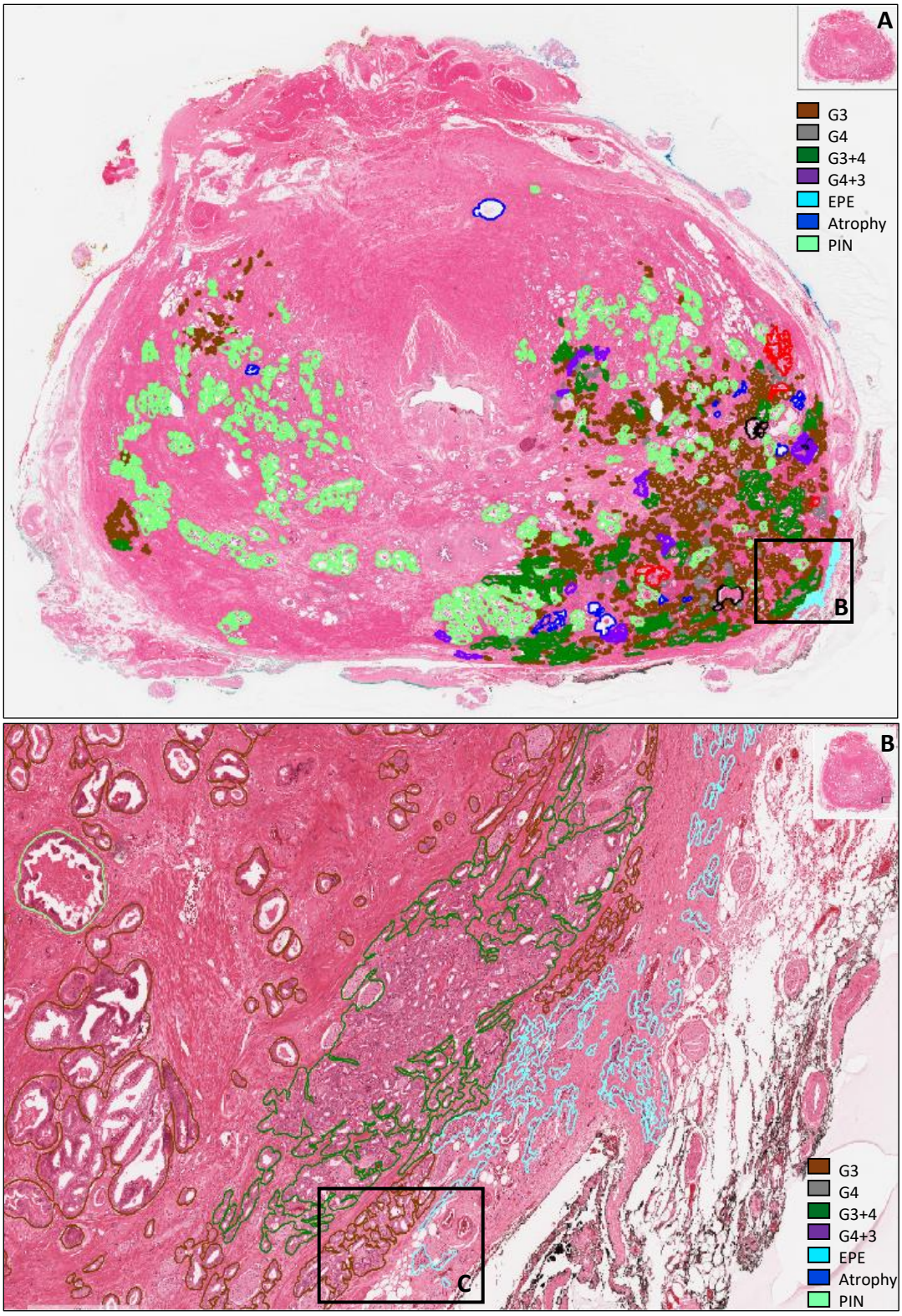
A
G3
G4
G3+4
G4+3
EPE
Atrophy
PIN
B
B
G3
G4
G3+4
G4+3
EPE
Atrophy
PIN
C

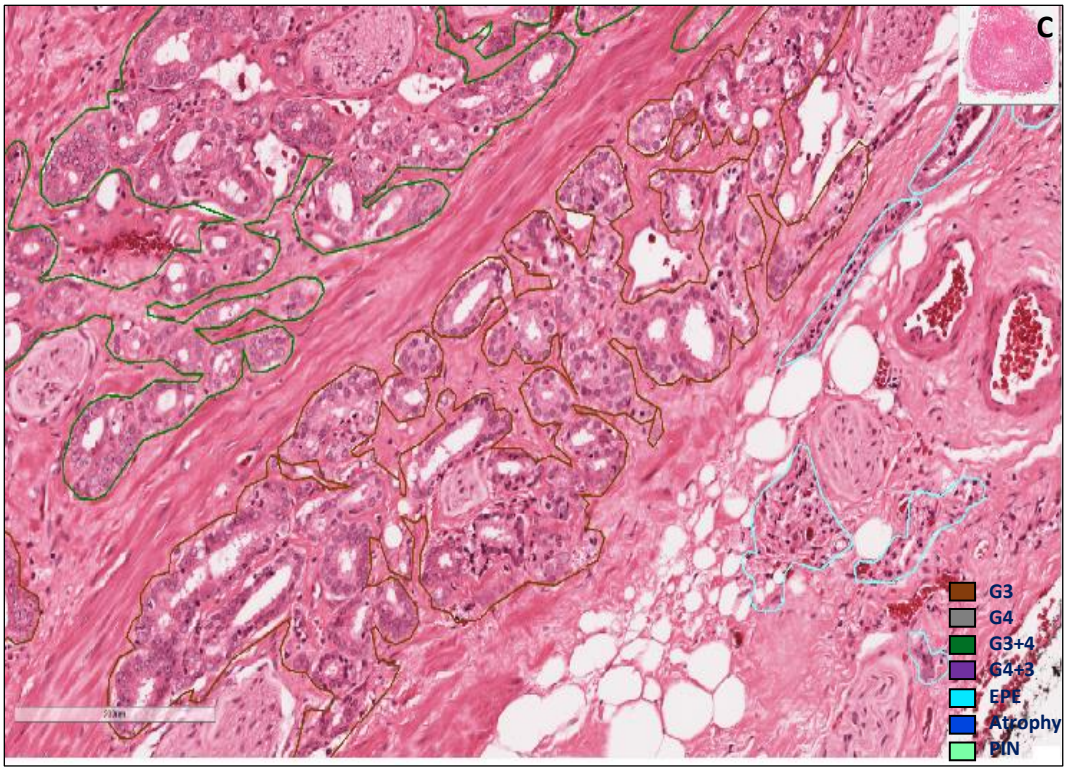

(Figure 2.8) Histopathology digital images for a whole-mount prostate section showing several contours with there color-coded scheme. (A) Prostate whole-mount histopathology image with color-coded contours for various types of cancer grade and non-cancerous abnormality. (B) 10X power zoom showing section with area contoured with (G3) Brown-Gleason grade 3, (G3+4) Green-Gleason grade 3+4, (EPE) cyan-Extra-Prostatic Extension. (C) reveals a high-power zoom 20X with G3, G3+4, and EPE.

Before full registrations, the *in vivo* mpMR images were assessed and contoured independently by four radiology observers. These observers had various levels and years of experience in prostate cancer assessment and diagnosis with mpMR imaging. The years of experience varied from five and six years with observer A and B respectively, to two and half years with observer C and D. These observers were aware that all patients had a biopsy confirmed PCa. However, they had no previous exposure to the histopathology diagnosis reports or evaluation for each individual case. They contoured unregistered T2W, DCE, and ADC MR images sequences separately using Version 1 of the Prostate Imaging Reporting Data System (PI-RADS) score system. The observers delineate lesions with a score from three to five: equivocally (3), likely (4) and very likely (5) to be a malignant tumour area. In this study, we only considered the same areas outlined by the radiology observers in the three-consecutive unregistered sequence of mpMRI, T2W, DCE and ADC. The PI-RADS score used in this study is the overall assessment score for each lesion in the three-previous consecutive sequence of mpMRI.

2.2.4 Registration

Initial registration was performed using the 3D Slicer viewing software between digital histopathology images and 3D *ex vivo* MR images with the aid of applied fiducials markings [132]. An interactive digital technique was developed in our lab for deformable registration of 3D *ex vivo* MRI and *in vivo* mpMRI to high resolution 3D *in vivo* T2W MR images with histopathology [133, 134]. Using a rigid method of registration and the anatomical homolog landmarks (e.g., Urethra, Verumontanum, cystic atrophy spaces, benign prostatic hyperplasia, calcifications) the registration error was $\leq$ 2 mm on average. This interactive digital technique allowed navigating simultaneously between the mpMRI sequences (T2W, DCE, and ADC) and the contoured histopathology. To avoid any confusion or registration errors, we excluded any false positive MRI contours adjacent to PCa region on the histopathology digital images.

Chapter 3

3 Results

3.1 Analysis of MRI Contoured Areas

(**Figures 3.1-3.4**) show examples of contoured mpMRI images by the four radiology observers and the corresponding histopathology images. These four figures illustrate four different patient cases of the 19 cases analyzed in this study.

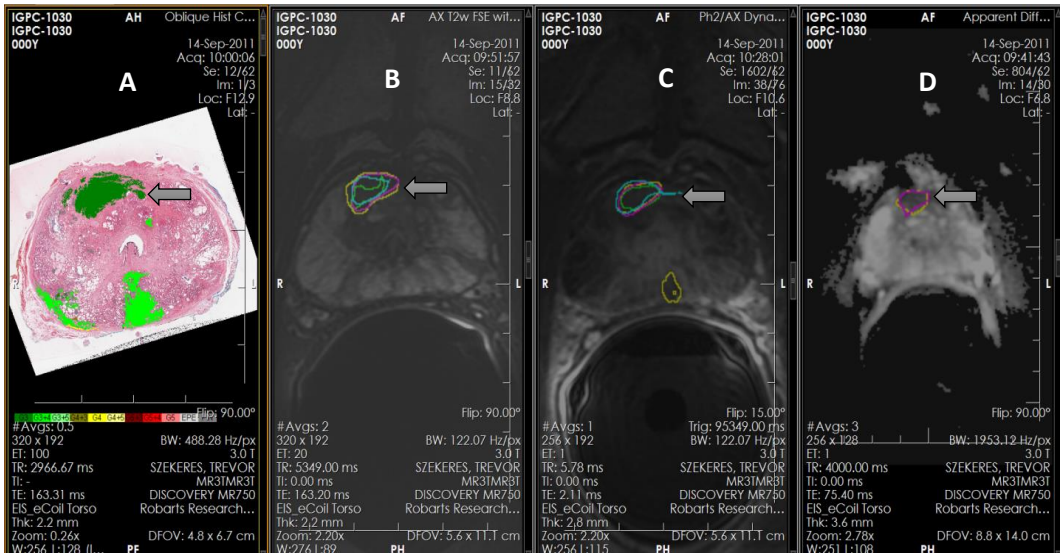

(Figure 3.1) True Positive mpMRI contour correlated to Gleason grade 3 adenocarcinoma on histopathology image. (A) Histopathology image showing a contoured area (gray arrow) for Gleason grade 3. (B) True positive areas on T2W MRI image contoured by the 4 observers, (C) contoured on DCE MRI image, and (D) contoured on ADC map and their corresponding area on histology with Gleason grade 3, and Gleason scores 6.

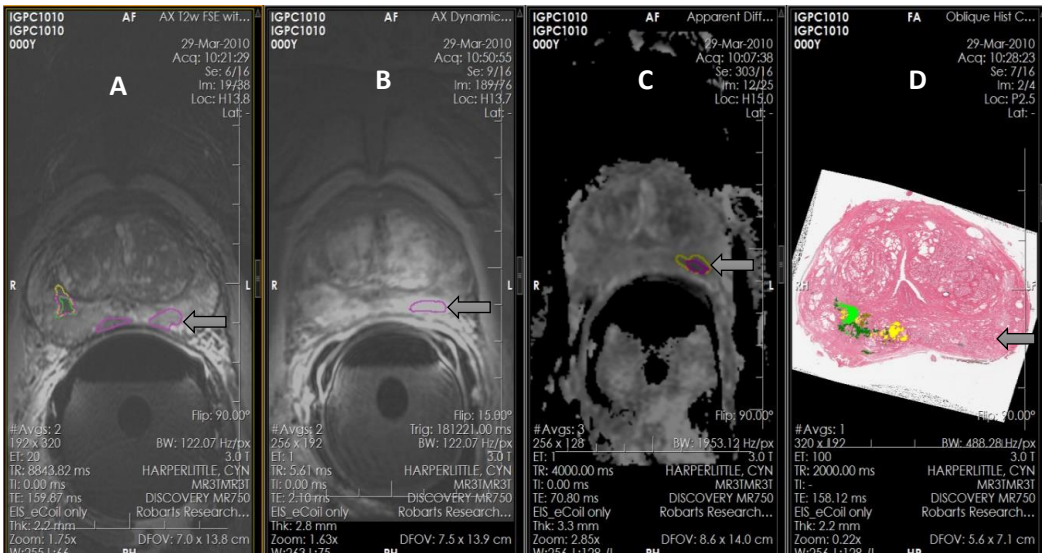

(Figure 3.2) False Positive mpMRI contour correlated to the area with atrophic glands. (A) A false positive area on T2W MRI image contoured by one observer (gray arrows). (B) Contoured on DCE MRI image, and (C) contoured on ADC map. The corresponding area on histology shows atrophic glands change on Histopathology image (D).

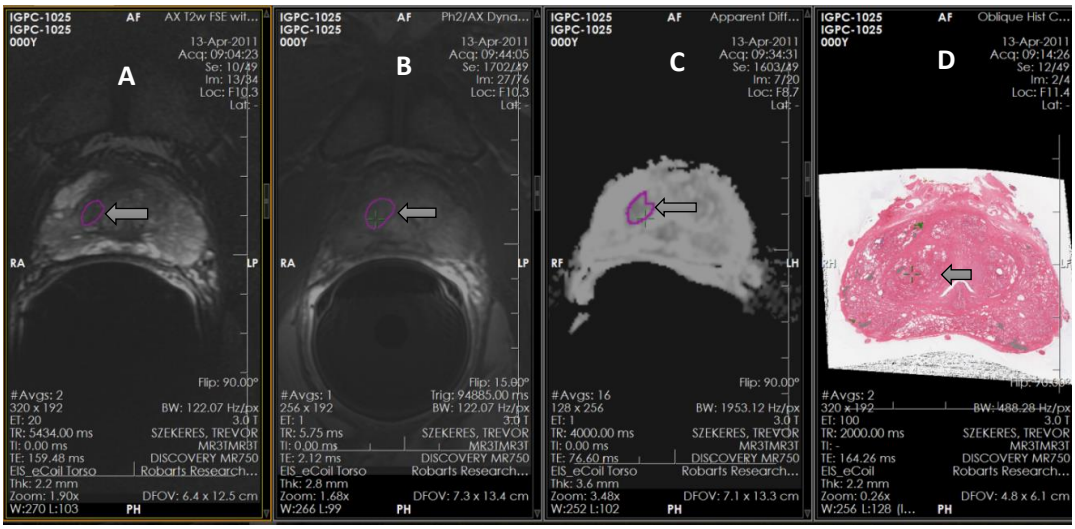

(Figure 3.3) False Positive mpMRI contour correlated to the area with BPH. (A) A false positive area on T2W MRI image contoured by one observer (gray arrows). (B) Contoured on DCE MRI image, and (C) contoured on ADC map. Their corresponding area on histology displays BPH on Histopathology image (D).

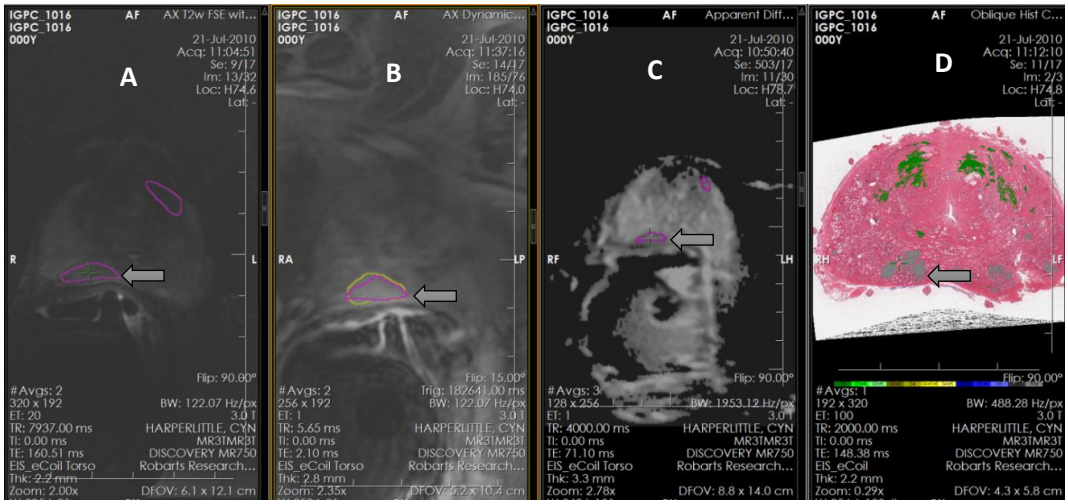

(Figure 3.4) False Positive mpMRI contour correlated to the area with prostatic intraepithelial neoplasia (PIN). (A) A False positive area on T2W MRI image contoured by one observer (gray arrows). (B) Contoured on DCE MRI image, and (C) contoured on ADC map. The corresponding area on histology shows PIN on Histopathology image (D).

The graphs in **(Figure 3.5-3.6)** demonstrate the analysis results of the 37 MRI contoured areas. After corresponding these radiology contoured areas to the corresponding histological regions. This analysis shows the number of each non-cancerous lesion (PIN, Atrophy, BPH, normal histology) and their PI-RADS score assessed on MRI.

The first radiology observer (A) had six years of experience in prostate MRI imaging assessment and PCa diagnosis. This observer contoured seven suspicious lesions in MRI, which were identified on histology to be false positive areas. After corresponding these contoured MRI areas, histology images revealed three lesions of PIN with a PI-RADS score 4. Of the other three atrophic areas, two were given a PI-RADS score 3 and one a PI-RADS score 5 on the contoured unregistered MRI images.

The second radiology observer (B) had five years of experience in prostate MRI assessment. This observer contoured a total of fourteen areas in the MRI images, which were a false positive. Histology images revealed that four of these areas

were PIN, two lesions were marked as PI-RADS score 3, another area was labeled as PI-RADS score 4 and one as PI-RADS score 5. Histology images showed that atrophy was represented in six MRI susceptible lesions. Three areas were assessed as PI-RADS score 3, and the other three were given PI-RADS score 4. BPH was found in three areas, two of them were PI-RADS score 3, and one was a PI-RADS score 4. There was one area assessed as a PI-RADS score 3, which the histology revealed to be a non-pathological central zone structure.

The third radiology observer (C) had two and a half years of experience in prostate MRI assessment. This observer contoured a total of seven areas on MRI, which were false positive areas. Corresponding histology images of contoured MRI areas revealed that five areas were PIN and two were atrophic regions. Of these five areas, two had a PI-RADs score 3, and two had PI-RADs score 4, and one area with PI-RADS score 5 assessments. The PI-RADs score for the two atrophic areas were assessed as score 4 and 5.

The fourth radiology observer (D) also had two and a half years of experience in prostate MRI imaging. This individual contoured a total of nine regions, which were false positive areas. Corresponding histology images to MRI contoured areas with PI-RADS score 3 and above revealed that four areas were PIN. Of these four areas with PIN, one had a PI-RADS score 3, two had a score of 4, and one area had a score 5. Two areas with PI-RADS score 3 and 4 were regions of atrophy. BPH was in one contoured area with PI-RADS score 4, and two areas with normal structure were contoured on MRI as PI-RADS score 4 and 5.

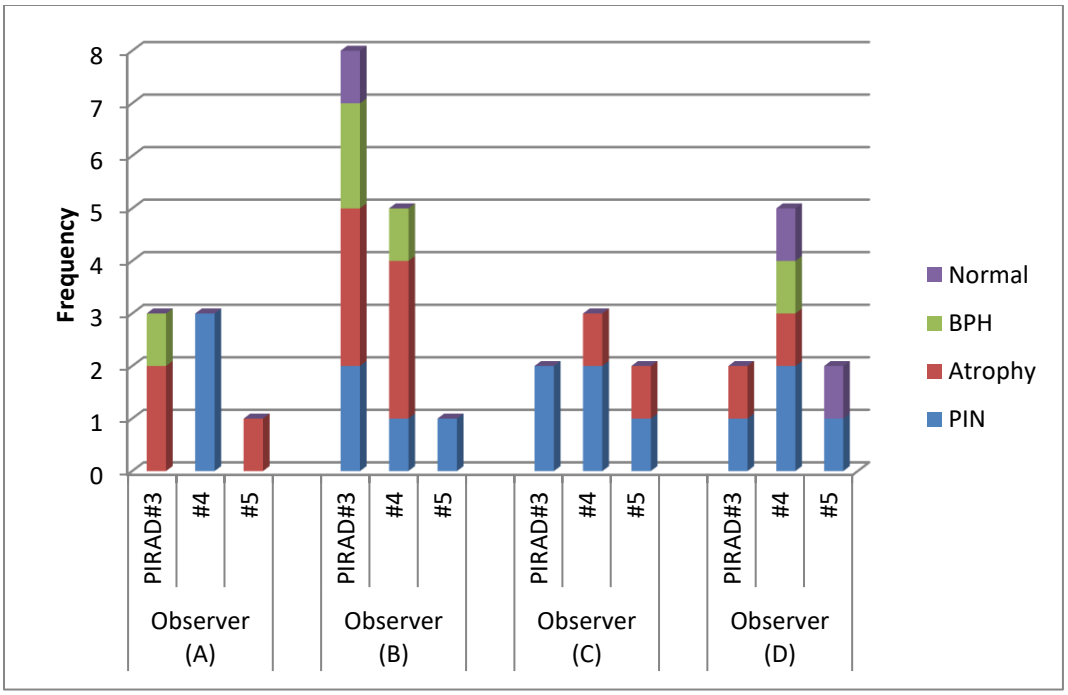

Figure 3.5. Histogram demonstrate the total PI-RADS scores assessment performed by the 4 radiology observers and their corresponding histology findings. Histogram demonstrate the total PI-RADS score assessment contoured by four radiology observers on three functional MRI image sequences (T2W, DCE, ADC) and their corresponding non-cancerous lesions on digital histopathology images (n=19).

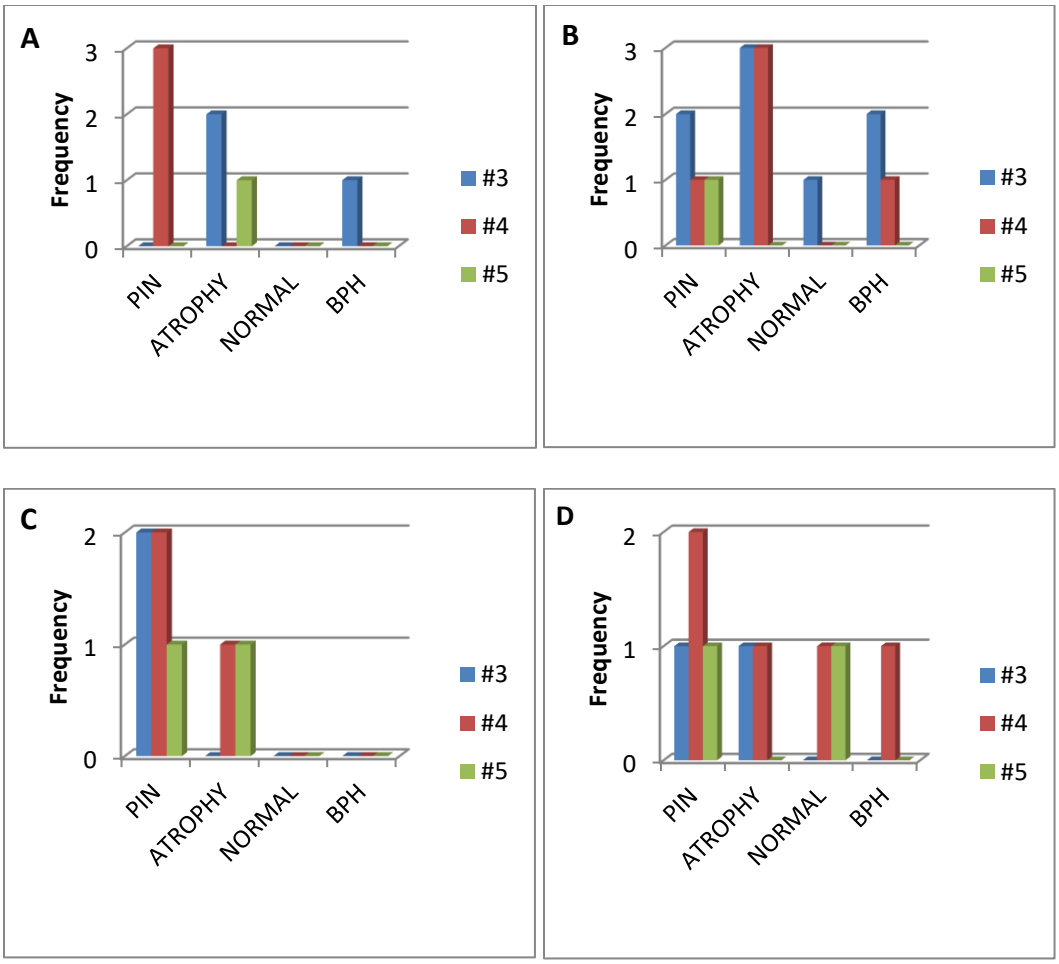

Figure 3.6. Histograms of the frequency of the PI-RADs score of contoured areas on mpMRI by each observer separated by the histologically identified non-cancerous lesions on HDI.

3.2 Analysis of Histology Areas Corresponding to MRI

(**Table 3.1**) shows a summary of the analysis of the histology images, which corresponded to MRI contoured areas. The graphs in (**Figure 3.7**) display the frequency of each non-cancerous lesions (PIN, Atrophy, BPH, normal histology) and their PI-RADS score assessment.

The 23 digital histology images showed that PIN was found in 10 areas. With 8 areas demonstrating solitary PIN and 2 areas with PIN admixed with other non-cancerous lesions. Of the 8 areas with a solitary PIN, 2 areas were found with a flat pattern, 2 areas with a papillary pattern, 2 with tufting and 1 with a cribriform pattern. There are 2 areas found with 2 patterns mixed between flat and tufting and 1 area mixed between papillary and cribriform. The remaining 2 areas admixed with other non-cancerous lesions were found to be a flat pattern, admixed with simple atrophy. The other area was a flat and tufting pattern along with Post-Atrophic Hyperplasia (PAH).

Analysis of these PIN areas, which were contoured 16 times in MRI by the four radiology observers, revealed that five contours were assessed as PI-RADs score 3, eight contours as PI-RADs score 4, and three contours as PI-RADS score 5.

Of the 23 corresponding histology areas to MRI, atrophy was present in seven areas. Of these atrophic areas, 3 areas were found to be with post-atrophic hyperplasia. One area had simple atrophy, and another was mixed between simple and cystic atrophic subtypes. Two atrophic areas were admixed with a PIN, one area displayed simple atrophy and another displayed simple and PAH. These atrophic areas were contoured on MRI thirteen times by the four radiology observers. Six contours were assessed as PI-RADS score 3, five contours were assessed as PI-RADS score 4 and two contours with PI-RADS score 5.

BPH was found to be represented in five areas, which consisted of glandular and stromal components. An epithelial component was represented in 60% or higher in these nodules. On the corresponding MR images, the radiology observers

contoured three of these five areas as PI-RADs score 3 and two areas as PI-RADS score 4.

Normal prostate tissue was present in three areas on the digital histology images, which corresponded to contoured regions on MRI as potential cancerous lesions. One area was in the anterior fibromuscular stroma region, and the other two were in the central zone structure.

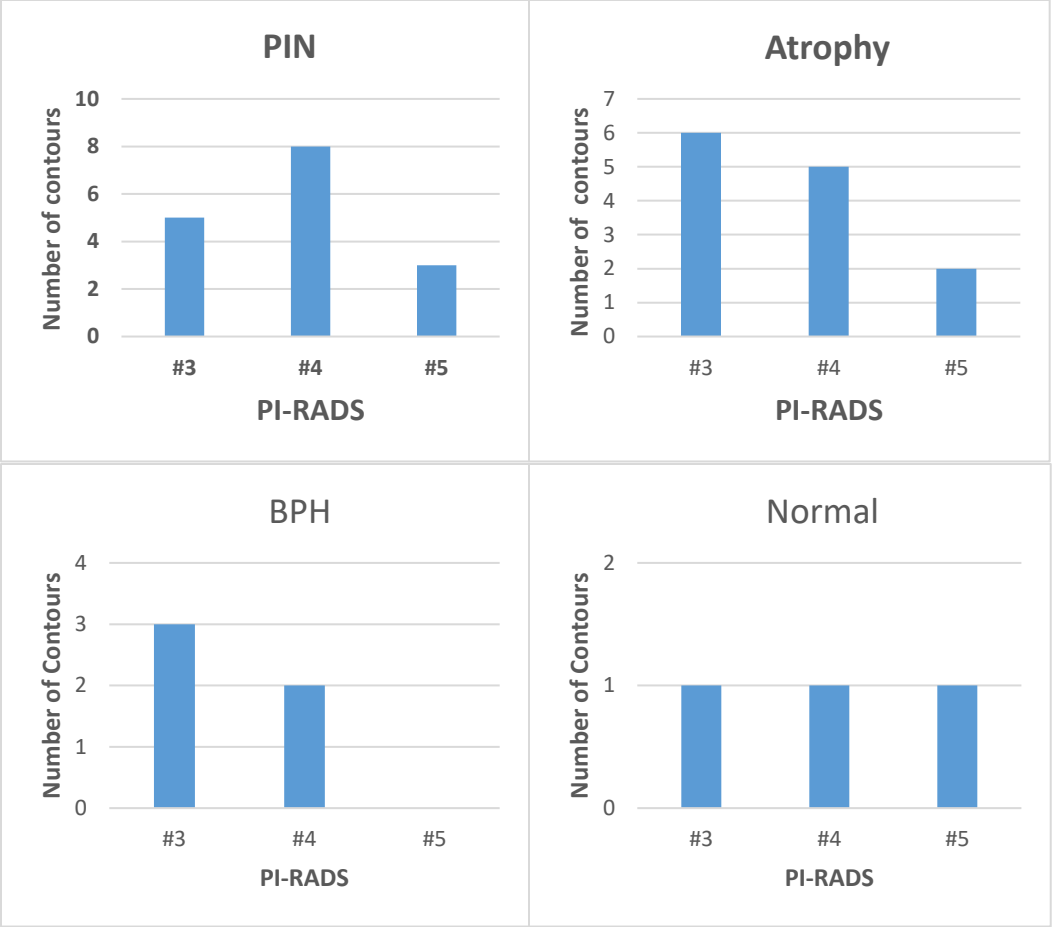

Figure 3.7. Histograms of the frequency of the PI-RADs score for the individual non-cancerous lesions.

Sum of Total areas	PIN	Mixed between PIN & atrophy	Atrophy	BPH	Normal structures
23	8	2	5	5	3

Table 3.1. Summary of the total number corresponding digital histology image areas to contoured MRI areas delineated by four Radiology observers.

3.3 Analysis of PI-RADS Score Corresponding to Histopathology Digital Images

(**Figures 3.7 - 3.9**) show the results of the analysis of each PI-RADS scored area and their frequency of non-cancerous lesion as contoured by the four observers.

PI-RADS score 3 areas were contoured by the four observers fifteen times. The corresponding histopathology images revealed that PIN, atrophy, BPH and a normal structure were represented in 5, 6, 3 and 1 areas respectively.

A PI-RADS score 4 was evaluated and contoured by the four observers on MRI in sixteen areas. The digital histopathology images, which corresponded to MRI contoured areas revealed that PIN, Atrophy, BPH and normal structure were represented in 8, 5, 2 and 1 areas respectively.

A PI-RADS score 5 was assessed six times on MRI by the four radiology observers. The corresponding areas of these MRI contoured areas to histopathology digital images demonstrated PIN, Atrophy, BPH and normal structure presented in 3, 2, 0 and 1 respectively.

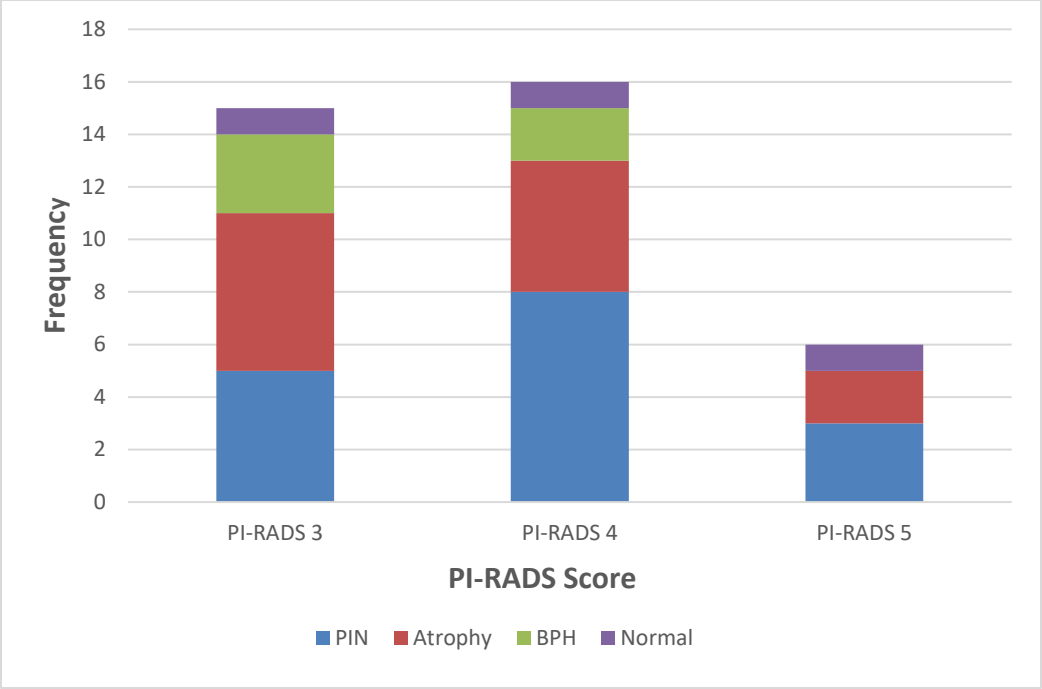

Figure 3.8. Histogram characterizing the total frequency of each PI-RADS score assessment provided by four radiology observers and their corresponding non-cancerous lesions on digital histopathology images (n=19)

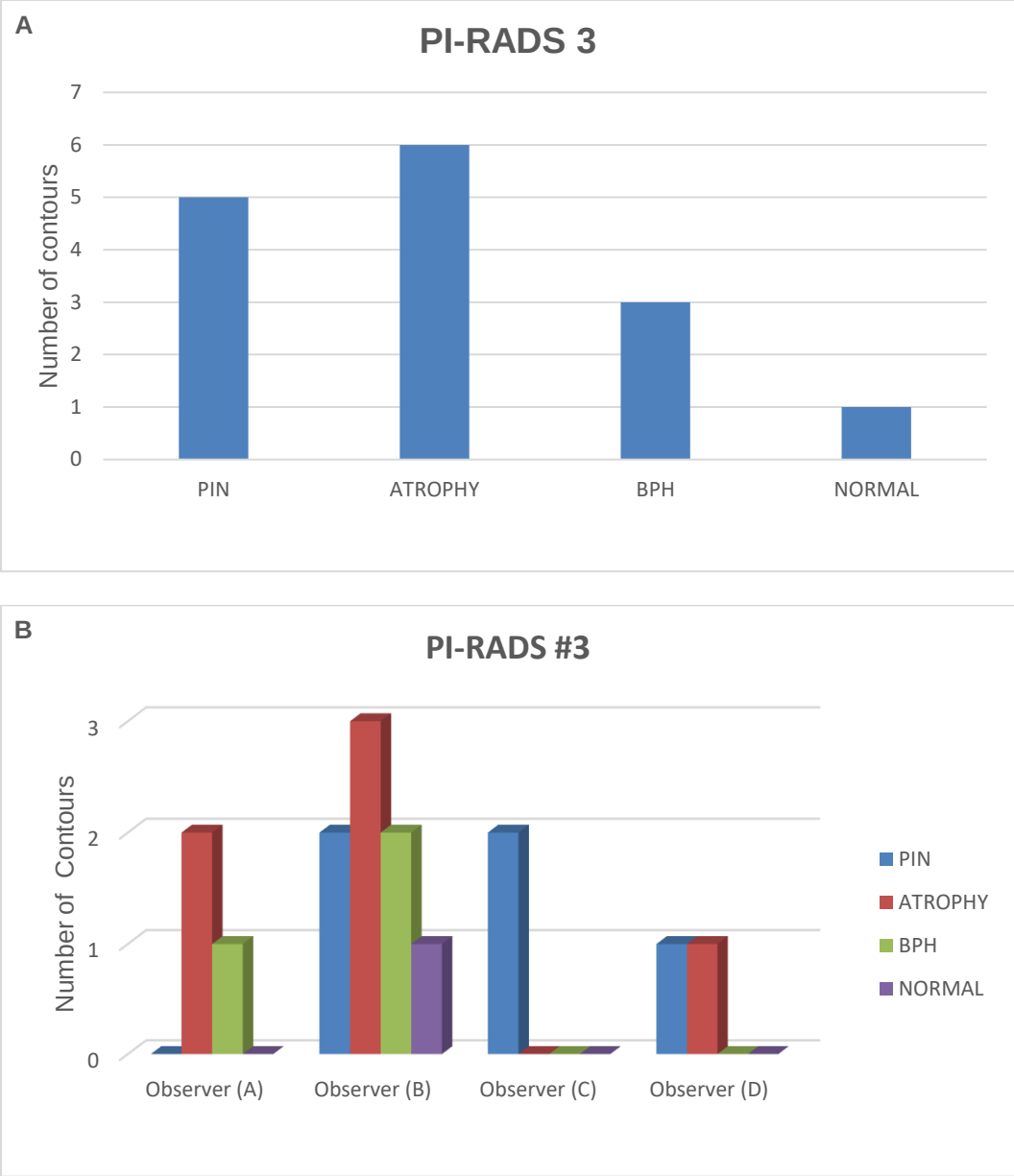

Figure 3.9. Histograms of the frequency of total assessment of PI-RADS score 3 for each of the four observers. (A) The graph shows the total number of PI-RADS score 3 with the corresponding histology of non-cancerous structures on digital image slides (n=19). (B) The graph shows the total number of PI-RADS score 3 assessment by the four observers and their corresponding areas of non-cancerous structures on digital image slides (n=19).

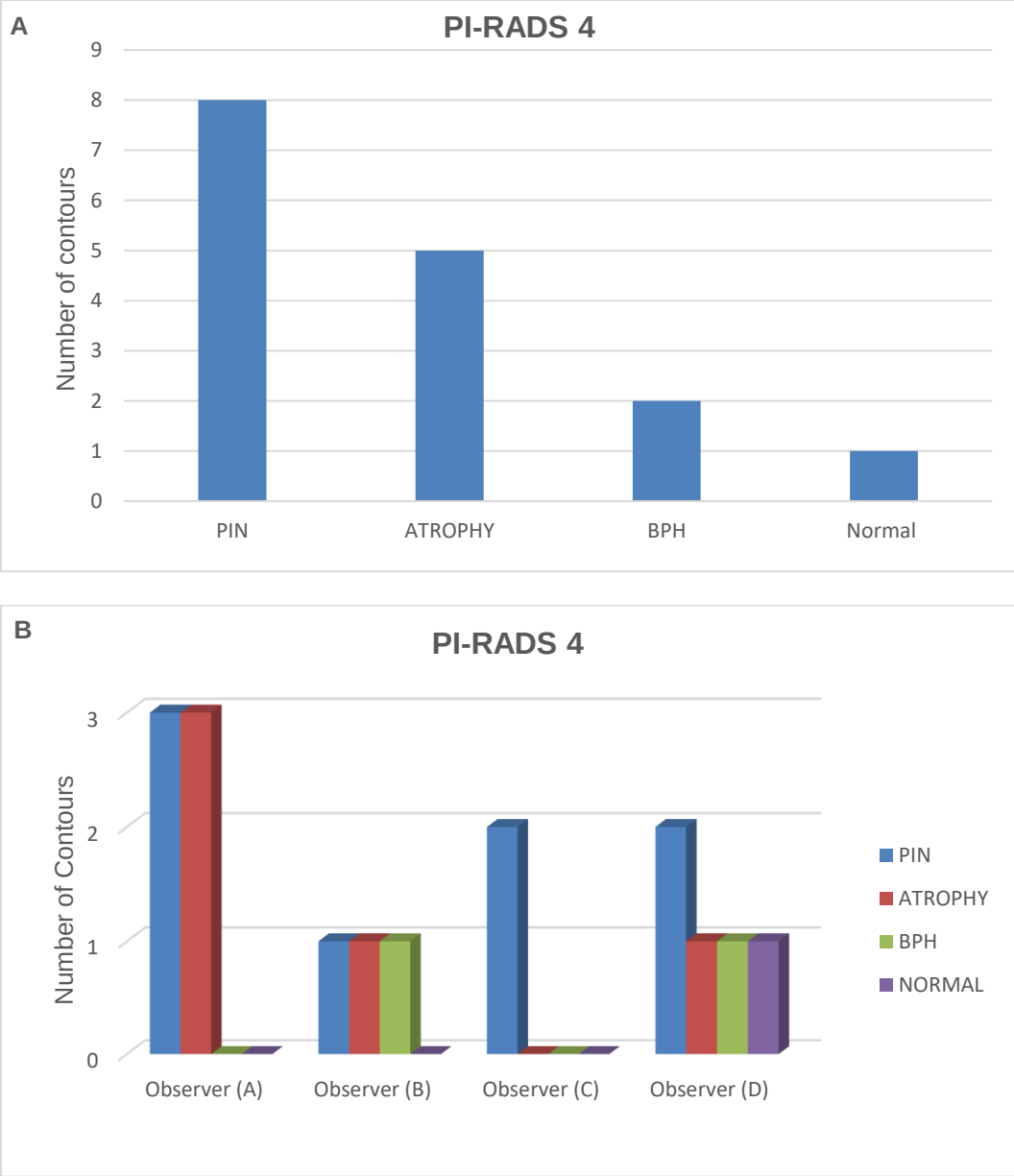

Figure 3.10. Histograms of the frequency of total assessment of PI-RADS score 4 for each of the four observers. (A) The graph shows the total number of PI-RADS score 4 with the corresponding histology of non-cancerous structures on digital image slides (n=19). (B) The graph shows the total number of PI-RADS score 4 assessment by the four observers and the corresponding areas of non-cancerous structures on digital image slides (n=19).

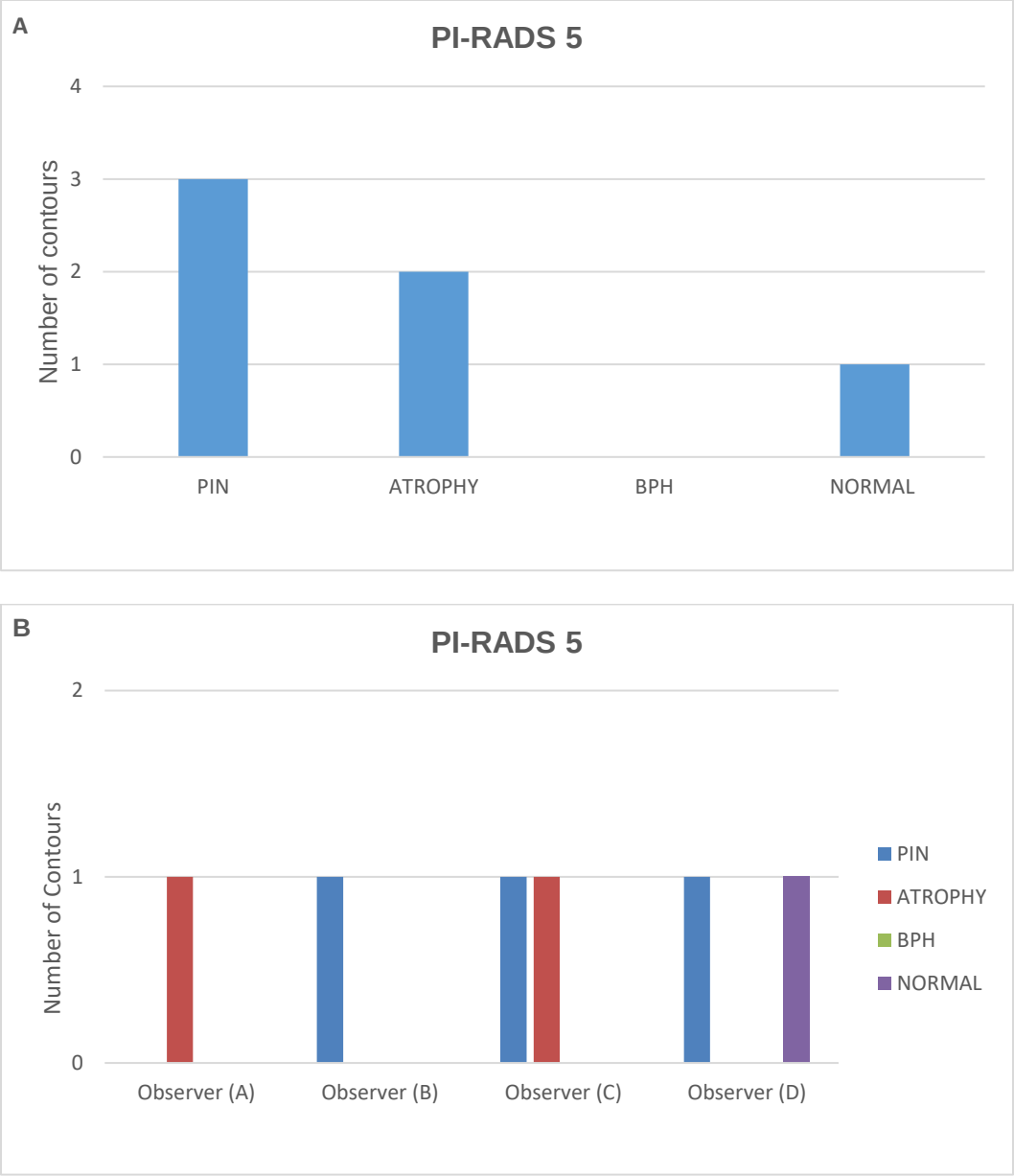

Figure 3.11. Histograms of the frequency of total assessment of PI-RADS score 5 for each of the four observers. (A) The graph shows the total number of PI-RADS score 5 with the corresponding histology of non-cancerous structures on digital image slides (n=19). (B) The graph shows the total number of PI-RADS score 5 assessment by the four observers and the corresponding areas of non-cancerous structures on digital image slides (n=19).

The assessment of the 19 mpMRI prostate surgery cases illustrated that 23 areas on histopathology digital slides corresponded with non-cancerous lesions. These areas were assessed by the four radiology observers as a potential PCa on the corresponding areas in the MRI images. Each of the 23 histopathology areas was individually examined, verified and contoured in the MRI images by at least one or more observers. These areas were contoured a total of 37 times by the observers. Multiple areas were contoured by more than a single radiology observer. (**Table 3.2**) displays the total number of times that the radiology observers contoured areas, which were found to be non-cancerous when the corresponding areas were examined in the histopathology slides.

Examination of the MRI images, which corresponded to the 23 digital histopathology images showed that 16 areas were contoured only by a single observer. Two areas were contoured twice by 2 different observers. Three areas were contoured three times by 3 individual radiology observers. The each of last two remaining areas were contoured by each of the four radiology observers individually. The 2 areas contoured by 4 observers were PIN and Atrophy (simple/cystic). The 3 areas contoured by 3 observers were a PIN. The 2 areas contoured by 2 observers was atrophy (PAH). The remaining 16 areas contoured by a single observer as follow; 3 areas were normal structure, 4 areas were a PIN, 2 areas were mixed between atrophy and PIN, 2 areas were atrophy and 5 areas were BPH.

Table 3.2. The total non-cancerous area on histology and their contoured frequency by radiology observers on the corresponding mpMRI image. The first column shows the total number of non-cancerous areas on histopathology digital images, which were contoured on the MRI images. The other columns show the total number of times the observers contoured the non-cancerous areas on the MRI images by the number of involved radiology observers.

Total involved areas on digital histopathology	Areas contoured by a single observer on mpMRI	Areas contoured by two observers on mpMRI	Areas contoured by three observers on mpMRI	Areas contoured by four observers on mpMRI
23	**16**	**2**	**3**	**2**

Chapter 4

4 Discussion and Conclusion

Prostate Cancer is one of the most common cancers in men, yet screening tools including PSA, DRE, and Transrectal Ultrasound-guided (TRUS) biopsy do not provide the desired high accuracy for PCa early detection and management.

The accuracy of TRUS biopsy is still debated especially in cancer-negative biopsies and the medium rise in PSA levels between 4-10 ng/ml [74]. TRUS biopsy is seen to have a higher chance of discovering large cancer volume rather than higher cancer grades. However, the chance of detecting prostate tumours is lower in the early stages of cancer with a smaller volume. TRUS is still the primary imaging guiding tool for detecting PCa through biopsy [94]. Other studies submitted that only 28% of the prostatectomy specimen is associated with the original cancer grade in biopsy specimens [93]. Higher Gleason grades during biopsy were associated with poorly differentiated cancer after processing the whole prostate specimen following a prostatectomy [93].

The emerging MRI scanning protocol for imaging the prostate gland has a significant role; that is to provide a high-resolution prostate image, assist in detection, diagnosis, and staging the prostate tumour. Multi-parametric MRI (mpMRI) is not only involved in prostate cancer diagnosis but also in management. A controversial disagreement is present between Radiologists and Urologists on when mpMRI images should be prescribed [96]. Radiologists claim that biopsies will result in prostate haemorrhage that could take several months to resolve. Haemorrhage and bleeding parenchymal spots will alter prostate MRI assessments, which is a challenging for accurate tumour localization. The mpMRI could provide a highly, detailed anatomy of the prostate gland and surrounding structures assisting in determining the location for lesion sampling. The current guideline sets the MRI after a prostate biopsy associated with no tumour detection. On the other hand, the financial and logistic problems accompanying MRI are still one of the leading hindrances. Many imaging centers do not have the

capacity or equipment to compensate for a high number of patients for regular prostate screening MRI scans.

The sensitivity and specificity of cancer detection with mpMRI reaches 80% for clinically significant cancer volume more than 0.5 cc in the anterior area of the prostate. This percentage increases to 90% for cancer located in the posterior gland [135]. The MRI sensitivity for detecting small prostate cancer volume (less than 0.5cc) is low; however, about 98% of these undetectable cancer lesions on MRI are low-grade prostate cancer [126, 136]. Prostate tumour volume less than 0.5 cc is unlikely to be associated with aggressive disease, especially if it is a pure Gleason grade 3 and Gleason score 6 [137]. The initial aim for prostate MRI is to detect the most significant tumour, not every single lesion compared to breast MRI's [126]. Relative to TRUS, mpMRI is more accurate in detecting gland volume with adjacent anatomical structures and extra-prostatic extension (EPE) [93].

The PI-RADS score system is a developing tool for assessing and differentiating the presence of prostate tumours and non-cancerous lesions in prostate gland MRI images. The probability of prostate tumour evidence is directly proportioned with the higher overall PI-RADS score. The PI-RADS score may also be used as a tool for assessing tumour aggressiveness and extra-prostatic extension. The overall PI-RADS score 1 and 2 reveal that the probability of cancer is very unlikely. It is associated with the high probability of benign lesions being present. The overall PI-RADS score 4 and 5 are reflect the high probability of existing cancer. PI-RADS score 3 acts as an intermediate zone between 2 possibilities [123]. Our data demonstrates that PI-RADS score 3 was specified in 15 radiology contours on mpMRI images. PI-RADS score 4 was labeled in 16 radiology contours compared to 6 contours labeled with PI-RADS score 5. None of these contours were correlated to a prostate tumour area on histopathological images. In fact, these contours were correlated to non-cancerous abnormalities that have been described in the Results section above.

Our study provides preliminary results on the relationship between non-cancerous abnormalities that could mimic cancer-like signals on prostate gland mpMRI and digital histopathology images. In our study, the non-rigid Target Registration Error (TRE) of MRI to histopathology digital images was 1.1 ± 0.7 mm [129]. In other studies, these relationships have not been examined with the same accuracy for the correlation between digital histology images and mpMRI images as completed in our study.

The analysis of our study should be interpreted within the context of the study population. The analysis of 19 prostatectomy specimens shows that BPH, HGPIN, Atrophy and normal structure (CZ, AFMS) were presented in 37 radiology contours as potential lesions of PCa. These non-cancerous lesions had displayed cancer like signals on mpMRI along with an assessment of PI-RADS score ranging from 3 to 5 by our 4 radiology observers.

BPH was present in 5 histopathology areas with PI-RADS score 3 and 4. PI-RADS score 3 was assigned to 3 BPH areas out of 5. The remaining 2 areas were assessed as PI-RADS score 4. The BPH tissue in these 5 areas was composed of the glandular and stromal components. The glandular component was the major element of these nodules with minimal stromal tissue within BPH nodules. Visual qualitative assessment of these nodules revealed that glandular component composed of at least 70% to 80% of BPH areas with minimal stromal tissue in-between.

PIN is widely accepted as a known PCa precursor due to the similarity in genetic and cell morphology except in acini basement membrane invasion, which is associated with PCa. PIN includes 4 main morphological patterns: papillary, tufting, flat and cribriform. However, no known clinical significant impact exists between these different types of patterns. Their recognition arises from the diagnostic efficacy.

Our data revealed that PIN was represented in 10 histopathological areas with no dominant or consistent pattern. Each of these patterns (tufting, papillary and flat) was represented in 2 areas. The cribriform pattern was represented in 1 area, and

mixed pattern between flat and tufting was represented in 2 areas. Another mixed pattern between papillary and cribriform type was present in 1 area.

PIN features include hypercellularity, accompanied by basophilic appearance similar to prostate adenocarcinoma. Although the PIN glands are usually relatively larger in size compared to PCa glands, the basal cell layer is still abrupt, discontinued, or in countless cases are not visible especially with H&E stain. This is a characteristic feature for PCa as well. The PIN nuclear complex features include nuclear enlargement, crowding, and hyperchromasia are another typical findings in PCa cells. With PIN involvement, it is difficult to draw a clear separation of atypical or normal cells from nuclear presentation based on H&E stain only. Most of the time, additional immunohistochemical staining is required for further differentiation especially in prostate gland biopsy tissue. In addition to the loss of basal cell layer, hypercellularity and hyperchromasia are responsible for the decreased water permeability and restriction in fluid transfer between cells and between intracellular and extracellular space. This results in low water content in the zonal tissue similar to cancer features. The diminished water tissue content responsible for low signal intensity in T2W sequence and the hypointense signal on ADC map are the same findings in existing PCa.

The similarity in histologic features between PIN and PCa cells such as cellular, nuclear and glandular features are accountable for the major portion in signal similarity on mpMRI.

Atrophy was found in 7 histopathological areas. The Post-Atrophic hyperplasia (PAH) represented the majority of atrophic glandular changes. PAH was present in 4 areas, 3 areas with PAH, and one area mixed with a flat pattern of PIN. Another area with cystic atrophy was present with PIN features mixed with patterns between flat and tufting. Simple atrophy was present in 1 area. A mix between PAH and simple atrophic gland was present in 1 area. In general, the Atrophic glands are accompanied by inflammatory cells. Our data illustrates no large significant inflammatory cell patches in-between atrophic glands correlated to cancer like signal on mpMRI. The basal cell layer is diminished in glands with

atrophic features. Occasionally a complete lack of basal cells are seen. This feature presents itself in adenocarcinoma of the prostate. In the case of PAH, the glands appear basophilic at low power. The multiple, small acini packing is responsible for the hyperplastic appearance with an increase in cellularity compared to normal glandular tissue. The nucleolar may also display mild to moderate enlargement. This is also a feature of PCa and could raise confusion in distinguishing between PAH and prostate adenocarcinoma in the pathology setting. The similarities between PCa and atrophy are hypercellularity, mild to moderate nuclear, nucleolar enlargement, and attenuated to complete lack of basal cell layer could be responsible for a similar signal on mpMRI.

The remaining 3 histopathological areas were represented by a normal or non-pathological structure. The normal central zone glandular component was represented in 2 areas. The CZ glands are more complex compared to PZ glands with significant papillary foldings and piled up nuclei. These features increase the possibility for CZ glands to be diagnosed as a PIN. Anterior-fibromuscular stroma was present in the last remaining area.

Our data showed that the 2 histopathology areas that were contoured by 4 observers were atrophy and PIN. The atrophy area contained a mix of cystic and simple atrophy sub-type. The PIN area demonstrated a papillary pattern.

Our study required approximately 3 extra days of processing compared to regular histology processing time. This processing time is for fiducial applications, apex, base, and mid-gland sectioning and photographing formalin sections. A set of *ex vivo* MRI images were aquired after fiducial applications. This results in the delay of the pathological assessment by 4-5 days.

One of the technical challenges of the study is the registration between histopathology digital images and *in vivo* mpMRI images for the apex first cut. This is performed through an interactive digital technique using T2W, T1W and *ex vivo* MRI images of the prostate gland specimens after prostatectomy.

The clinical pathology processing protocol allows only prostate mid-gland for whole-mount slicing. The whole-mount blocks ranged between 3 to 5 blocks per

prostate specimen depending on the prostate gland shape and volume. This procedure excluded the assessment of the apex and base of the prostate in correlation with mpMRI due to lack of registration between digital histopathology images of apex and base and mpMRI images.

The results included multiple observers involved in the radiology contours, which displayed a significant inter-observer variability. Sixteen areas were contoured with a single observer, two areas were contoured with 2 observers, three areas were contoured with 3 observers and 2 areas contoured with 4 observers. Also, through case examinations, some areas with adenocarcinoma on the digital histopathology images were not associated with any radiology contours or recognition on mpMRI images by the 4 radiology observers. Further investigations are required to explore the cause of this finding as this was beyond the scope of this study.

The assessment of mpMRI by 4 radiology observers was achieved using PI-RADS score V1. The PI-RADS score V1 went through some amendments to increase clarity and reduce inter-observer variability. PI-RADS version 2 (V2) was published in 2015 as a result of these acquired changes [138]. The PI-RADS V2 has introduced the concepts of domain sequence in assessing prostate zonal anatomy [138]. DWI was assigned as a domain sequence in PZ assessment since T2W images were accompanied by the lack of specificity with low signal intensity [138]. The T2W low signal intensity may have occurred from non-cancerous lesions such as inflammation (acute or chronic) or haemorrhage. The DCE sequence comes secondary to DWI in evaluating PZ. The DCE went from a 5 points score to a positive or negative assessment, which reflects the possibility of the presence or absence of cancer respectively [138]. Score 3 on DWI should be upgraded to score 4 if corresponding DCE area shows a positive signal. Additionally, lesion size and shape were introduced as factors in the assessment. The cut-off size is ≥1.5 cm upgraded score 4 to score 5. DWI scoring categories went through major modification in V2 in contrast to V1. The primary sequence in evaluating TZ is a T2W image. The BPH in TZ accompanied by increased cellularity and reduced diffusion raising the suspicion for PCa presence. The cut-

off size lesion is ≥1.5 cm between score 4 and 5, which was not considered an influence on V1. It is still early to evaluate how significant PI-RADS classification amendments will impact the clinical diagnostic performance. Further changes may be implemented in the future. Some studies concluded that the modification included in V2 has increased the sensitivity in assessing TZ compared to V1; however, the sensitivity of PZ assessment is slightly better with the V1 scoring system [139]. Our radiology observers' assessment was performed according to PI-RADS V1 prior to PI-RADS V2 publication. From the comparison between the two versions, our data could be slightly impacted by increasing the sensitivity in TZ evaluation. Our data demonstrated 5 areas that were contoured as potential cancerous lesions in TZ on mpMRI with BPH finding on corresponding histopathology images. Three of these 5 areas were classified as score 3 and the remaining 2 were classified as PI-RADS score 4. Training and experience will play an essential role in interpreting prostate mpMRI images since there was a significant inter-observer variability between radiology observers associated with variable years of experience.

Overall, our study demonstrated the relationship between false positive cancer like signals on prostate gland mpMRI and their corresponding pathological non-cancerous abnormalities. Our data showed 3 major categories of non-cancerous lesions (Atrophy, PIN, and BPH) associated with the false positive mpMRI signals. The examination of these 3 major categories revealed no consistent pattern or subtypes responsible for this signal similarity with cancer on mpMRI images. Surprisingly, our data displayed no inflammation, whether, acute or chronic, which were associated with false positive cancer signal on mpMRI.

The use of our current research method with a larger sample size may provide a vital tool in better understanding and answering the previous research questions regarding developing a map of non-cancerous pathology lesions and their signals on mpMRI.

More research should be directed towards the relationship between multiple non-cancerous pathology lesions present in the same zone and their signals on

mpMRI. The examination of areas that contain multiple mixed types of non-cancerous abnormalities could provide essential data when correlated to mpMRI signals. Together with the above recommendations, the stromal glandular ratio should be examined in correlation to mpMRI signals. The attenuated, disruptive or even complete absence of basal cell layer is an existing co-finding between prostate adenocarcinoma and other non-cancerous lesions such as PIN and atrophy. Further quantitative and qualitative assessment of the basal cell layer and its relationship to water permeability and fluid restriction may provide valuable data on basal cell presence and its impact on mpMR images. This relationship may have a significant input in understanding the similarity between adenocarcinoma and other non-cancerous lesions on mpMR images. This data, in collaboration with further research, can assist in improving the differentiation between cancerous and non-cancerous lesions, reducing the rate of false positive diagnosis of PCa on MRI.

Chapter 5

5 Reference

1. Ferlay, J., et al., *Cancer incidence and mortality worldwide: Sources, methods and major patterns in GLOBOCAN 2012.* International Journal of Cancer. **136**(5): p. E359-E386.
2. Hankey, B.F., et al., *Cancer surveillance series: interpreting trends in prostate cancer--part I: Evidence of the effects of screening in recent prostate cancer incidence, mortality, and survival rates.* J Natl Cancer Inst, 1999. **91**(12): p. 1017-24.
3. Center, M.M., et al., *International Variation in Prostate Cancer Incidence and Mortality Rates.* European Urology, 2012. **61**(6): p. 1079-1092.
4. 2015, C.C.S., *Canadian Cancer Society's Advisory Committee on Cancer Statistics.* 2015.
5. Brawley, O.W., *Prostate cancer epidemiology in the United States.* World Journal of Urology, 2012. **30**(2): p. 195-200.
6. Tao, Z.Q., et al., *Epidemiology of prostate cancer: current status.* Eur Rev Med Pharmacol Sci, 2015. **19**(5): p. 805-12.
7. Shavers, V.L.P., W.I.I.I.M.D.M.S.M.P.H. Underwood, and R.P.P. Moser, *Race/Ethnicity, Risk Perception, and Receipt of Prostate-Specific Antigen Testing.* Journal of the National Medical Association, 2009. **101**(7): p. 698-704.
8. Freedland, S.J. and W.B. Isaacs, *Explaining racial differences in prostate cancer in the United States: Sociology or biology?* The Prostate. **62**(3): p. 243-252.
9. Mahal, B.A., et al., *Racial disparities in an aging population: The relationship between age and race in the management of African American men with high-risk prostate cancer.* Journal of Geriatric Oncology. **5**(4): p. 352-358.
10. Powell, I.J., et al., *Evidence supports a faster growth rate and/or earlier transformation to clinically significant prostate cancer in black than in*

white American men, and influences racial progression and mortality disparity. J Urol, 2010. **183**(5): p. 1792-6.

11. Arcangeli, S., V. Pinzi, and G. Arcangeli, *Epidemiology of prostate cancer and treatment remarks.* World Journal of Radiology, 2012. **4**(6): p. 241-246.
12. Billis, A., *Latent carcinoma and atypical lesions of prostate. An autopsy study.* Urology, 1986. **28**(4): p. 324-9.
13. Haas, G.P., et al., *The Worldwide Epidemiology of Prostate Cancer: Perspectives from Autopsy Studies.* The Canadian journal of urology, 2008. **15**(1): p. 3866-3871.
14. Bechis, S.K., P.R. Carroll, and M.R. Cooperberg, *Impact of Age at Diagnosis on Prostate Cancer Treatment and Survival.* Journal of Clinical Oncology, 2011. **29**(2): p. 235-241.
15. Gandaglia, G., et al., *The effect of age at diagnosis on prostate cancer mortality: A grade-for-grade and stage-for-stage analysis.* European Journal of Surgical Oncology. **40**(12): p. 1706-1715.
16. Zeegers, M.P., A. Jellema, and H. Ostrer, *Empiric risk of prostate carcinoma for relatives of patients with prostate carcinoma: a meta-analysis.* Cancer, 2003. **97**(8): p. 1894-903.
17. Hemminki, K., *Familial risk and familial survival in prostate cancer.* World J Urol, 2012. **30**(2): p. 143-8.
18. Cheng, I., et al., *Socioeconomic status and prostate cancer incidence and mortality rates among the diverse population of California.* Cancer Causes Control, 2009. **20**(8): p. 1431-40.
19. Rundle, A., et al., *A prospective study of socioeconomic status, prostate cancer screening and incidence among men at high risk for prostate cancer.* Cancer Causes & Control, 2013. **24**(2): p. 297-303.
20. Allen, N.E., et al., *Animal foods, protein, calcium and prostate cancer risk: the European Prospective Investigation into Cancer and Nutrition.* The British Journal of Cancer, 2008. **98**(9): p. 1574-81.

21. Augustsson, K., et al., *A prospective study of intake of fish and marine fatty acids and prostate cancer.* Cancer Epidemiol Biomarkers Prev, 2003. **12**(1): p. 64-7.

22. Vogt, T.M., et al., *Serum selenium and risk of prostate cancer in U.S. blacks and whites.* Int J Cancer, 2003. **103**(5): p. 664-70.

23. Allen, N.E., et al., *A case--control study of selenium in nails and prostate cancer risk in British men.* Br J Cancer, 2004. **90**(7): p. 1392-6.

24. Lippman, S.M., et al., *Effect of selenium and vitamin E on risk of prostate cancer and other cancers: the Selenium and Vitamin E Cancer Prevention Trial (SELECT).* Jama, 2009. **301**(1): p. 39-51.

25. Singh, B.P., et al., *Status and Interrelationship of Zinc, Copper, Iron, Calcium and Selenium in Prostate Cancer.* Indian Journal of Clinical Biochemistry, 2015. **31**(1): p. 50-56.

26. Freedland, S.J., E. Giovannucci, and E.A. Platz, *Are findings from studies of obesity and prostate cancer really in conflict?* Cancer Causes Control, 2006. **17**(1): p. 5-9.

27. Gong, Z., et al., *Obesity, diabetes, and risk of prostate cancer: results from the prostate cancer prevention trial.* Cancer Epidemiol Biomarkers Prev, 2006. **15**(10): p. 1977-83.

28. Freedland, S.J. and E.A. Platz, *Obesity and prostate cancer: making sense out of apparently conflicting data.* Epidemiol Rev, 2007. **29**: p. 88-97.

29. Marshall, J., *Diet and prostate cancer prevention.* World Journal of Urology, 2012. **30**(2): p. 157-165.

30. Freedland, S.J., et al., *Obesity Is a Significant Risk Factor for Prostate Cancer at the Time of Biopsy*. Urology, 2008. **72**(5): p. 1102-1105.

31. Allott, E.H., E.M. Masko, and S.J. Freedland, *Obesity and Prostate Cancer: Weighing the Evidence.* European Urology, 2013. **63**(5): p. 800-809.

32. Price, A.J., et al., *Insulin-like growth factor-I concentration and risk of prostate cancer: results from the European Prospective Investigation into*

Cancer and Nutrition. Cancer Epidemiol Biomarkers Prev, 2012. **21**(9): p. 1531-41.

33. McNeal, J.E., *Normal and pathologic anatomy of prostate.* Urology, 1981. **17**(Suppl 3): p. 11-6.
34. Everaerts, W. and A.J. Costello, *Applied Anatomy of the Male Pelvis*, in *Prostate Ultrasound: Current Practice and Future Directions*, R.C. Porter and M.E. Wolff, Editors. 2015, Springer New York: New York, NY. p. 11-30.
35. Mills, S.E., *Histology for Pathologist*. 2012, Wolters Kluwer. p. 987-1002.
36. Fine, S.W. and V.E. Reuter, *Anatomy of the prostate revisited: implications for prostate biopsy and zonal origins of prostate cancer.* Histopathology. **60**(1): p. 142-152.
37. Hayward, S.W., M.A. Rosen, and G.R. Cunha, *Stromal-epithelial interactions in the normal and neoplastic prostate.* Br J Urol, 1997. **79 Suppl 2**: p. 18-26.
38. Dauge, M.C., V. Delmas, and C.A. Mandarim de Lacerda, *[Development of the human prostate during the first stages of fetal life. Morphometric study]*. Bull Assoc Anat (Nancy), 1986. **70**(211): p. 5-11.
39. McNeal, J.E., *Normal histiology of the prostate.* American Journal of Surgical Pathology, 1988. **12**(8): p. 619-633.
40. McNeal, J.E., *The zonal anatomy of the prostate.* Prostate, 1981. **2**(1): p. 35-49.
41. McNeal, J.E., *The prostate and prostatic urethra: a morphologic synthesis.* J Urol, 1972. **107**(6): p. 1008-16.
42. McNeal, J.E., *Origin and evolution of benign prostatic enlargement.* Invest Urol, 1978. **15**(4): p. 340-5.
43. Selman, S.H., *The McNeal Prostate: A Review.* Urology, 2011. **78**(6): p. 1224-1228.
44. Bostwick, D.G. and L. Cheng, *Urologic surgical pathology*. Vol. Thirdition. 2014, Philadelphia, PA: Elsevier Saunders.

45. Lee, S., et al., *Reliable identification of transition zone prostatic adenocarcinoma in preoperative needle core biopsy.* Human Pathology, 2013. **44**(10): p. 2331-2337.

46. Cohen, R.J., et al., *Prediction of bladder neck invasion and tumor extension to bladder neck margin by prostatic adenocarcinoma: a nomogram using biopsy data including transition zone tumor morphology.* Human pathology, 2016. **57**: p. 85-90.

47. McNeal, J.E., et al., *Capsular penetration in prostate cancer. Significance for natural history and treatment.* Am J Surg Pathol, 1990. **14**(3): p. 240-7.

48. Ayala, A.G., et al., *The prostatic capsule: does it exist? Its importance in the staging and treatment of prostatic carcinoma.* Am J Surg Pathol, 1989. **13**(1): p. 21-7.

49. Garcia-Monaco, R., et al., *Human cadaveric specimen study of the prostatic arterial anatomy: implications for arterial embolization.* J Vasc Interv Radiol, 2014. **25**(2): p. 315-22.

50. Bilhim, T., et al., *Radiological anatomy of prostatic arteries.* Tech Vasc Interv Radiol, 2012. **15**(4): p. 276-85.

51. Walsh, P.C., *Radical retropubic prostatectomy with reduced morbidity: an anatomic approach.* NCI Monogr, 1988(7): p. 133-7.

52. Huri, E., *Novel anatomical identification of nerve-sparing radical prostatectomy: fascial-sparing radical prostatectomy.* Prostate Int, 2014. **2**(1): p. 1-7.

53. Daneshmand, S., et al., *Ethnic differences in neuroendocrine cell expression in normal human prostatic tissue.* Urology. **65**(5): p. 1008-1012.

54. Noordzij, M.A., et al., *The prognostic influence of neuroendocrine cells in prostate cancer: results of a long-term follow-up study with patients treated by radical prostatectomy.* Int J Cancer, 1995. **62**(3): p. 252-8.

55. Srigley, J.R., *Benign mimickers of prostatic adenocarcinoma.* Modern Pathology, 2004. **17**(3): p. 328-348.

56. De Marzo, A.M., et al., *A working group classification of focal prostate atrophy lesions.* American Journal of Surgical Pathology, 2006. **30**(10): p. 1281-1291.

57. Davidsson, S., et al., *Inflammation, focal atrophic lesions, and prostatic intraepithelial neoplasia with respect to risk of lethal prostate cancer.* Cancer Epidemiol Biomarkers Prev, 2011. **20**(10): p. 2280-7.

58. Billis, A., *Prostatic atrophy. Clinicopathological significance.* Int Braz J Urol, 2010. **36**(4): p. 401-9.

59. Ruska, K.M., J. Sauvageot, and J.I. Epstein, *Histology and cellular kinetics of prostatic atrophy.* Am J Surg Pathol, 1998. **22**(9): p. 1073-7.

60. Bostwick, D.G., et al., *Architectural Patterns of High-Grade Prostatic Intraepithelial Neoplasia.* Human Pathology, 1993. **24**(3): p. 298-310.

61. Bostwick, D.G. and L. Cheng, *Precursors of prostate cancer.* Histopathology, 2012. **60**(1): p. 4-27.

62. A. Sakr, A.B.P.E.T.W.D.G.B.W., *Epidemiology of High-Grade Prostatic Intraepithelial Neoplasia.* Scandinavian Journal of Urology and Nephrology, 2000. **34**(205): p. 11-18.

63. Sakr, W.A., *Prostatic Intraepithelial Neoplasia: A Marker for High-Risk Groups and a Potential Target for Chemoprevention.* European Urology, 2012. **35**(5-6): p. 474-478.

64. Fowler, J.E., Jr., et al., *Prospective study of correlations between biopsy-detected high grade prostatic intraepithelial neoplasia, serum prostate specific antigen concentration, and race.* Cancer, 2001. **91**(7): p. 1291-6.

65. Joniau, S., et al., *Prostatic Intraepithelial Neoplasia (PIN): Importance and Clinical Management.* European Urology, 2005. **48**(3): p. 379-385.

66. Dema, A., et al., *Unusual patterns of high-grade prostatic intraepithelial neoplasia: morphological and immunohistochemical aspects.* Virchows Archiv, 2011. **459**: p. S278-S279.

67. Epstein, J.I. and M. Herawi, *Prostate needle biopsies containing prostatic intraepithelial neoplasia or atypical foci suspicious for carcinoma: implications for patient care.* J Urol, 2006. **175**(3 Pt 1): p. 820-34.

68. Lopez, J.I., *Prostate adenocarcinoma detected after high-grade prostatic intraepithelial neoplasia or atypical small acinar proliferation.* BJU Int, 2007. **100**(6): p. 1272-6.

69. Bishara, T., D.M. Ramnani, and J.I. Epstein, *High-grade prostatic intraepithelial neoplasia on needle biopsy - Risk of cancer on repeat biopsy related to number of involved cores and morphologic pattern.* American Journal of Surgical Pathology, 2004. **28**(5): p. 629-633.

70. McNicholas, T. and D. Swallow, *Benign prostatic hyperplasia.* Surgery (Oxford), 2011. **29**(6): p. 282-286.

71. McNeal, J.E., *Anatomy of the prostate and morphogenesis of BPH.* Prog Clin Biol Res, 1984. **145**: p. 27-53.

72. Bostwick, D.G., et al., *The association of benign prostatic hyperplasia and cancer of the prostate.* Cancer, 1992. **70**(1 s): p. 291-301.

73. Kristal, A.R., et al., *Race/Ethnicity, Obesity, Health Related Behaviors and the Risk of Symptomatic Benign Prostatic Hyperplasia: Results From the Prostate Cancer Prevention Trial.* The Journal of Urology, 2007. **177**(4): p. 1395-1400.

74. Gretzer, M.B. and A.W. Partin, *PSA Levels and the Probability of Prostate Cancer on Biopsy.* European Urology Supplements, 2002. **1**(6): p. 21-27.

75. Pezaro, C., H.H. Woo, and I.D. Davis, *Prostate cancer: measuring PSA.* Internal Medicine Journal, 2014. **44**(5): p. 433-440.

76. Balk, S.P., Y.-J. Ko, and G.J. Bubley, *Biology of Prostate-Specific Antigen.* Journal of Clinical Oncology, 2003. **21**(2): p. 383-391.

77. Adhyam, M. and A. Gupta, *A Review on the Clinical Utility of PSA in Cancer Prostate.* Indian Journal of Surgical Oncology, 2012. **3**(2): p. 120-129.

78. Christensson, A., et al., *Serum prostate specific antigen complexed to alpha 1-antichymotrypsin as an indicator of prostate cancer.* J Urol, 1993. **150**(1): p. 100-5.

79. Gretzer, M.B. and A.W. Partin, *PSA markers in prostate cancer detection.* Urol Clin North Am, 2003. **30**(4): p. 677-86.

80. Crawford, E.D., et al., *Prostate-specific antigen 1.5–4.0 ng/mL: a diagnostic challenge and danger zone.* BJU International, 2011. **108**(11): p. 1743-1749.

81. Crawford, E.D., et al., *An Approach Using PSA Levels of 1.5 ng/mL as the Cutoff for Prostate Cancer Screening in Primary Care.* Urology (Ridgewood, N.J.), 2016. **96**: p. 116-120.

82. Oesterling, J.E., et al., *Serum prostate-specific antigen in a community-based population of healthy men. Establishment of age-specific reference ranges.* JAMA, 1993. **270**(7): p. 860-4.

83. Elliott, C.S., R. Shinghal, and J.C. Presti, *Racial Variations in the Performance of Prostate Specific Antigen and Prostate Specific Antigen Density in the Era of Extended Prostate Biopsy Schemes.* The Journal of Urology, 2008. **180**(4): p. 1318-1324.

84. Morgan, T.O., et al., *Age-specific reference ranges for prostate-specific antigen in black men.* The New England journal of medicine, 1996. **335**(5): p. 304-310.

85. Walsh, P.C., *Re: Long-Term Effects of Finasteride on Prostate Specific Antigen Levels: Results From the Prostate Cancer Prevention Trial: R. D. Etzioni, N. Howlader, P. A. Shaw, D. P. Ankerst, D. F. Penson, P. J. Goodman and I. M. Thompson J Urol, 174: 877–881, 2005.* The Journal of Urology, 2006. **176**(1): p. 409-410.

86. Catalona, W.J., et al., *Use of the percentage of free prostate-specific antigen to enhance differentiation of prostate cancer from benign prostatic disease: a prospective multicenter clinical trial.* Jama, 1998. **279**(19): p. 1542-7.

87. Luboldt, H.J., et al., *Clinical usefulness of free PSA in early detection of prostate cancer.* Onkologie, 2001. **24**(1): p. 33-7.

88. Flanigan, R.C., et al., *Accuracy of digital rectal examination and transrectal ultrasonography in localizing prostate cancer.* J Urol, 1994. **152**(5 Pt 1): p. 1506-9.

89. Djavan, B. and M. Margreiter, *Biopsy standards for detection of prostate cancer.* World Journal of Urology, 2007. **25**(1): p. 11-17.

90. Bjurlin, M.A., et al., *Optimization of initial prostate biopsy in clinical practice: sampling, labeling and specimen processing.* J Urol, 2013. **189**(6): p. 2039-46.

91. Eskicorapci, S.Y. and L. Tuncay, *Re: Diagnostic value of systematic biopsy methods in the investigation of prostate cancer: a systematic review. K. Eichler, S. Hempel, J. Wilby, L. Myers, L. M. Bachmann and J. Kleijnen, J Urol, 175: 1605-1612, 2006.* J Urol, 2006. **176**(6 Pt 1): p. 2745; author reply 2745-6.

92. Fütterer, J.J., et al., *High-risk prostate cancer: value of multi-modality 3T MRI-guided biopsies after previous negative biopsies.* Abdominal Radiology, 2012. **37**(5): p. 892-896.

93. Cam, K., et al., *Accuracy of transrectal ultrasound guided prostate biopsy: histopathological correlation to matched prostatectomy specimens.* Int J Urol, 2002. **9**(5): p. 257-60.

94. Washington, S.L., et al., *Transrectal ultrasonography-guided biopsy does not reliably identify dominant cancer location in men with low-risk prostate cancer.* BJU Int, 2012. **110**(1): p. 50-5.

95. Panebianco, V., et al., *Conventional imaging and multiparametric magnetic resonance (MRI, MRS, DWI, MRP) in the diagnosis of prostate cancer.* Q J Nucl Med Mol Imaging, 2012. **56**(4): p. 331-42.

96. Rosi, G., et al., *Role of multiparametric MRI in the diagnosis of prostate cancer: update.* Urologia, 2016. **83**(2): p. 61-67.

97. Boesen, L., *Multiparametric MRI in detection and staging of prostate cancer.* Dan Med J, 2017. **64**(2).

98. Futterer, J.J., et al., *Prostate cancer: local staging at 3-T endorectal MR imaging--early experience.* Radiology, 2006. **238**(1): p. 184-91.

99. Beyersdorff, D., et al., *MRI of prostate cancer at 1.5 and 3.0 T: comparison of image quality in tumor detection and staging.* AJR Am J Roentgenol, 2005. **185**(5): p. 1214-20.

100. Bittencourt, L.K., et al., *Multiparametric magnetic resonance imaging of the prostate: current concepts.* Radiol Bras, 2014. **47**(5): p. 292-300.

101. Sankineni, S., M. Osman, and P.L. Choyke, *Functional MRI in prostate cancer detection.* Biomed Res Int, 2014. **2014**: p. 590638.

102. Yoo, S., J.K. Kim, and I.G. Jeong, *Multiparametric magnetic resonance imaging for prostate cancer: A review and update for urologists.* Korean Journal of Urology, 2015. **56**(7): p. 487-497.

103. Vargas, H.A., et al., *Normal Central Zone of the Prostate and Central Zone Involvement by Prostate Cancer: Clinical and MR Imaging Implications.* Radiology, 2012. **262**(3): p. 894-902.

104. Akin, O., et al., *Transition zone prostate cancers: features, detection, localization, and staging at endorectal MR imaging.* Radiology, 2006. **239**(3): p. 784-92.

105. Rosenkrantz, A.B. and S.S. Taneja, *Radiologist, be aware: ten pitfalls that confound the interpretation of multiparametric prostate MRI.* AJR Am J Roentgenol, 2014. **202**(1): p. 109-20.

106. De Visschere, P.J., et al., *Multiparametric magnetic resonance imaging characteristics of normal, benign and malignant conditions in the prostate.* Eur Radiol, 2017. **27**(5): p. 2095-2109.

107. Gupta, R.T., et al., *Multiparametric prostate MRI: focus on T2-weighted imaging and role in staging of prostate cancer.* Abdom Radiol (NY), 2016. **41**(5): p. 831-43.

108. Sala, E., et al., *Endorectal MR imaging in the evaluation of seminal vesicle invasion: Diagnostic accuracy and multivariate feature analysis.* Radiology, 2006. **238**(3): p. 929-937.

109. Ren, J., et al., *Seminal vesicle invasion in prostate cancer: prediction with combined T2-weighted and diffusion-weighted MR imaging.* Eur Radiol, 2009. **19**(10): p. 2481-6.

110. Baliyan, V., et al., *Diffusion weighted imaging: Technique and applications.* World J Radiol, 2016. **8**(9): p. 785-798.

111. Ueno, Y., et al., *Computed diffusion-weighted imaging using 3-T magnetic resonance imaging for prostate cancer diagnosis.* European Radiology, 2013. **23**(12): p. 3509-3516.

112. Provenzale, J.M., et al., *Use of MR exponential diffusion-weighted images to eradicate T2 "shine-through" effect.* AJR Am J Roentgenol, 1999. **172**(2): p. 537-9.

113. Vargas, H.A., et al., *Diffusion-weighted endorectal MR imaging at 3 T for prostate cancer: tumor detection and assessment of aggressiveness.* Radiology, 2011. **259**(3): p. 775-84.

114. Nicholson, B., G. Schaefer, and D. Theodorescu, *Angiogenesis in prostate cancer: biology and therapeutic opportunities.* Cancer Metastasis Rev, 2001. **20**(3-4): p. 297-319.

115. Thompson, J., et al., *The role of magnetic resonance imaging in the diagnosis and management of prostate cancer.* BJU Int, 2013. **112 Suppl 2**: p. 6-20.

116. Turkbey, B., B. Turkbey, and P.L. Choyke, *Multiparametric MRI and prostate cancer diagnosis and risk stratification.* Current opinion in urology, 2012. **22**(4): p. 310-315.

117. Verma, S., et al., *Overview of dynamic contrast-enhanced MRI in prostate cancer diagnosis and management.* AJR Am J Roentgenol, 2012. **198**(6): p. 1277-88.

118. Isebaert, S., et al., *Evaluation of semi-quantitative dynamic contrast-enhanced MRI parameters for prostate cancer in correlation to whole-mount histopathology.* Eur J Radiol, 2012. **81**(3): p. e217-22.

119. Hansford, B.G., et al., *Dynamic Contrast-enhanced MR Imaging Curve-type Analysis: Is It Helpful in the Differentiation of Prostate Cancer from Healthy Peripheral Zone?* Radiology, 2015. **275**(2): p. 448-457.

120. Cuenod, C.A. and D. Balvay, *Perfusion and vascular permeability: basic concepts and measurement in DCE-CT and DCE-MRI.* Diagn Interv Imaging, 2013. **94**(12): p. 1187-204.

121. Pinto, P.A., et al., *Magnetic resonance imaging/ultrasound fusion guided prostate biopsy improves cancer detection following transrectal ultrasound biopsy and correlates with multiparametric magnetic resonance imaging.* J Urol, 2011. **186**(4): p. 1281-5.

122. Westphalen, A.C. and A.B. Rosenkrantz, *Prostate imaging reporting and data system (PI-RADS): reflections on early experience with a standardized interpretation scheme for multiparametric prostate MRI.* AJR Am J Roentgenol, 2014. **202**(1): p. 121-3.

123. Clements, R., et al., *ESUR prostate MR guidelines 2012.* European Radiology, 2012. **22**(4): p. 746-757.

124. Rothke, M., et al., *[PI-RADS classification: structured reporting for MRI of the prostate]*. Rofo, 2013. **185**(3): p. 253-61.

125. Roethke, M.C., et al., *Evaluation of the ESUR PI-RADS scoring system for multiparametric MRI of the prostate with targeted MR/TRUS fusion-guided biopsy at 3.0 Tesla.* European Radiology, 2014. **24**(2): p. 344-352.

126. Junker, D., et al., *Evaluation of the PI-RADS scoring system for mpMRI of the prostate: a whole-mount step-section analysis.* World Journal of Urology, 2015. **33**(7): p. 1023-1030.

127. Roethke, M.C., et al., *Evaluation of the ESUR PI-RADS scoring system for multiparametric MRI of the prostate with targeted MR/TRUS fusion-guided biopsy at 3.0 Tesla.* European Radiology, 2014. **24**(2): p. 344-352.

128. Dickinson, L., et al., *Magnetic resonance imaging for the detection, localisation, and characterisation of prostate cancer: recommendations from a European consensus meeting.* Eur Urol, 2011. **59**(4): p. 477-94.

129. Ward, A.D., et al., *Prostate: Registration of digital histopathologic images to in vivo MR images acquired by using endorectal receive coil.* Radiology, 2012. **263**(3): p. 856-864.

130. Ward, A.D., et al., *Prostate: registration of digital histopathologic images to in vivo MR images acquired by using endorectal receive coil.* Radiology, 2012. **263**(3): p. 856-64.

131. Ward, A.D., et al., *Registration of In Vivo Prostate Magnetic Resonance Images to Digital Histopathology Images*, in *Prostate Cancer Imaging. Computer-Aided Diagnosis, Prognosis, and Intervention: International Workshop, Held in Conjunction with MICCAI 2010, Beijing,China, September 24, 2010. Proceedings*, A. Madabhushi, et al., Editors. 2010, Springer Berlin Heidelberg: Berlin, Heidelberg. p. 66-76.

132. Gibson, E., et al., *Registration of prostate histology images to ex vivo MR images via strand-shaped fiducials.* Journal of Magnetic Resonance Imaging, 2012. **36**(6): p. 1402-1412.

133. Gibson, E., et al., *3D prostate histology image reconstruction: Quantifying the impact of tissue deformation and histology section location.* Journal of Pathology Informatics, 2013. **4**(1): p. 31-31.

134. Gibson, E., et al., *Toward prostate cancer contouring guidelines on MRI: dominant lesion gross and clinical target volume coverage via accurate histology fusion.* International Journal of Radiation OncologyBiologyPhysics, 2016.

135. Villers, A. and A. Ouzzane, *Multimodality MRI-Guided Targeting*, in *Imaging and Focal Therapy of Early Prostate Cancer*, J.T. Polascik, Editor. 2013, Humana Press: Totowa, NJ. p. 133-140.

136. Moore, C.M., et al., *Image-Guided Prostate Biopsy Using Magnetic Resonance Imaging–Derived Targets: A Systematic Review.* European Urology, 2013. **63**(1): p. 125-140.

137. Wolters, T., et al., *A critical analysis of the tumor volume threshold for clinically insignificant prostate cancer using a data set of a randomized screening trial.* J Urol, 2011. **185**(1): p. 121-5.

138. Weinreb, J.C., et al., *PI-RADS Prostate Imaging – Reporting and Data System: 2015, Version 2.* European Urology, 2016. **69**(1): p. 16-40.

139. Polanec, S., et al., *Head-to-head comparison of PI-RADS v2 and PI-RADS v1*. European Journal of Radiology, 2016. **85**(6): p. 1125-1131.

Curriculum Vitae

Mena Gaed

EDUCATION

2012-2018 **Master of Science,** Pathology M.Sc.
University of Western, London, Ontario

2006 **Bachelor of Medicine and Bachelor of Surgery MB. BCH**
Cairo University, Cairo, Egypt

POST-GRADUATE QUALIFICATIONS

2013 National Assessment Collaboration (NAC) Objective Structured Clinical Examination
2011 Ultra Sound Operator
2011 MRI Operator
2010 Centre for the Evaluation of Health Professional Educated Abroad CEHPEA
2009 Medical Council of Canada Qualifying Exam One MCCQ1
2008 Medical Council of Canada Evaluation Exam MCCEE

RELEVANT WORK EXPERIENCE

2010-P **Pathologist Research Assistant**
London Health Science Centre/ Robarts Research Institute

2015-P **Ontario Telemedicine Network (OTN)**
Physician Assistant

2005-2016 **Central Mall Drug Mart**
Pharmacy Office Manager

OBSERVERSHIP

2014 Summer **London Health Science Centre**
Anatomical Pathology Observer-ship

2013-2014 **Windsor River Walk-In Clinic**
Family Medicine Observer-ship

2005-2006 **Central Mall Medical Centre**
Family Medicine Observer-ship

PUBLICATIONS

JOURNALS

1. E. Gibson, **M. Gaed**, T. Hrinivich, J.A. Gómez, M. Moussa, C. Romagnoli, J. Mandel, M. Bastian-Jordan, D.W. Cool S. Ghoul, S.E. Pautler, J.L. Chin, C. Crukley, G. S. Bauman, A. Fenster, A.D. Ward. Multiparametric MR imaging of prostate cancer foci: assessing the detectability and localizability of Gleason 7 peripheral zone cancers based on image contrasts. Medical Imaging 2014: Digital Pathology, SPIE 9041. [DOI: 10.1117/12.2043324]

2. M. Salarian, E. Gibson, M. Shahedi, **M. Gaed,** J.A. Gómez, M. Moussa, C. Romagnoli, D.W. Cool, M. Bastian-Jordan, J.L. Chin, S.E. Pautler, G. S. Bauman. Accuracy and variability of tumour burden measurement on multi-parametric MRI. Medical Imaging 2014: Digital Pathology, SPIE 9041. [DOI: 10.1117/12.2043716]

3. E. Gibson, C. Crukley, **M**. **Gaed,** J.A. Gómez, M. Moussa, J.L. Chin, G.S. Bauman, A. Fenster, A.D. Ward. Registration of prostate histology images to ex vivo MR images via strand-shape fiducials. Journal of Magazine of Reasoning Imaging, 2012. [DOI: 10.1002/jmri.23767]

4. E. Gibson, **M. Gaed**, J. A. Gómez, M. Moussa, S. Pautler, J. L. Chin, C. Crukley, G. S. Bauman, A. Fenster, A. D. Ward. 3D prostate histology image reconstruction: quantifying the impact of tissue deformation and histology section location. Journal of Pathology Informatics, 2013.

5. E. Gibson, **M. Gaed**, J. A. Gómez, M. Moussa, C. Romagnoli, S. Pautler, J. L. Chin, C. Crukley, G. S. Bauman, A. Fenster, A. D. Ward. 3D prostate histology reconstruction: an evaluation of image-based and fiducial-based algorithms. Medical Physics, 40(9), 093501, 2013. [10.1118/1.4816946]

6. F. Imani, P. Abolmaesumi, E. Gibson, A. Khojaste**, M. Gaed**, M. Moussa, J. A. Gómez, C. Romagnoli, D. R. Siemens, M. Leviridge, S. Chang, Fenster, A. D. Ward, P. Mousavi. Ultrasound-based characterization of prostate

cancer: an in vivo clinical feasibility study. In Medical Image Computing and Computer-Assisted Intervention. 2013;16(Pt2):279-86

7. L. Gorelick, O. Veskler, **M. Gaed,** J.A. Gómez, M. Moussa, G.S. Bauman, A. Fenster, A.D. Ward. Prostate Histopathology: Learning Tissue Component Histograms for Cancer Detection and Classification. Transactions on Medical Imaging, May 2013

BOOK CHAPTERS

1. Gibson, C. Crukley, **M. Gaed**, J. A. Gómez-Lemus, M. Moussa, C. Romagnoli, S. Pautler, J. Chin, G. Bauman, A. Fenster, A. D. Ward. 3D registration of whole-mount prostate histology images to ex vivo magnetic resonance images using strand-shaped fiducials. In Abdomen and Thoracic Imaging: An Engineering & Clinical Perspective, A. S. El-Baz, L. Saba, J. Suri.

ORAL PRESENTATIONS

1. **M. Gaed.** MRI Signaling to Non-Cancerous Abnormalities That Could Mimic Cancer in Prostate. Journal Club Oral Presentations, Department of Pathology, The University of Western Ontario; London, Canada, April 01, 2014.

2. **M. Gaed**. Prostate Cancer Subtype & Grade In Correlation With MRI. Journal Club Oral Presentations, Department of Pathology, The University of Western Ontario; London, Canada, April 09, 2013.

3. E.Gibson, I. Rachinsky, **M. Gaed**, C. Romagnoli, T. Lee, C. Crukley, J.A. Gómez-Lemus, M. Moussa, J.L. Chin, G. Bauman, A. Fenster, A.D. Ward. Ontario's first F fluorocholine prostate PET images: histology and multi-parametric MRI correlation. Robarts Research Institute, Department of Medical Imaging, The University of Western Ontario; Lawson Health Research Institute; Department of Medical Biophysics, Department of

Pathology, Department of Urology, Department of Oncology, The University of Western Ontario; Baines Imaging Research Laboratories, London Health Sciences Centre, London, Canada, April 2012.

4. E. Gibson, C. Crukley, **M. Gaed**, J. A. Gómez-Lemus, M. Moussa, J. L.Chin, G. Bauman, A. Fenster, A. D. Ward. Validation of direct registration of whole-mount prostate digital histopathology to ex vivo MR images, Medical Image Computing and Computer-Assisted Intervention (MICCAI) Prostate Cancer Imaging Workshop, Toronto, Canada, *September 2011*. (Oral presentation by E. Gibson and J. L. Chin)

CONFERENCE MANUSCRIPTS

1. E. Gibson, C. Crukley, **M. Gaed**, J. A. Gómez-Lemus, M. Moussa, J. L. Chin, G. Bauman, A. Fenster, A. D. Ward. Validation of direct registration of whole-mount prostate digital histopathology to ex vivo MR images, Medical Image Computing and Computer-Assisted Intervention (MICCAI) Prostate Cancer Imaging Workshop, Prostate cancer imaging: image analysis and image-guided interventions, Lecture Notes in Computer Science, 6963(2011) pp 134-145, *2011*.
2. E. Gibson, C. Crukley, V. Karnik, **M. Gaed**, J. A. Gómez-Lemus, M.Moussa, J. L. Chin, G. Bauman, A. Fenster, A. D. Ward. Co-registration framework for histology-registration-based validation of fused multimodality prostate cancer imaging, IEEE International conference on Intelligent Computation and Bio-Medical Instrumentation, Wuhan, China, *December 2011*.

PEER-REVIEWED CONFERENCE PROCEEDINGS

1. E. Gibson, **M. Gaed**, J. A. Gómez-Lemus, M. Moussa, C. Romagnoli, J. L. Chin, C. Crukley, G. S. Bauman, A. Fenster, A. D. Ward. 3D prostate histology reconstruction: an evaluation of image-based and fiducial-based algorithms. In *SPIE Medical Imaging: Digital Pathology*, 8676, pp. 86760A,

Orlando, USA, Mar. 2013. (podium presentation by E. Gibson) [10.1117/12.2006897].

2. E. Gibson, **M. Gaed**, T. Hrinivich, J. A. Gómez, M. Moussa, C. Romagnoli, J. Mandel, M. Bastian-Jordan, D. Cool, S. Ghoul, S. Pautler, J. L. Chin, C. Crukley, G. S. Bauman, A. Fenster, A. D. Ward. Multiparametric MR imaging of prostate cancer foci: assessing the detectability and localizability of Gleason 7 peripheral zone cancers based on image contrasts. In *SPIE Medical Imaging*, San Diego, USA, Feb. 2014.

3. M. Salarian, E. Gibson, M. Shahedi, **M. Gaed**, J. A. Gómez, M. Moussa, C. Romagnoli, D. W. Cool, M. Bastian-Jordan, J. L. Chin, S. Pautler, G. S. Bauman, A. D. Ward. Accuracy and variability of tumour burden measurement on multi-parametric MRI. In *SPIE Medical Imaging*, San Diego, USA, Feb. 2014. (podium presentation by M. Salarian)

4. M. Salarian, M. Shahedi, E. Gibson, **M. Gaed**, J. A. Gómez-Lemus, M. Moussa, G. S. Bauman, A. D. Ward. Toward quantitative digital histopathology for prostate cancer: comparison of inter-slide interpolation methods for tumour measurement. In *SPIE Medical Imaging: Digital Pathology*, 8676, pp. 86760F, Orlando, USA, Mar. 2013. (podium presentation by M. Salarian) [10.1117/12.2007103]

5. T. Hrinivich, E. Gibson, **M. Gaed**, J. A. Gómez, M. Moussa, C. McKenzie, G. Bauman, A. D. Ward, A. Fenster, E. Wong. A dimensionless dynamic contrast enhanced MRI parameter for intra-prostatic tumour target volume delineation: initial comparison with histology. In SPIE Medical Imaging, San Diego, USA, Feb. 2014.

PEER-REVIEWED CONFERENCE ABSTRACTS

1. E. Gibson, M. Gaed, J. A. Gómez, M. Moussa, C. Romagnoli, J. Mandel, M. Bastian-Jordan, S. Ghoul, D. Cool, S. Pautler, J. L. Chin, C. Crukley, G. S. Bauman, A. Fenster, A. D. Ward. Toward contouring guidelines for

prostate cancer focal therapy planning on MRI: characterisation of tumour boundary contrast via accurate pathology fusion. Ann. Meeting Radiological Society of North America, Chicago, USA, Dec. 2013. (podium presentation by E. Gibson)

2. E. Gibson, **M. Gaed**, J. A. Gómez, M. Moussa, C. Romagnoli, J. Mandel, M. Bastian-Jordan, S. Ghoul, D. Cool, S. Pautler, J. L. Chin, C. Crukley, G. S. Bauman, A. Fenster, A. D. Ward. Toward contouring guidelines for prostate cancer focal therapy planning on MRI: characterisation of tumour boundary contrast via accurate pathology fusion. Australian-Canadian Prostate Cancer Research Alliance Symposium, Port Douglas, Australia, Aug. 2013. (Prostate Cancer Canada travel award; one of seven posters selected for podium presentation)

3. G. Bauman, J. Mandel, C. Romagnoli, I. Rachinsky, A. D. Ward, E. Gibson, **M. Gaed**, M. Moussa, J. Gómez-Lemus, J. Chin, S. Pautler, J. Butler, E. Wong, T.-Y. Lee. 18-fluorocholine imaging of localized prostate cancer: first experience with hybrid PET/MRI. Ann. Meeting Canadian Organization of Medical Physicists-Canadian Association of Radiation Oncology, Montreal, Canada, Sep. 2013.

4. M. Salarian, M. Shahedi, E. Gibson, **M. Gaed**, J. A. Gómez, M. Moussa, D. W. Cool, C. Romagnoli, G. S. Bauman, A. D. Ward. Imaging validation and quantitative pathology in prostate cancer: shape interpolation methods for tumour measurement. Ann. Meeting Canadian Organization of Medical Physicists-Canadian Association of Radiation Oncology, Montreal, Canada, Sep. 2013. (podium presentation by M. Salarian)

LOCAL/PROVINCIAL/NATIONAL CONFERENCE ABSTRACTS

1. E. Gibson, **M. Gaed**, J. A. Gómez, M. Moussa, C. Romagnoli, J. Mandel, M. Bastian-Jordan, S. Ghoul, D. Cool, S. Pautler, J. L. Chin, C. Crukley, G. S. Bauman, A. Fenster, A. D. Ward. Toward contouring guidelines for prostate cancer focal therapy planning on MRI: characterisation of tumour

boundary contrast via accurate pathology fusion. Canadian Cancer Research Conference, Toronto, Canada, Nov. 2013.

2. E. Gibson, **M. Gaed**, J. A. Gómez, M. Moussa, C. Romagnoli, J. Mandel, M. Bastian-Jordan, S. Ghoul, D. Cool, S. Pautler, J. L. Chin, C. Crukley, G. S. Bauman, A. Fenster, A. D. Ward. Toward contouring guidelines for prostate cancer focal therapy planning on MRI: characterisation of tumour boundary contrast via accurate pathology fusion. Oncology Research and Education Day, London, Canada, Jun. 2013.

3. E. Gibson, **M. Gaed,** J. A. Gómez, M. Moussa, C. Romagnoli, J. Mandel, M. Bastian-Jordan, S. Ghoul, D. Cool, S. Pautler, J. L. Chin, C. Crukley, G. S. Bauman, A. Fenster, A. D. Ward. Toward contouring guidelines for prostate cancer focal therapy planning on MRI: characterisation of tumour boundary contrast via accurate pathology fusion. London Imaging Discovery, London, Canada, Jun. 2013. (podium presentation by E. Gibson; honourable mention)

4. M. Salarian, M. Shahedi, E. Gibson, **M. Gaed**, J. A. Gómez, M. Moussa, D. W. Cool, C. Romagnoli, G. S. Bauman, A. D. Ward. Imaging validation and quantitative pathology in prostate cancer: shape interpolation methods for tumour measurement. Canadian Cancer Research Conference, Toronto, Canada, Nov. 2013.

POSTER PRESENTATIONS

1. E. Gibson, C. Crukley, V. Karnik, **M. Gaed**, J. A. Gómez-Lemus, M. Moussa, J. L. Chin, G. Bauman, A. Fenster, A. D. Ward. Co-registration framework for histology-registration-based validation of fused multimodality prostate cancer imaging, IEEE International conference on Intelligent Computation and Bio-Medical Instrumentation, presented at Wuhan, China, December 2011.

2. E. Gibson, C. Crukley, V. Karnik, **M. Gaed**, J. A. Gómez, M. Moussa, J. L. Chin, G. Bauman, A. Fenster, A. D. Ward, From digital histopathology to in

vivo imaging: 3D reconstruction, registration and validation. To be presented at Canadian Cancer Research Conference, Toronto, Canada, November 2011.

3. E. Gibson, C. Crukley, V. Karnik, **M. Gaed**, J. A. Gómez, M. Moussa, J. L. Chin, G. Bauman, A. Fenster, A. D. Ward. 3D reconstruction of prostate histopathology for co-registration with in vivo imaging. Presented at Pathology Visions, San Diego, USA, October 2011.